

Investigation on Stress Increase of Sand inside Immersed Tunnel Joint Gap

R. Rahadian | 4519000 | October 2017



Gemeente Rotterdam



Van Hattum en Blankevoort

Investigation on Stress Increase of Sand inside Immersed Tunnel Joint Gap

by

Rheza Rahadian

4519000

in partial fulfilment of the requirements for the degree of

Master of Science

in Geo Engineering

at Technische Universiteit Delft

to be defended publicly on Friday October 13, 2017 at 09.30 AM.

October 2, 2017

Supervisor:	Dr. Ir. W. Broere	TU Delft
Thesis committee:	Ir. D. Wilschut	Gemeentewerken Rotterdam
	Ir. S. van der Woude	Van Hattum en Blankevoort
	Dr. Ir. C.B.M. Blom	TU Delft
	Prof. Dr. M.A. Hicks	TU Delft



[This page is intentionally left blank]

Preface

This document serves as a partial fulfillment for the degree of Master of Science in Geo-Engineering at Delft University of Technology. This report concludes the master's program with a 10-month long thesis research project under the supervision and guidance of a graduation committee consisting of experts in the related field.

The underground space field of study, specifically tunnel design, and construction, had always been an intriguing subject for me to learn. The abundance of tunneling experts in The Netherlands prompted me to seek a final project related to this topic. On top of that, a research centered on laboratory experiment and testing, as well as the skill to design and construct a custom test device is a valuable experience to have. Therefore when this project (physical modeling of an immersed tunnel joint gap) was offered to me, I regarded it as a great opportunity to further my knowledge in the subject.

The journey to complete this project was long and bumpy at times. None of it would have been finished without the support, guidance, and blessing of many. I would like to take this opportunity to thank the people involved throughout the completion of this project.

The construction of the laboratory test device and all the instruments involved would not be made possible without the financial support from Rotterdam Elektrische Tram. I would also like to thank Ir. D. Wilschut and the Municipality of Rotterdam for their assistance and financial support.

I would like to express my deepest gratitude to Dr. Ir. W. Broere for his extended supervision, advice, and guidance for the entire duration of the project. The finalization of the thesis project along with this report would not be possible without the continued assistance and feedback from the graduation committee: the technical expertise and invaluable advice of Ir. D. Wilschut, the critical observations, and comments of Dr. Ir. C.B.M. Blom, the unwavering enthusiasm of Ir. S. van der Woude, and the academic guidance of Prof. Dr. M.A. Hicks.

I would like to thank S. van Herk, and T. Philips of DEMO, as well as C. van Beek and R. van Leeuwen, whose direct involvements in the device design, construction, and set up, was crucial to the finalization of the physical model. Special thanks to J. van Stee and Trelleborg Ridderkerk B.V. for providing a custom model Gina seal and a general insight on rubber gaskets. Thank you to J.J. de Visser for his assistance and supervision during experiments. Photos of the device included in this report are courtesy of C. Kevinly.

Thank you to the Republic of Indonesia, and the Indonesian Endowment Fund for Education (LPDP) for supporting me financially for the majority of my stay in Delft through a full scholarship.

Finally, I would like to thank the people closest to my heart. Thank you to my beloved parents, Bambang Priambodho and Yuyu Yuliasih for constantly supporting me with their love and prayers every day of my life. Thank you to my dear siblings and their families; Rizki & Dindy Pratama, and Karina & Marco Zedda, who always provided me with love and comfort whenever I visit them, even in the midst of their busy lives. And lastly for all my friends, here in Delft, back home in Indonesia, and all around the world, thank you for always being present for me. You made these 2 years at TU Delft a fun, enjoyable and unforgettable experience.

R. Rahadian

Delft, 28 September 2017

[This page is intentionally left blank]

Abstract

Watertightness and leakage prevention is crucial in every tunnel joint design. Immersed tunnels have been utilizing the Gina-Omega gasket solution since the 1960s to prevent leakage from occurring. The Rotterdam Metrotunnel was completed in 1968 and is the first tunnel in The Netherlands to implement the Gina-Omega gasket solution in its immersion joints. However, after almost 50 years of service life, leakages were detected in the immersion joints, which leads to an investigation into the source of the problem. It was uncovered that the bolts of the Gina gaskets had failed due to the immense load exerted by the sand above them.

It was apparent that the load on the gaskets builds up due to an increase in soil stresses. A hypothesis was formed regarding this phenomenon; the sand inside the joint gap was exposed to almost 50 years of loading and unloading cycles from the expansion and contraction of the tunnel elements due to seasonal changes in temperature. This, in turn, densifies the sand inside the joint gap, which results in rising soil stresses.

A 1:3 scaled physical model of the joint gap was designed and constructed to test the validity of this hypothesis. The model joint gap is equipped with a static lining on one end and an actuated lining on the other, hence the device is able to imitate the annual joint contraction and expansion cycle. A barrel containing sand is fixed onto the top of the model joint gap and acts as a reservoir of sand, allowing for more sand to enter the joint gap. The device is also equipped with 2 load cells and an LVDT, which allows for the measurement of horizontal soil stresses and vertical gasket displacement respectively. Two holes, with a flap covering each of them, are installed on the side of the model joint gap, which allows for a penetrometer test to be conducted on the joint gap sand.

Multiple experiments with varying configurations and test conditions were performed. The results show that although the multiple loading and unloading cycles apply the same displacement for every cycle, the soil stresses increase with time. The Gina gasket show an apparent “walking effect,” where the gasket moves continually inwards. While a similar test conducted without the presence of sand fails to produce any “walking effect.” Penetrometer measurements show that the soil increases in density over time.

The investigation is continued further with finite element analysis using the geotechnical modeling software PLAXIS. The joint gap part of the device is modeled in the program and is subjected to loading conditions and configuration similar to the physical model. Results of the simulation show indications of gasket “walking effect,” as well as stress-strain behavior similar to the experiment results. A comparison analysis between the results of the physical and finite element model is subsequently conducted. The finite element analysis allows for the calculation of the sand vertical stresses, which is previously unable to be measured during the experiment. It is observed that the vertical stresses rapidly escalates due to the high friction between the sand and the lining wall.

A further analysis is conducted to estimate the force required to push back the displaced Gina gasket. Due to the good agreement between the results of the physical and finite element models, a modified version of the finite element model is used to predict the resulting pushing-back forces.

Finally, the research is concluded with the validity of the previous-mentioned hypothesis. It was also confirmed that the soil undergoes densification, proven by the penetrometer readings as well as further validated by the stress-strain behavior of the sand. It is also proven that at higher horizontal strain, the increase in density, stresses, and the “waking effect” is more pronounced.

The force analysis produces values of force needed to push back the Gina gasket. It was concluded that pushing back the entire Gina gasket upwards would require a high amount of force. However, affecting only 1/3 of the gasket bottom area would result in the gasket merely being pushed aside while failing to push the soil upwards.

[This page is intentionally left blank]

Contents

Preface	i
Abstract.....	iii
Nomenclature	viii
Chapter 1 Introduction.....	1
1.1. Project Summary	1
1.2. Topic Description.....	1
1.3. Research Questions	2
1.4. Methodology.....	2
1.5. Report Outline	3
Chapter 2 Literature Study	4
2.1. Immersed Tunnel.....	4
2.1.1. Joints in an Immersed Tunnel	4
2.1.2. Soil inside Joint Gap	5
2.2. Soil Behavior	5
2.2.1. Cyclic Loading of Soil	5
2.2.2. Densification of Soil.....	6
2.2.3. Discussion on Cyclic Loading vs. Static Compaction.....	13
2.2.4. Soil Arching.....	13
2.2.5. Ground Arch/Dome Effect	14
2.2.6. Discussions on Soil Arching and Ground Arch/Dome Effect.....	15
2.3. Measurement Instruments	15
2.3.1. Cone Penetrometer Test	16
2.3.2. Measurement of Soil Stresses using Load Cells.....	18
2.4. Metro Tunnel	22
2.4.1. History.....	22
2.4.2. Technical Specifications.....	23
2.4.3. Gina Profile	24
2.4.4. Soil Type	25
Chapter 3 Test Equipment and Setup	26
3.1. Test Equipment	26
3.1.1. Overview	26
3.1.2. Soil Type	27
3.1.3. Section (a) Soil Drum	28
3.1.4. Section (b) Immersion Joint Gap	29
3.1.5. Model Gina Gasket	30
3.1.6. Actuator Force	31

3.1.7. Instrumentation	31
3.2. General Experiment Procedure	34
3.2.1. Setup Procedure	34
3.2.2. Experiment Procedure.....	35
3.2.3. Control Tests.....	35
3.3. Test Configurations	36
3.3.1. Reference Configuration	36
3.3.2. Variations in the Configuration	37
3.3.3. Summary of Configurations & Test Conditions	37
3.3.4. Extra Configurations.....	38
3.4. Experiment Timeline	38
Chapter 4 Laboratory Test Result Analysis	40
4.1. Test Results	40
4.1.1. Overview	40
4.1.2. Stresses	40
4.1.3. Gasket Bottom Side Deflections.....	41
4.1.4. Penetrometer Test	42
4.2. Analysis	43
4.2.1. Gina Gasket Deflection Analysis	43
4.2.2. Soil Stress Analysis.....	46
4.2.3. Stress Path Analysis	47
4.2.4. Evolution of Soil Density.....	48
Chapter 5 Finite Element Analysis	51
5.1. Overview	51
5.2. Parameters.....	51
5.2.1. Model Sand.....	51
5.2.2. Gina Gasket.....	51
5.2.3. Interface.....	52
5.3. Model Structure	52
5.4. Calculation Steps.....	53
5.5. Model Results.....	54
5.5.1. Soil Stresses	54
5.5.2. Plastic Points	56
5.5.3. Deformations.....	56
5.6. Effects of Changing Soil Density.....	57
5.6.1. Horizontal Stresses	57
5.6.2. Soil Deformations.....	58
5.6.3. Gina Gasket Deformations	60
Chapter 6 Discussions	61
6.1. Laboratory Experiment Results versus Finite Element Analysis Results	61

6.1.1. Evolution of Soil Stresses in a Cycle	61
6.1.2. Soil Stresses vs. Gasket Displacement	62
6.2. Sand Effective Vertical Stress.....	64
6.2.1. Role of Interface Friction	65
6.2.2. Stress Path Analysis with Adjusted Parameters and Assumptions	65
6.3. Force Analysis	66
6.3.1. Model Structure and Calculation Conditions.....	66
6.3.2. Results and Analysis.....	67
Chapter 7 Conclusions and Further Research	70
7.1. Conclusions.....	70
7.2. Limitations and Further Research.....	72
7.2.1. Possible Further Research Topics	72
7.2.2. Solutions	72

Nomenclature

σ	Soil total stress	FoS	Factor of safety
σ'	Soil effective stress	ρ	Mass density
σ_v	Vertical soil stress	γ_d	Dry density
σ_h	Horizontal soil stress	γ_{sat}	Saturated density
τ	Shear stress	c	Cohesion
γ_{xy}	Shear strain	E_{oed}	Oedometer modulus
D_r	Soil relative density	E_{50}	Tangential modulus
D_{r0}	Initial relative density (stress densification)	E_{ur}	Unloading-reloading modulus
e_{max}	Maximum void ratio	ν	Poisson's ratio
e_{min}	Minimum void ratio	G_s	Specific gravity
ϕ	Soil friction angle	q	Overburden load (Terzaghi)
δ	Soil – structure interaction friction angle	G_{soil}	Soil shear modulus
R_f	Friction ratio	G_i	Interface shear modulus
CPT	Cone penetrometer test	R_{inter}	Interface multiplier
f_s	CPT skin friction			
q_c	CPT cone resistance			
Q_{CN}	Adjusted q_c			
Q_c	Compressibility factor (Kulhawy & Mayne)			
OCR	Overconsolidation ratio			
$C_0, C_1,$ C_2	Sand correlation coefficient (Sadrekarimi)			
K_0	Rankine earth pressure coefficient at rest			
q_{cH}	Horizontal q_c (Broere & van Tol)			
q_{cV}	Vertical q_c (Broere & van Tol)			
EPC	Earth pressure cell			
D_{EPC}	EPC sensing diameter			
H	Height			
A	Area			
V	Volume			
W	Weight			
F	Force			

Chapter 1 Introduction

1.1. Project Summary

The thesis research focuses on the project conducted by the partnership of Rotterdam Elektrische Tram, Gemeentewerken Rotterdam, BAM, and van Hattum en Blankevoort for the rehabilitation of the Rotterdam Metro tunnel. The tunnel itself is an immersed tunnel built in 1968 and is the first tunnel to introduce the Gina-Omega gasket solution to watertight design.

It was detected that leakages were occurring across the joints of the immersed tunnel and several inspections were performed in 2015. It was observed that the Gina gaskets punched through the inner side of the tunnel joints and, in some occasions, damaged the Omega gaskets.

It was apparent that the soil on the outer side of the immersion joint gap had exerted pressure onto the Gina Profile. This led to a hypothesis that the soil directly outside of the joint gap had undergone a particular failure mechanism due to the seasonal contraction/expansion of the joint gap, thus densifying joint gap soil and applying pressure. The contraction and expansion of the gap is influenced by the change in temperature along the year.

The design of the Gina gasket configuration also played a role in the incident. The Gina gaskets are placed with a steel strip that contains a support plate in the inner part of the joint, therefore applying a moment force that contributed to the failure of the gasket bolts.

In order to solve the problem, a finite element analysis had been performed using the programs PLAXIS and Abaqus. The analysis came up with forces that were exerted onto the support strip in the roof, walls, and floor of the joints. With the results at hand, the project had included a permanent solution for possible Gina gasket failures in the future. Extra steel supports for the Gina gasket are to be installed in the inner part of the immersion joint to counteract the soil forces.

1.2. Topic Description

The finite element analysis was performed under the hypothesis that the soil underwent densification due to annual cycles of loading and unloading due to the change in temperature. This gives an upper boundary approach in determining the loads on the permanent solution to secure the Gina gasket. However, it has not been confirmed that this phenomenon had occurred over the tunnel lifetime (only labeled plausible by the project team and the involved experts¹).

The research looks into whether or not the densification process is a possibility, as it might pose problems for other immersed tunnels that also implement Gina-Omega solution. The hypothesis states that during colder seasons, the tunnel elements shrink in size (thus expanding the joints), and allowing intrusion of soil in the joint gap. In the warmer seasons, the tunnel expands (thus contracting the joints), consequently densifying the soil in the joint gap while unable to push back the soil outside of the joint gaps.

The original finite element analysis utilized both Abaqus and PLAXIS, as both programs have shortcomings related to this specific analysis: Abaqus is unable to simulate soil behavior correctly, whereas PLAXIS could, but does not provide the deformations and forces in the gasket correctly. Therefore in the analysis, the resulting deformations from the Abaqus model were taken and subsequently applied to the PLAXIS model. The results were then re-applied to Abaqus to obtain the forces exerted onto the Gina gaskets. However, the analysis was unable to simulate the multiple cycles of loading and unloading, as currently there aren't any

¹ Prof. Frits van Tol and Klaas-Jan Bakker

soil models that could model hysteresis due to densification of soil in this particular way. These restrictions and shortcomings led to the inception of this research.

1.3. Research Questions

From the above-mentioned problems, it is interesting to have an understanding of the behavior of soils inside immersion joint gaps. Therefore, as the primary focus of the research, the first research question was asked

- Do the multiple cycles of loading and unloading, due to the annual expansion and contraction of the immersion joint, generate increased stresses in the soil inside the joint?

In the case that the phenomenon occurs, further sub-questions are then asked

- Does the soil experience densification due to the cyclic loading-unloading process?
- To what extent does the mechanics of loading and unloading cycles affect the soil stresses?

1.4. Methodology

The data needed to be able to answer the above-mentioned research questions would involve specific soil behavior inside immersion joint gaps. Therefore it was decided that a physical model would need to be constructed and tested upon. The model would expectedly show soil behavior similar to the soil in the immersion joint gap and observation would then be carried out to determine whether or not soil failure occurs.

As this might be considered an initiatory research for the problem, it is worth noting that the equipment would not be an exact replica of the Metrotunnel joints. One particularly important note is that the experiment will be performed on dry soil. Thus the soil might behave differently compared to the soil in field condition. Details of the equipment are explained in Chapter 3.

The scaled model immersion joint gap would subsequently be analyzed using a finite element program. A finite element model would be made using PLAXIS, similar to the model mentioned in section 1.2, albeit in more detail. Both the finite element model and the following analysis are discussed in Chapter 5.

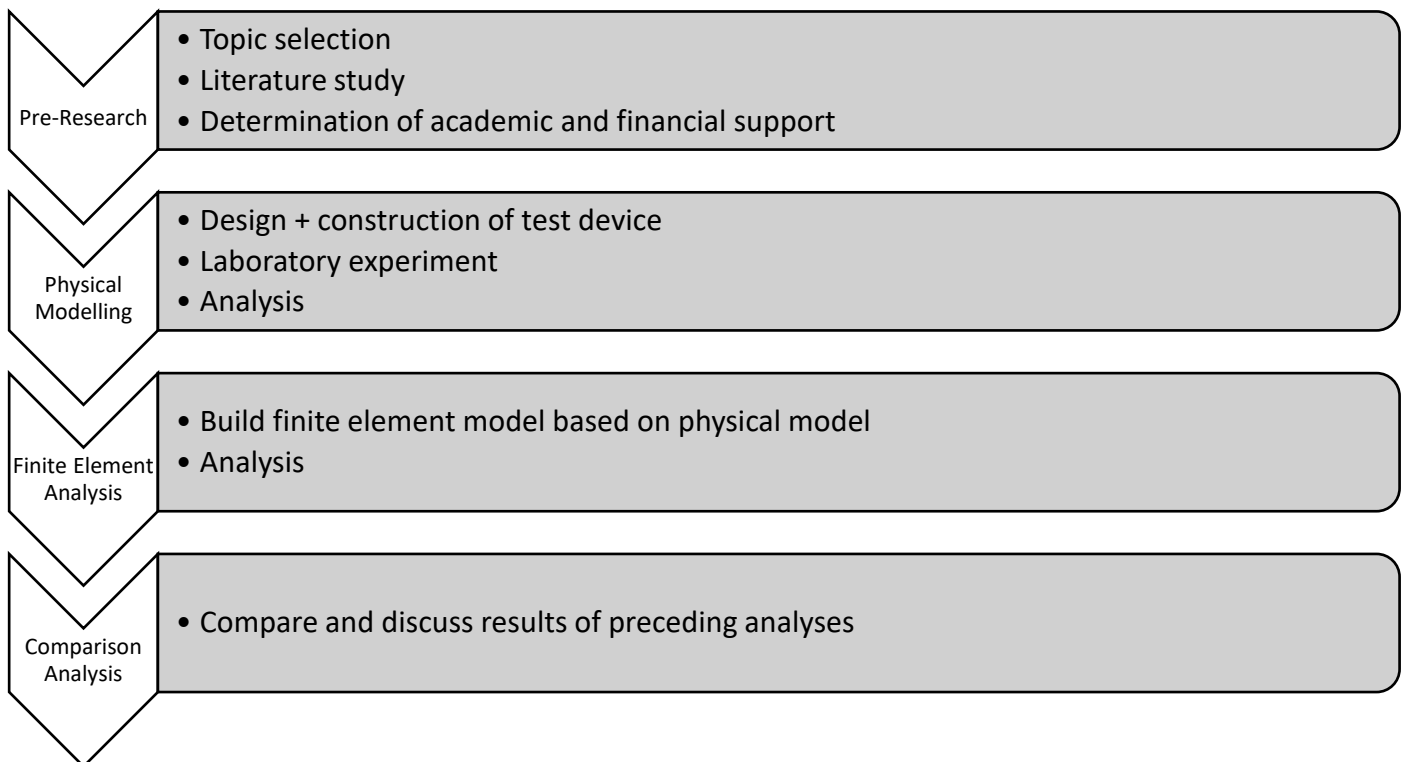


Figure 1-1 Research Methodology Flow Chart

1.5. Report Outline

Chapter 1 provides the general overview of the topic, including a summary of the case study. The research questions are stated along with the research methodology.

Chapter 2 presents various established past studies related to the field of this research. Topics include basic knowledge on immersed tunnel joints, soil behavior on cyclic and static loading, arching and failure mechanism, and a more detailed look at the case study tunnel.

Chapter 3 provides a thorough description of the physical modeling device used in the research. Various test configurations, as well as the detailed procedures, are also stated along with the experiment timeline.

Chapter 4 exhibits the results of the physical model tests, which are mainly the stress, strain, and density measurement readings. It is followed subsequently by an analysis combining the 3 mentioned results.

Chapter 5 describes the finite element model used in this research. The description includes model structure, calculation stages, considerations, and limitations. The outputs of the finite element program are shown, followed by a further analysis on the behavior of the model.

Chapter 6 starts by comparing the results of the 2 previous analyses. It is followed by a further discussion on the soil behavior inside the joint gap considering the results of prior analyses. A further analysis concerning the force required to rehabilitate the existing joint gap is subsequently made.

Chapter 7 concludes the report with statements and findings that answer the overlying research questions. Limitations of this research are acknowledged along with possible further research on this topic.

Chapter 2 Literature Study

2.1. Immersed Tunnel

2.1.1. Joints in an Immersed Tunnel

In principle, there are 2 types of joints in an immersed tunnel, namely the segment joint and the immersion joint. As its name suggests, segment joints are the joints in between the concrete segments of approximately 20-25 meters apart (Lunniss & Baber, 2013). The joint ends are shaped into shear keys to withstand shear forces and to allow a certain degree of movement and bending of the tunnel element. Segment joints usually apply rubber-metal water stops that are grout-injected along the length of the joint, thus preventing leakage.

The second type of joint is the immersion joint, which serves as the connection between tunnel elements. Immersion joints. The elements are lined up end to end and pushed together until the rubber seal along the bulkhead contracts. Water inside the joint gap is subsequently pumped out and the joint compacts further due to the difference in pressure. The formation of immersion joints is shown in Figure 2-1.

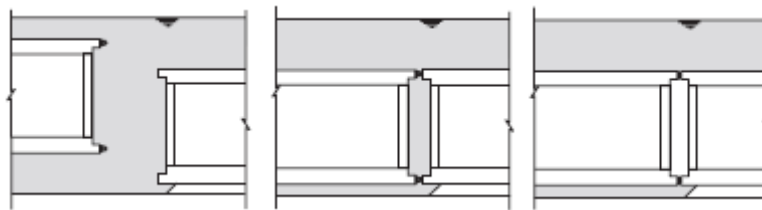


Figure 2-1 Construction of Immersion Joint (Lunniss & Baber, 2013)

The most common solution for immersed tunnel water tightness is the application of Gina-Omega seals along the immersion joints. The Gina is a rubber gasket that is bolted to a frame on the outer edge of the immersion joints, and functions as the primary watertight measure and is usually regarded as temporary construction. The Gina consists of 2 main parts, the stiff base and the soft nose that will compress once the elements are lined up to one another.

The Omega seal is a curved rubber strip placed around the inner side of the immersed joint after the water between the bulkheads have been drained. It functions as the secondary measure against leakage and the permanent solution against leakage. The Omega gasket is held in place with a clamping system as demonstrated in Figure 2-2.

Both the Gina and Omega gaskets are not intended to withstand high loads and pressure. However, as the Gina gasket compresses due to the water pressure, a gap between the end frames forms, as shown in Figure 2-2. The gap allows for water and soil to enter after the soil cover have been backfilled on top of the tunnel.

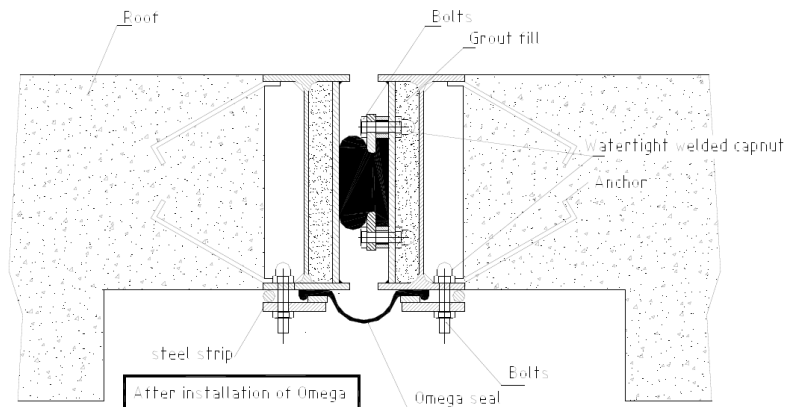


Figure 2-2 Gina-Omega Seal Solution (Trelleborg Ridderkerk Brochure)

2.1.2. Soil inside Joint Gap

Following assembly of elements and construction of joint seals, the trench in which the immersed tunnel is placed upon is backfilled to the required height of soil cover. The typical backfill material usually consists of a thin rock layer that functions as protection against anchors along with layers of sand on top. However, parts of the tunnel that were built inland usually require thicker layers of sand as the soil cover.

2.2. Soil Behavior

Understanding the behavior of soil under certain conditions and a particular type of loading is crucial to comprehending the phenomenon that occurred in the tunnel joints. The soil inside the immersion joints underwent a combination of cyclic loading due to apparent seasonal changes in temperature which led to an increase in density. The common behavior of soil under cyclic loading and the densification of soil in daily practice are discussed in this section.

2.2.1. Cyclic Loading of Soil

The term cyclic loading generally implies a state of loading that is non-static and non-monotonic, with certain magnitudes and frequencies. Under cyclic loading, soil exhibits drastically different behavior than statically loaded soils. The differences in behavior could be divided into 3 factors (O'Reilly, 1991):

- Stress reversal, the changes in the sign of the rate of loading
- Rate-dependent behavior of soil
- Dynamic effects.

As the drastic changes in temperature occur seasonally, the contraction-expansion motion of the tunnel linings also occurs annually. Thus the frequency of the cyclic loading of this project is considered to be very low. Therefore this report will focus more on the effects of stress reversals in dynamic loading due to the fact that under low-frequency loading, the soil would be less affected by the rate of loading and the dynamic effects would not have a much significant effect.

The event of stress reversal, in which the rate of loading changes from positive to negative or vice versa, has a significant impact on the behavior of the soil. It is shown in Figure 2-3 (left) that soil generates irrecoverable strains, which means that the soil displays a certain degree of damping under cyclic loading. This behavior is called the hysteretic behavior of soil, which suggests that soil has an ability to absorb and dissipate the energy received from the load.

Figure 2-3 (right) shows that soil displays a sudden increase in stiffness as stress reversal occurs. However, the stiffness would subsequently decrease as the soil continues to experience loading.

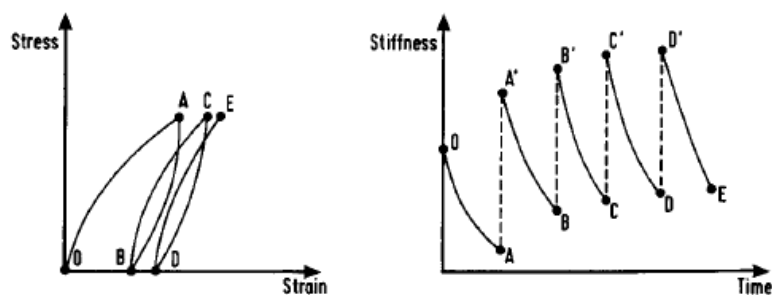


Figure 2-3 Effects of Stress Reversal (after O'Reilly & Brown, 1991)

Cyclic loads also have an impact on the shear strength of the soil. Undrained soils reduce in shear strength when under cyclic load, as demonstrated by the stress path shown in Figure 2-4 (left). The shear stress state steadily decreases to the point of touching the failure surface. This phenomenon is caused by the generation of excess pore water pressure as more cycles of loading are applied to the soil, as shown in Figure 2-4 (right).

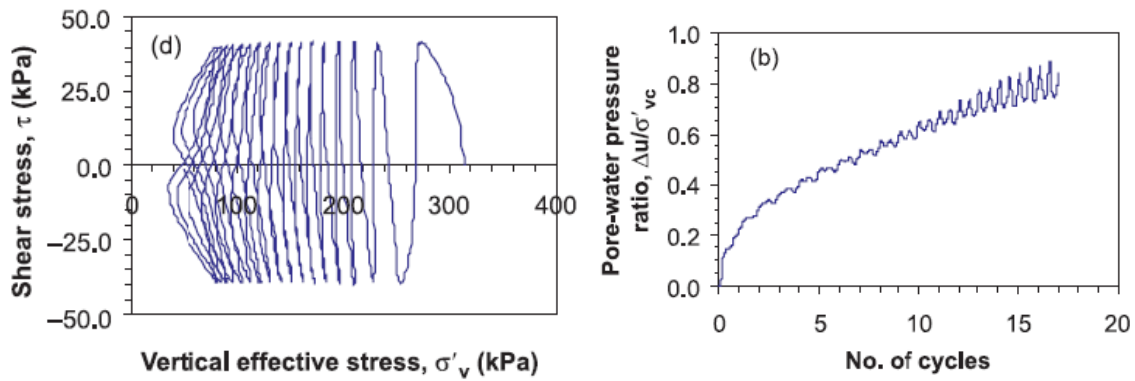


Figure 2-4 Undrained Soil under Stress-Controlled Cyclic Loading (after Wijewickreme et al., 2005)

Not unlike the soil under stress-controlled tests, soil also behaves similarly under a strain-controlled system. The soil initially exhibits high stiffness, which subsequently decreases after each cycle is completed, as demonstrated in Figure 2-5. This condition is more akin to the immersed tunnel in question and also the test procedures that will be performed on the scaled model.

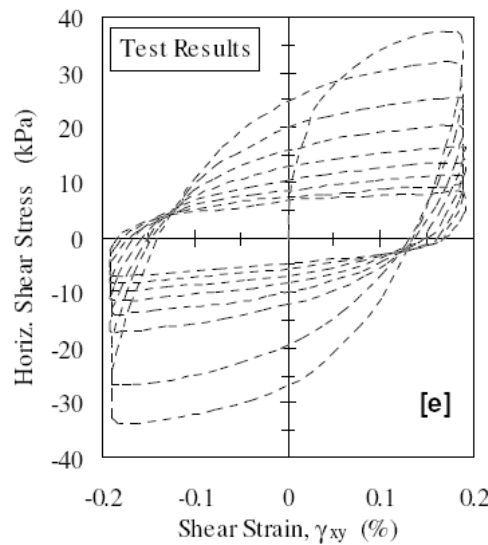


Figure 2-5 Constant Strain Cyclic Load Test (after Beaty & Byrne, 1998)

2.2.1.1. Discussion on Cyclic Loading & Soil inside Immersion Joint Gap

The detrimental effects of cyclic loading are much more pronounced on the saturated granular soil. The phenomenon of liquefaction is the leading cause of the decrease in soil shear strength. However, this presents several noticeable problems pertaining to both the project and the research.

Liquefaction may only occur on fully saturated, or at the very least moist soil. The soil inside the joint gap is located under the water table, thus it is safe to assume that the soil is fully saturated. However, as explained in part 1.4, the experiment will be performed on dry soil, and therefore liquefaction would not likely be the main failure mechanism.

Liquefaction also may only occur under high-frequency loading, where the build-up of excess pore water pressure reduces the shear strength of the soil. The load exerted by the linings have a very low frequency, as it occurs annually and might be more akin to long-term drained loading rather than short-term undrained loading.

2.2.2. Densification of Soil

A soil skeleton is comprised of 3 distinct parts: solid, water void, and air void. Densification of soil in conventional term is often specified as compaction or short-term densification, which separates it from the consolidation process or long-term dissipation of pore water pressure.

Densification of granular soil occurs due to the removal of the void-containing air. The process requires an external source of mechanical energy to be applied to the soil skeleton in order to re-orientate the soil particles to expulse air. In daily practice, the external mechanical energy originates from the application of either static load, cyclic load or both.

Moisture content plays a significant role in the process of compaction. A dry soil specimen is relatively stiffer and harder to compact due to its high inter-granular friction resistance. The addition of water in the soil skeleton produces a condition where the water acts as lubrication between the soil grains, therefore promotes rearrangement of the grains themselves while reducing the volume of air.

During compaction, the air void inside the soil skeleton gradually decreases at a different rate for every moisture content. However, after a certain moisture content, the unit weight of the soil decreases. This is due to the fact that the air void had disappeared entirely, and the water had taken the space that the solid particles would otherwise have. This moisture content threshold is defined as the Optimum Moisture Content (OMC). An illustration of this phenomenon is shown in Figure 2-6, where Williams (1949) had compared the effects of different moisture contents on the final density of the soil. It is shown that for both the A.A.H.S.O test and the modified A.A.H.S.O test, the density vs. moisture content curve displays an apex at the optimum moisture content and proceeds to decrease in density asymptotically with the zero air void line.

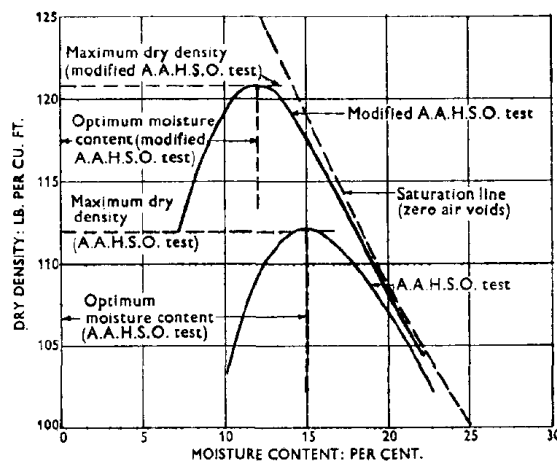


Figure 2-6 Effect of Moisture Content on Dry Density of Soil (after Williams, 1949)

Figure 2-6 also showed another factor that had an effect on the densification of soil: the compaction energy. The modified A.A.H.S.O test was developed by the US Engineer Department to give a heavier standard of compaction. When compared to the original A.A.H.S.O test, the densification rate of the soil is clearly more rapid, which proves that higher amount of compaction translates into higher soil dry densities. A similar, albeit more detailed experiment, was performed by Williams (1949) by comparing different rammer sizes, weights and fall heights against different kinds of soils. The results of the experiments are demonstrated in the graph shown in Figure 2-7. Rammers with higher energies are able to produce higher soil dry densities

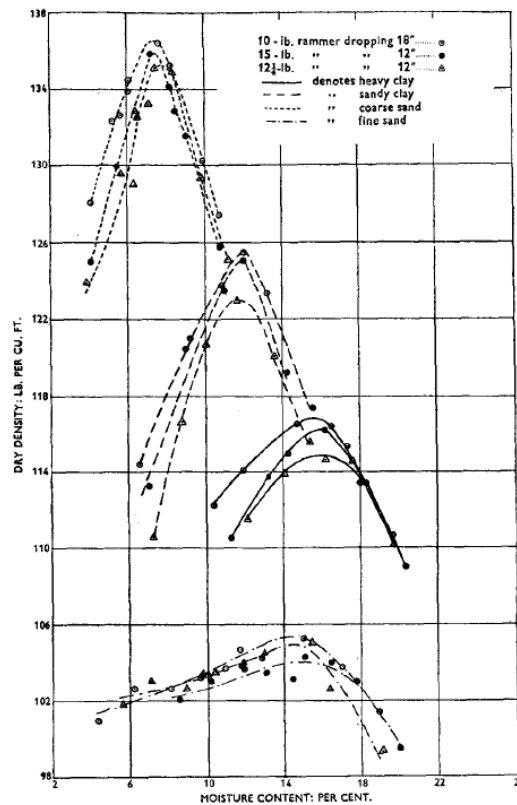


Figure 2-7 Dry Density/Moisture Content Relationships for Various Soil Types and Various Compaction Energies (after Williams, 1949)

2.2.2.1. Dynamic Compaction of Soil

Dynamic compaction is the most used method of compaction in practical applications as it allows for much higher compaction energy outputs by utilizing kinetic energy. The most common forms of dynamic compaction are the following:

- a. Impact ramming, with equipment such as rammers, pounders, and hand tamping.
- b. Vibrations, with equipment such as soil vibrators and vibro-rollers

Both the impact load and the high-frequency load exposes the soil to high energy in a short period of time. The energy forces the soil grain particles to rearrange into a denser state. This energy is transformed into both compression and shear waves that travel along the soil body (Bo et al., 2009). The combination of compression and shear waves are able to overcome the granular interlocking stresses and rearrange the configuration of the soil skeleton. In a saturated sand, as it is in the case of this project, the sudden transfer of energy by the compression waves triggers liquefaction in the sand, which decreases its shear stress and enables easier compaction.

2.2.2.2. Static Compaction of Soil

The second form of compaction is performed by applying static load on the soil. The soil is subjected to high magnitudes of pressure that is able to overcome the interlocking mechanism and rearrange the soil particles. The most common use of pressure based compaction in daily practice is the mechanical roller, which transfers energy to the soil depending on the weight of the roller and the number of passes.

The low rate expansion and contraction of the soil inside the joint gap in the Metrotunnel is more akin to the static compaction, where slowly increasing load is imparted to the soil. Venkatarama Reddy & Jagadish (1993) performed static compaction experiments on low plasticity clayey soil. The loading setup follows a variable peak stress-constant stroke compaction scheme, where multiple soil blocks with various densities are gradually compressed to a specific volume following the same stroke length. The experiment results show that with increasing moisture content, the lesser is the force required to perform compaction. The graph correlating between compaction stroke and force is provided in Figure 2-8.

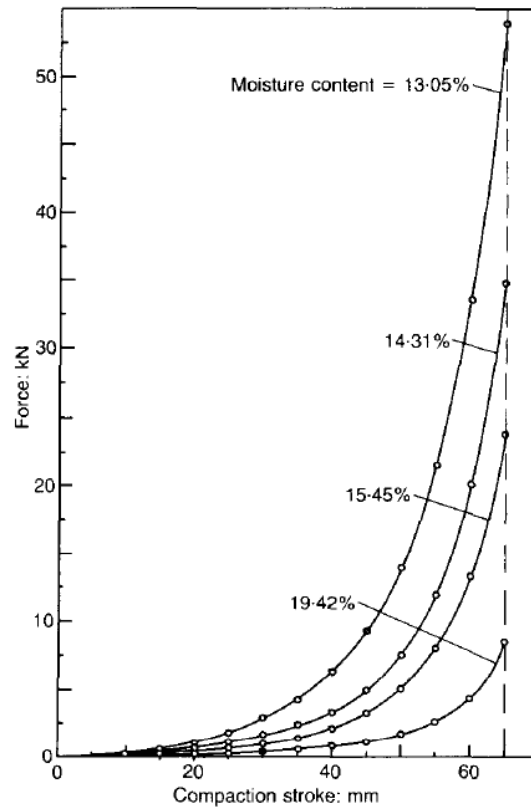


Figure 2-8 Force vs. Stroke Length for Soil with Bulk Density of 20.11 kN/m^3 (after Venkatarama Reddy & Jagadish, 1993)

Therefore, theoretically, a dry soil specimen would require much greater force to compact than a fully saturated soil. This factor is crucial to note, as the field condition of the tunnel is a contrast to the configuration of the lab equipment. The sand inside the joint gap is most likely fully saturated, while the sand in the lab equipment would be mostly dry.

It is important to note that the process of energy transfer during dynamic compaction differs considerably compared to static compaction. The impact forces of dynamic compaction are high in magnitude. However, the area in which a single impact force is exerted upon is usually much smaller than the entire soil specimen. For example, a hand tamper or a frog rammer has a tiny contact area compared to the field that it is compacting, which allows for the soil to form a bulge around the contact area. In a static compaction condition, however, a uniform load is pressed upon the entire area of the soil specimen, which does not allow the soil to deform in any direction other than compaction. The static compaction process might transfer energy more efficiently throughout the soil specimen compared to the dynamic compaction (Venkatarama Reddy & Jagadish, 1993)

Venkatarama Reddy & Jagadish (1993) also compared the results of a standard Proctor test and the static compaction test, as shown in Figure 2-9. It is shown that for the same energy of 0.6 MJ/m^3 at the optimum moisture content, the soil densifies much more for the static compaction compared to the proctor test. However, when comparing a dry soil specimen, the densification results obtained from the static compaction test is less than the proctor test. This is due to the fact that without the presence of water, it takes much more force to overcome the interlocking stress. And while the load in a static compaction test is uniform, it might not suffice to exceed some of the inter-particle friction resistance. However, despite it being local in the area, the dynamic compaction exerts more energy in a single blow, allowing it to overcome the interlocking stresses and rearrange the grains.

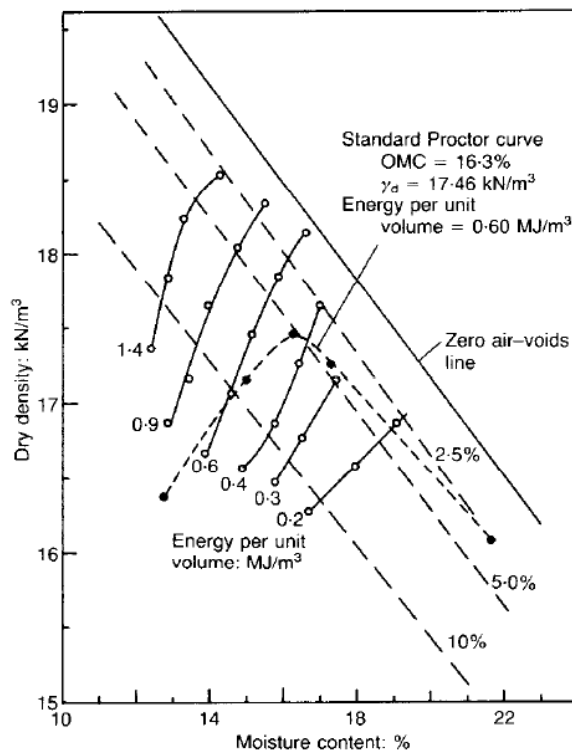


Figure 2-9 Comparison between Results of Static Compaction Test (Full Lines) and Standard Proctor Test (Dashed Line). (after Venkatarama Reddy & Jagadish, 1993)

2.2.2.3. Cyclic Loading of Piles

Multiple experiments have been conducted regarding the effects of cyclic loading of single or grouped piles on the soil. A number of experiments show that the soil beneath the pile tip tends to densify and fail while under cyclic load. Tsuha et al. (2012) performed experiments that involved multiple instances of loading, both static and cyclic, on a scaled model pile. The loading conditions of the experiment are shown in Table 2-1.

While the number of cycles is substantially larger compared to the Metrotunnel experiment, the cycle period of loads are comparable. The mean cyclic period ranges from 0.5 to 2.17 minutes for multiple two-way-loaded cycles, which is similar to the 0.5 minutes cycle of the Metrotunnel experiment. A pile is deemed stable when no failures or large displacements were recorded throughout the entire 1000 cycles of loading. Unstable piles experience failure at less than 100 cycles. Failure occurs if either of the following conditions is met: displacement that exceeds 10% of the pile diameter or displacement rates that exceed 1 mm/100 cycles.

The results of this experiment are displayed in the graph shown in Figure 2-10. It was obtained from the test results that the tests that result in stable piles occur only on piles with one-way loading. However, at higher magnitudes loads, the piles tend to fail even for one-way loads. This phenomenon might have happened due to the fact that the tests apply virtually zero tension load on the soil. Hence the load is only taken by the soil compressive resistance, and failure occurs when the load is higher than the soil resistance. Two-way loads generally cause failure to the piles, presumably due to the tension load allowing the sand to lose its stress state and collapse into a denser configuration.

Tests ICP1-TW1 and ICP2-TW1 have the most similar conditions to the Metrotunnel experiment. Both are displacement controlled tests at 100 cycles of two-way cyclic loading. Both tests resulted in unstable piles that had failed at 4 load cycles. Tests ICP3-TW2 and ICP4-TW1 are load controlled tests that have similar conditions to the Metrotunnel experiment, where the magnitudes of both compression and tension loads are the same. Both tests also yield failure on the piles, albeit after a greater number of cycles.

Table 2-1 Various Loading Conditions on Scaled Model Pile (after Tsuha et al., 2012)

Installation	Cyclic test	N_f cycles applied	Control mode	Mean cyclic period T (min)	Q_{cyclic}/Q_T	Q_{mean}/Q_T
Mini-ICP1	ICP1-OW1 Meta-stable	1000	Load control: from 0 to -4.0 kN	0.58	0.22	0.22
	ICP1-TW1 Unstable	100 ($N_f=4$)	Displacement control From -4 to $+5$ mm per cycle	2.64	0.41	0.06
Mini-ICP2	ICP2-OW1 Stable	1000	Load control: from 0 to -3.0 kN	0.43	0.12	0.12
	ICP2-OW2 Stable	1000	Load control: from 0 to -4.8 kN	0.70	0.20	0.20
	ICP2-OW3 Meta-stable	500	Load control: from 0 to -6.8 kN	1.04	0.28	0.28
	ICP2-TW1 Unstable	100 ($N_f=4$)	Displacement control From -2 to $+3$ mm per cycle	2.17	0.48	0.15
Mini-ICP3	ICP3-OW1 Unstable	100 ($N_f=66$)	Load control: from 0 to -9.6 kN	1.64	0.38	0.38
	CP3-TW1 Unstable	1 ($N_f=1$)	Load control: from -5.0 kN to $+8.0$ kN (shaft load: $-5-6.67$ kN)	6	0.54	-0.08
	ICP3-TW2 Unstable	199 ($N_f=165$)	Load control: from -5.0 kN to $+5.0$ kN (shaft load: $-5-3.80$ kN)	0.73	0.40	0.06
	ICP3-TW3 Unstable	50 ($N_f=10$)	Load control: from -5.0 kN to $+7.0$ kN (shaft load: $-5.0-4.65$ kN)	1.04	0.44	0.02
	ICP3-TW4 Unstable	37 ($N_f=3$)	Load control: from -5.0 kN to $+10.0$ kN (shaft load: $-5.0-4.53$ kN)	2.16	0.44	0.02
Mini-ICP4	ICP4-OW1 Stable	7000	Load control: from 0 to -3.5 kN	0.43	0.15	0.15
	ICP4-TW1 Meta-stable	600 ($N_f=580$)	Load control: from -4.0 kN to $+4.0$ kN (shaft load: $-4.0-2.4$ kN)	0.44	0.23	0.06
	ICP4-OW2 Meta-stable	50 (Test incomplete)	Load control: from -2.3 to -4.6 kN	0.18	0.21	0.63

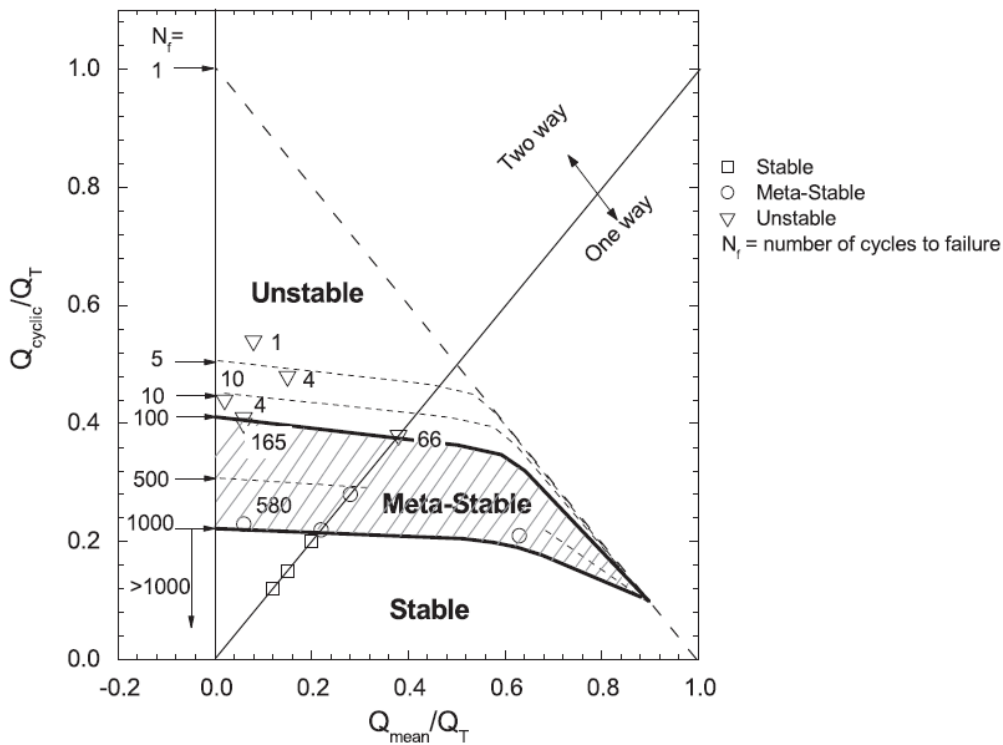


Figure 2-10 Pile Loading Experiment Results (after Tsuha et al., 2012)

The results of this experiment concluded that large displacements occur in dry sand due to cyclic loads. Two-way cyclic loads display different behavior compared with one-way loads. Figure 2-11 (a) shows that two-way loading of pile show an initial failure in the soil structure, followed by a steady increase in soil stresses, which indicates that densification occurred. Figure 2-11 (b) shows that with a one-way loading scheme, the stresses tend to decrease with increasing number of cycles, which does not indicate densification.

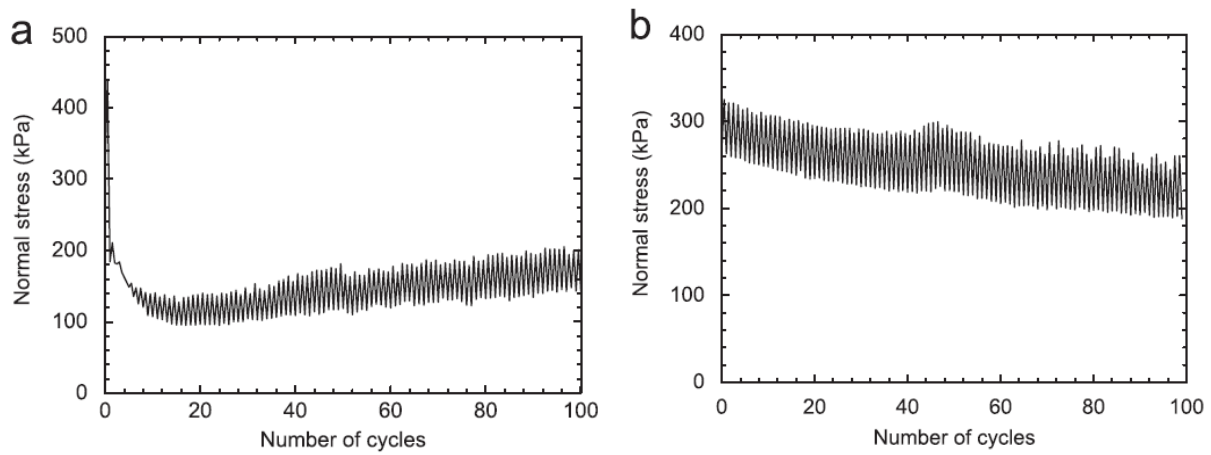


Figure 2-11 Normal Soil Stress throughout Loading Cycles (a) Two-Way Loading, (b) One-Way Loading (after Tsuha et al., 2012)

2.2.2.4. Stress Densification

Stress densification occurs naturally on soils at lower depths due to the high overburden stresses. The effects of stress densification vary with different types of sand. Park and Byrne (2004) argues that under confined conditions, the densification effect of soil is more pronounced. Park and Byrne (2004) formulated an equation that simulates the density increase in soil due to high stresses. The changes in density are expressed as follows:

$$D_r = D_{r0} + \alpha \frac{\sqrt{\sigma'_v}}{P_a}$$

Where the constant α is expressed as:

$$\alpha = \left(\frac{1 + e_{max}}{e_{max} - e_{min}} - D_{r0} \right) \frac{2(1.5 - D_{r0})}{C}$$

The above-mentioned equation contains the constant C , which is the material stiffness property of the sand. The value of C varies with different types of sand, and changes in the value would greatly affect the densification behavior of the sand. Table 2-2 shows the various values of C used in the calculations following experiments on various types of sand.

Table 2-2 Different Material Properties of Tested Sand (Park & Byrne, 2004)

Sands	Material properties						References
	G _s	D ₅₀ (mm)	C _u	e _{max}	e _{min}	C	
Brasted sand (BS)	2.68	0.25	2.42	0.79	0.48	500	Cornforth (1974)
Ottawa sand (OS)	2.67	0.40	1.54	0.82	0.50	370	Vaid et al. (1985)
Toyoura sand (TS)	2.65	0.19	1.24	0.963	0.605	300	Park (2000)
Nevada sand (NS)	2.67	0.17	2.00	0.887	0.511	220	Arulmoli et al. (1992)
Fraser River sand (FRS)	2.72	0.30	1.56	1.00	0.68	270	Park (2002) ²
Volcanic sand (VS)	2.44	0.17	2.38	1.81	0.97	105	Park (2000)
Mine tailing sand (MTS)	2.68	0.40	1.67	1.06	0.69	150	Vaid et al. (1985)
Quiou sand (QS)	2.71	0.70	4.5	1.20	0.78	100	Pestana and Whittle (1995)

Note: G_s is the specific gravity; C_u is the coefficient of uniformity.

The value of C is determined through 1D laboratory compression tests. The sand used in the experiment have not been rigorously tested to determine the exact value of C . However the sand property values might be comparable to the available data shown in Table 2-2.

2.2.2.5. Biaxial Tests on Sands

The configuration of the joint gap test equipment bears a similarity to a biaxial test apparatus. The minor axis is stress controlled at a certain overburden pressure while the major axis is steadily compressed at a controlled strain rate and the third axis is fully confined. Therefore the stress states of the sand inside the joint gap model would be comparable to stress states of sand in a biaxial test.

Desrues et al. (1985) have performed analyses regarding biaxial testing in dense, dry, coarse sand. The resulting shear band that formed in the soil sample is similar to the general shear band in the triaxial tests.

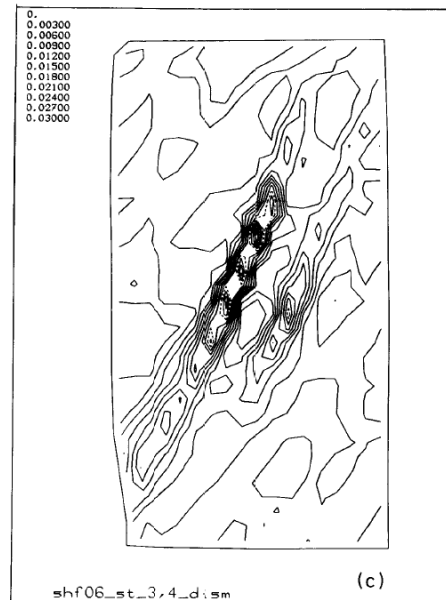


Figure 2-12 Typical Shear Band in Biaxial Tests (after Desrues et al., 1985)

Han and Drescher (1993) postulated that the thickness of the shear band depends on the magnitude of confining pressure. Their experiments show that the angle of the shear band decreases (resulting in less steep failure wedges) as the confining pressure increases.

2.2.3. Discussion on Cyclic Loading vs. Static Compaction

The events of cyclic loading and compaction on soil had been discussed in Parts 2.2.1 and 2.2.2 respectively. Both phenomena have distinct effects on the behavior of soil under different circumstances.

Project Point of View

Cyclic load is more critical when imparted upon saturated granular soil, which may result in liquefaction. This condition applies to the soil inside the actual joint gap. However, the actual load originating from the linings have a rate low enough not to be able to trigger liquefaction. Therefore if liquefaction is the leading cause of failure, the source of cyclic loading might not be due to the seasonal change of temperature, but rather the daily change in temperature. Another possible reason would be the vibrations due to passing metro trains during the entire 50-year service life.

Experiment Point of View

The experiment utilizes dry sand, as opposed to the saturated sand inside the actual metrotunnel joint gap. Hence cyclic loading, particularly at a lower load frequency, is less likely to induce neither failure nor densification. Static compaction is the leading cause of possible failure, as well as the subsequent densification that follows.

2.2.4. Soil Arching

Soil arching is a common phenomenon in a system with varying stiffnesses. A yielding soil mass transfers pressure to the adjacent stationary parts. The theory was first investigated by Janssen (1895) under the name

“silo effect,” where it was observed that the floor of silo structures bear less load than the apparent overburden pressure.

The idea was further analyzed by Terzaghi (1943), who stated that the relative movement of the yielding mass is opposed by the friction between the yielding mass and the stationary parts. An illustration of the phenomenon is shown in Figure 2-13.

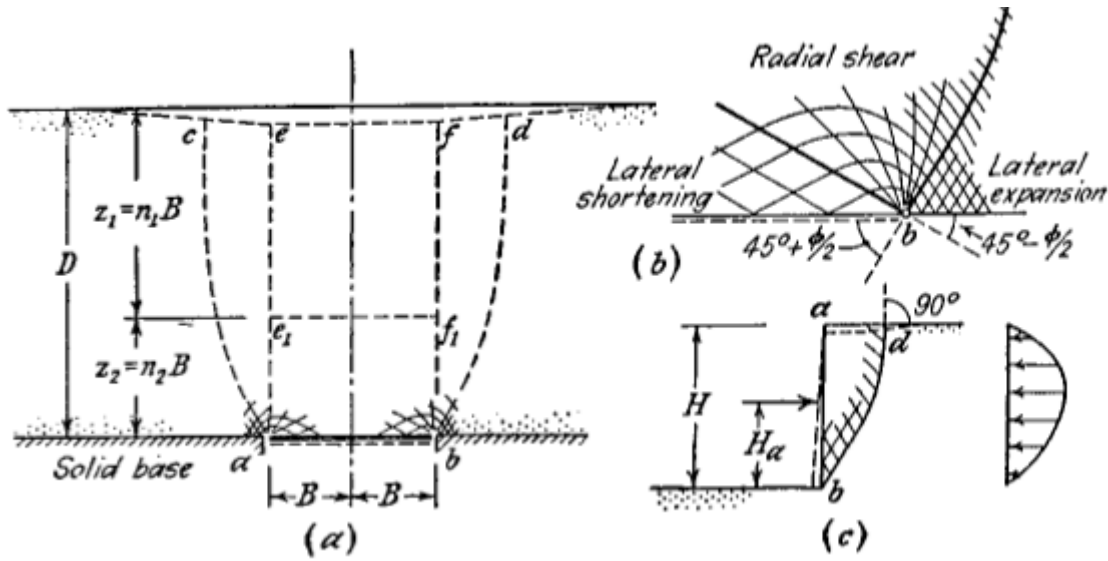


Figure 2-13 Mechanics of Soil Arching (After Terzaghi, 1943)

The general formula for the vertical soil stress undergoing an arching mechanism follows the following formula (Terzaghi, 1943):

$$\sigma_v = \frac{B \left(\gamma - \frac{c}{b} \right)}{K \tan(\phi)} \left(1 - e^{-\frac{K \tan(\phi) z}{b}} \right) + q \left(1 - e^{-\frac{K \tan(\phi) z}{b}} \right)$$

In the case of the Metrotunnel, where the friction is generated by the interaction between the soil and the tunnel lining, the equation changes into the following form:

$$\sigma_v = \frac{B \left(\gamma - \frac{c}{b} \right)}{K \tan(\phi)} \left(1 - e^{-\frac{K \tan(\delta) z}{b}} \right) + q \left(1 - e^{-\frac{K \tan(\delta) z}{b}} \right)$$

Handy (1985) and McKelvey (1994) suggests that the arch follows a catenary shape. The horizontal forces in the catenary represent the minor principal stresses as opposed to the Cartesian horizontal stresses.

2.2.5. Ground Arch/Dome Effect

The idea of a naturally forming ground arch was first proposed after experiments conducted by Whitman et al. (1962). The experiment features thin structural domes buried in granular soil and subjected to incrementally increasing loads. It was discovered that the domes require larger overburden pressure than the expected capacity to fail. Moreover, the failure points of the dome are positioned near the supports as opposed to the crown, even though the overburden pressure is kept uniform. Therefore Whitman et al. (1962) postulated that the soil forms a natural arch that is able to redistribute the loads onto the supports. They stated that the arch forms prior to the structural yielding, and restructures itself following the yield. The ability of the ground arch to withstand load following structural yield depends on the depth of the burial, where a higher soil column suggests a larger, more robust ground arch may form.

The hypothesis is further investigated by Nielson (1966), who used the theory to analyze the loads on buried conduits and the subsequent ground arch that forms. The analysis utilizes elastic theory to calculate the maximum shear stress plane above the buried conduit. The supports of the arch form on the plane following

soil particle rearrangement due to shearing. Numerical procedures were used to calculate the ground arch structure. An illustration of the calculation is shown in Figure 2-14.

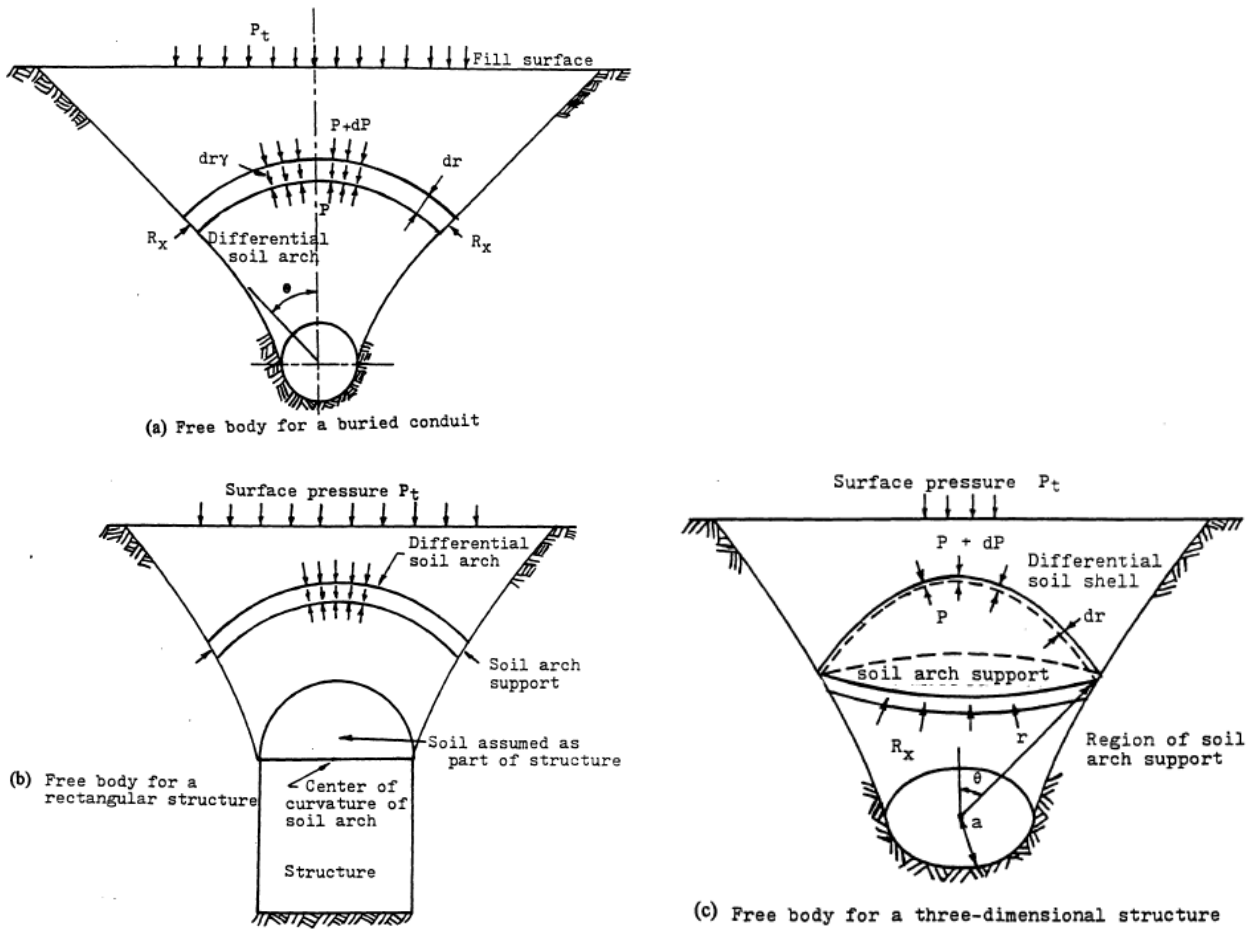


Figure 2-14 Ground Arching Effect for (a) Buried Conduit (b) Rectangular Structure, (c) Ground Dome for 3 Dimensional Structures (after Nielson, 1966)

The analysis is also extended to a buried rectangular structure, where the soil directly above the buried structure is assumed to be part of the structure. Hence the elastic maximum shear plane forms around the top of the structure.

2.2.6. Discussions on Soil Arching and Ground Arch/Dome Effect

Both soil arching and dome effect might have a role in the behavior of the sand inside the joint gap. The backfilled sand entering the joint gap might show undergo both phenomena: arching effect might be present due to the slightly yielding Gina gasket, and a natural ground arch might form right outside of the joint gap due to the high concrete stiffness compared to the yielding joint gap soil. These circumstances prevent any extra sand from outside of the joint gap to enter the system.

The subsequent loading-unloading cycles throughout the years might destabilize both the ground arch and the arching mechanism. The absence of these resisting mechanism might allow for the backfilled sand to enter the system, thus densifying the sand inside the joint gap and exerting more pressure on the Gina gasket.

2.3. Measurement Instruments

The test equipment will use several measurement instruments to quantify the data obtained in the experiments. Therefore a detailed look into the theory behind the instruments is required. This section discusses past experiments that utilize similar instruments, as well as correlations of data obtained by the instruments to the properties necessary for the analysis.

2.3.1. Cone Penetrometer Test

The cone penetrometer test (CPT) is a form of in situ soil test suitable for medium to soft soil. The test involves inserting a 3 cm rod into the soil and measuring the resistance that it records. The aims of the cone penetrometer test are included as follows (Ameratunga et al., 2016)

- Soil Classification
- Correlations between soil strength & compressibility
- Correlations with unit weight
- Correlations with foundation resistance
- Correlations with SPT
- Correlations with permeability

Two types of data are recorded, namely the cone resistance, and the cone + sleeve resistance. The data could be analyzed further to obtain the friction ratio following the formula below.

$$R_f = \frac{f_s}{q_c}$$

The method of soil classification using CPT data was summarized by Robertson et al. (1986), utilizing the cone resistance (q_c) measurement readings and the friction ratio. Robertson stated that certain types of soil possess certain combinations of the aforementioned readings. The soil classification graph is shown in Figure 2-15

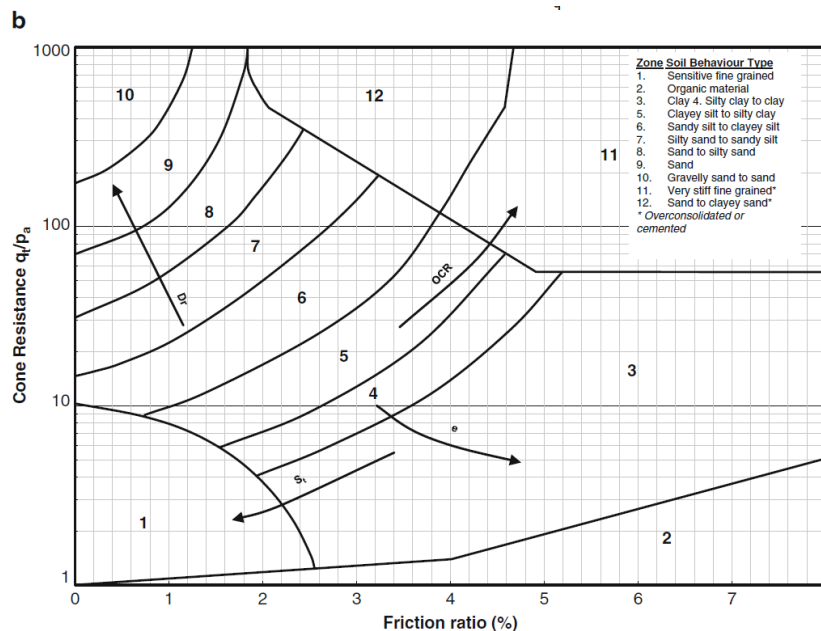


Figure 2-15 Soil Classification using CPT Data (Robertson et al., 1986)

Multiple research projects performed in the past had claimed that the soil density could also be correlated to the cone resistance. A commonly used relationship was proposed by Kulhawy and Mayne (1990) which takes into account the overconsolidation ratio of the soil. The correlation formula is as follows:

$$D_r^2 = \frac{Q_{cn}}{305 Q_c Q_{OCR}}$$

Where:

$$Q_{cn} = \frac{\left(\frac{q_c}{p_a}\right)}{\left(\frac{\sigma'_v}{p_a}\right)^{0.5}}$$

Q_c = Compressibility factor (0.91 for high, 1.0 for medium, 1.09 for low)

$$Q_{OCR} = OCR^{0.18}$$

Research conducted by Schmertmann (1976) obtained the following correlations for normally consolidated (NC) sand:

$$D_r = \left(\frac{100}{C_2}\right) \ln\left(\frac{q_c(MPa)}{C_0(\sigma'_{v0})^{C_1}}\right)$$

Coefficients C_0 through C_2 for different types of sand is listed in Table 2-3.

Table 2-3 Values of Correlation Coefficient for Various Sands (after Sadrekarimi, 2016)

	Sand	C_0	C_1	C_2	Reference
a	Several normally-consolidated sands	0.050	0.700	2.91	Schmertmann (1978)
b	Ticino	0.157	0.550	2.41	Baldi <i>et al.</i> (1986)
c	Hokksund	0.086	0.530	3.29	Baldi <i>et al.</i> (1986)
d	Ticino	0.140	0.550	2.90	Jamiolkowski <i>et al.</i> (2001)
e	Ticino, Toyoura, Hokksund	0.175	0.500	3.10	Jamiolkowski <i>et al.</i> (2001)

Another relationship suggested by Jamiolkowski et al. (2001) suggested a modified form of the Kulhawy and Mayne equation as follows:

$$D_r(\%) = 26.8 * \ln Q_{cn} - b_x$$

Where $b_x = 52.2, 67.5$ and 82.5 for high, medium and low compressibility sands respectively.

2.3.1.1. Pocket Penetrometer Test

The actual measurement in the test equipment will be performed using a pocket penetrometer instead of a full-scale cone penetrometer. The main difference between the two devices is the size. The CPT rod has a diameter of 3 cm and is suitable for large depths of testing. On the other hand, the pocket penetrometer probe only has a diameter of 10 mm and has a testing depth of approximately 0.25" in its unmodified state.

A pocket penetrometer only records the cone resistance (q_c) of the soil, as the sleeve area is considered to be too small to contribute to friction, and the device itself usually lack the means of measuring friction resistance. However, in this research project, the pocket penetrometer probe will be extended to approximately 70 mm to be able to reach the soil in the center of the joint gap model. Therefore some friction resistance is expected to be encountered, although the value will be relatively small and not corrected for.

2.3.1.2. Horizontal Penetrometer Tests

Most cone penetrometer tests are conducted on the field. Thus the cone penetrates the soil at a vertical angle. Therefore many research regarding cone penetrometer tests in the past that have yielded empirical relationship between the cone resistance and the soil properties are valid only for vertical tests. However the laboratory test results, as is performed in this research, utilizes a horizontal set up for the penetrometer tests. Therefore several factors have to be taken into account in order to analyze the cone resistance data obtained.

Research on horizontal cone penetration conducted by Broere & van Tol (1998) produced a relationship between vertical and horizontal cone resistances. The research focused on laboratory controlled CPT tests, both vertical and horizontal, performed on a soil drum at several sand densities. The research used the assumption suggested by Salgado et al. (1997) of cavity expansion as the core principle in analyzing the CPT model.

The results yielded a ratio between horizontal and vertical cone resistances in relation with its coefficient of neutral earth pressure (K_0). The graph displaying the ratio is shown in Figure 2-16

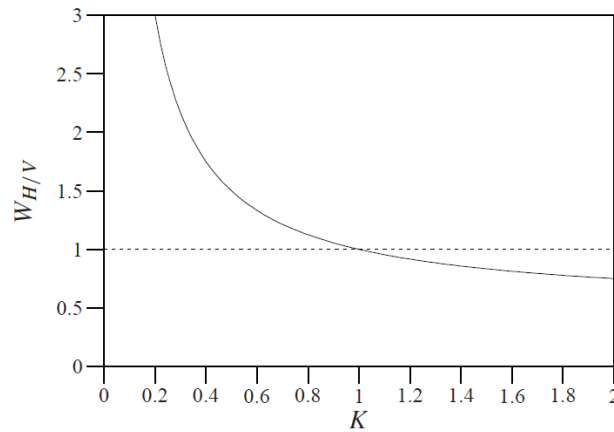


Figure 2-16 Ratio of Horizontal over Vertical Cone Resistance vs. Earth Pressure Coefficient (after Broere & van Tol, 1998)

Quantifying the graph yields the following formula: (after Broere & van Tol, 1998)

$$\frac{q_{cH}}{q_{cV}} = \frac{1 + K}{2K}$$

From the expression, it is shown that for medium sand with a K value of 0.5, which is going to be used for this research project, the value of horizontal q_c is 1.5 times that of the vertical q_c .

2.3.2. Measurement of Soil Stresses using Load Cells

2.3.2.1. Challenges in Measuring Soil Stresses

The measurement of internal soil stresses has been challenging to deliver in geotechnical laboratory tests accurately. Askegaard (1963) suggested that soil stress measurement should be differentiated into 2 types: contact pressure and in-soil pressure.

The conclusions of Taylor (1945), Monroe (1950), Askegaard (1963) and Labuz and Theroux (2005) state that the problem with soil stress measurement of the two types of measurement configurations lies in the difference in stiffness of the cells and the soil. A load cell with a stiffer modulus compared to the soil medium would induce “passive arching” of the soil and thus produce over-registration of stresses in the sensor. A load cell with a softer modulus compared to the soil medium induces the “active arching” of the soil and would under-register the actual exerted soil pressure (Terzaghi, 1943). Both phenomena are illustrated in Figure 2-17.

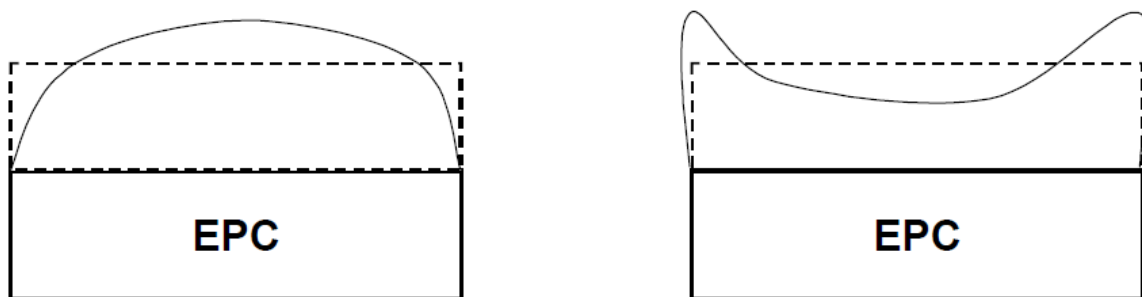


Figure 2-17 Non-uniform Distribution of Stresses in an Earth Pressure Cell. Over-registration (left) and Under-registration (right). (after Labuz & Theroux, 2005)

Contact pressure measurement simply suggests that the soil is in direct contact with the soil and built flush on a structure interface, thus theoretically unlikely for the configuration to over-register the soil stresses. However, the in-soil measurement might either over or under-register the pressure depending on the compliance of the soil (Talesnick et al., 2014).

The biggest problem with measuring soil contact pressure is the under-registration variant caused by the natural arching mechanism, where a soil body that has a tendency to move in a direction naturally forms an arc that prevents it from moving. The stresses that were previously exerted upon a yielding part of the body is transferred into its more rigid surroundings (Terzaghi, 1943). Therefore, in a laboratory condition, traditional load cells with flexible membranes might induce the soil arching behavior as the load increases, and the membrane deflects. The problem was addressed by Kallstenius and Bergau (1956), who suggested that a minimum number of 50-grain particles must fit in between the sensing diameter for the data to be valid. A lower limit was set by Weiler and Kulhawy (1982) at 10 particles per diameter.

The soil arching mechanism in laboratory conditions was quantified in an experiment conducted by Talesnick (2005), where the measured output from soil pressure is compared with a reference pressure originating from the pressurized air inside a latex membrane. The 2005 paper claimed that using one of the stiffest commercially available load cell transducers; the calibration coefficients had deviated much larger for dense sand compared to loose sand

The load cells used in the metrotunnel experiment are arranged to measure the soil contact pressure, with a sensing diameter plate of 10 mm. The sand used in the experiment has a grade fine to very fine. Therefore, it is assumed that the sensing diameter is large enough to contain more than 10 grain particles of sand.

2.3.2.2. Calibration Techniques

Prior to actual usage in experiments, every load cell is required to go through a calibration process. Moreover, earth pressure cells are prone to data misreading as explained in part 2.3.2.1. Terzaghi (1943) stated that the economical usage of earth pressure cells, meaning without in-soil calibration and time spent analyzing the behavior of the cells in relation to soil, the stresses obtained from the cells are nearly always unusable.

The first step in the calibration method for load cells usually involves applying a fluid load (air, water or oil) into the load cell. This application is intended to check the general condition of the cell, its response to pressure and the unloading behavior (Dave & Dasaka, 2011). The application of fluid load ensures uniform load is exerted upon the cell diaphragm, as opposed to inconsistent loading originating from other contact materials.

The application of water load was successfully used in researches conducted by Clayton & Bica (1993), Labuz & Theroux (2005), and Dave and Dasaka (2013). The water load usually originates from a modified Rowe cell or triaxial cell that allows for the load cells to be placed at the bottom of the cell. As the cells are already originally watertight, extra watertight measures are only required to keep the area around the newly installed load cell. The cells are filled with controlled pressurized water, and the cell outputs are subsequently compared to the water pressure load.

Another common method is using air pressure as the source of the load. This application has been successfully performed in the experiments conducted by Clayton & Bica (1993), and Talesnick (2005). The calibration apparatus is a cell lined with an expandable material (latex or rubber), while the load cell is positioned at the bottom of the cell. The rubber material is subsequently filled with pressurized air which is measured by a manometer. The cell output is subsequently compared with the manometer readings.

The second step involves applying actual soil load to the load cell. The soil is placed directly in contact with the sensing plate, with controlled relative density. The load may originate from the dead load of the soil itself, or through an external overpressure originating from the air pressure (Talesnick, 2005). The load cell output is subsequently taken and compared to the load applied to the sample.

The relationship between fluid and soil pressure measurements is described by the concept of a cell action factor (Dave & Dasaka, 2013). The cell action factor is simply the ratio between the measured pressure and the applied cell pressure, which follows the expression:

$$CAF = \frac{P_{measured}}{P_{applied}}$$

A value of 1 for the CAF indicates that the load cell registers the exact applied force. Lower CAF values might indicate that the load cell is less sensitive to soil loads. However, having the knowledge of the CAF value of the cell-soil configuration would enable the best possible calibration for the output of the load cell.

2.3.2.3. Factors Affecting Sensor Output

Several factors influence the output of the earth pressure cells. A review paper written by Dave & Dasaka (2011) focuses on various factors that may affect the accuracy of earth pressure cell readings. A summary of the factors is listed in Table 2-4. Several of these effects that pertain to the immersion joint gap experiment will be discussed further.

Table 2-4 Factors Affecting Earth Pressure Cell Output (after Dave & Dasaka, 2011, adopted from Weiler and Kulhawy, 1982)

Factors Affecting Stress Derivation	Description of Resultant Error	Correction Method
<i>Inclusion effects</i>		
Aspect ratio (cell thickness to diameter ratio)	Cell thickness alters the stress field around the cell	<ul style="list-style-type: none"> ▪ Use thin cells ($T/D < 1/5$) (Experimentation Station, 1944) ▪ Minimizing aspect ratio increases accuracy (Askegaard, 1963 and Collins et al., 1972)
Stress concentrations at cell corners	Causes cell to over-register by increasing stress over active cell face	<ul style="list-style-type: none"> ▪ Use inactive outer rims to reduce sensitive area $d^2/D^2 < 0.25-0.45$ (Monfore, 1950), Peattie & Sparrow, 1954) ▪ Active cell diameter to grain size ratio $d/D_{50} > 10$ (Weiler & Kulhawy, 1978)
Cross-sensitivity	Non-uniform direct lateral compression of cell causes error in measurement	<ul style="list-style-type: none"> ▪ Consider strain gauge arrangement, add outer ring (Brown & Pell, 1967)
Proximity of structures and other stress cells	Interaction of stress fields of cell and structure causes errors	Observe minimum distance between cells <ul style="list-style-type: none"> ▪ Horizontally – 1.5D ▪ Vertically – 4D ▪ From face of structure to edge of cell – 0.5D
Stress-strain behavior of soil	Cell measurements are influenced by confining conditions	Calibrate cell under near usage conditions
<i>Cell/soil interaction</i>		
Soil-cell stiffness ratio	Incompatible stiffness between cell and soil may cause nonlinear calibration	Cell-soil stiffness ratio ≥ 0.5 (Kogler & Scheidig, 1927) i.e. use stiff cell
Diaphragm deflection (arching)	Excessive deflection changes stress distribution over cell	Design cell for low deflection ($d/\Delta > 2000-5000$)
Eccentric, non-uniform and point loads	Soil grain size too large for cell size used	Increase active diameter ($d/d_{50} > 10$)
<i>Placement effects</i>		
Placement effects	Physical placing of soil causes disturbance of soil	Random error – Use duplicate measurements
Placement stresses	Over stressing of cell during soil compaction	Check cell design for yield strength
<i>Environmental effects and dynamic response</i>		
Temperature	Variation of temperature changes “zero reference” of cells: does not change slope calibration	Calibrate at operating temperature or use balance resistors
Dynamic stress measurement	Response time, natural frequency and inertia of the cell cause errors	Use dynamic calibration
Corrosion and moisture	Might cause failure or breakdown of the cell	Be particular in water proofing

Sensing Diameter

Labuz and Theroux (2005) conducted experiments by measuring the uniaxial calibration tests of Ottawa sand using a particular type of commercial load cell. The uniaxial test calibrates the load cell to the earth pressure exerted by the self-weight of the different diameters and thicknesses of the soil body. Results of the research are shown in Figure 2-18.

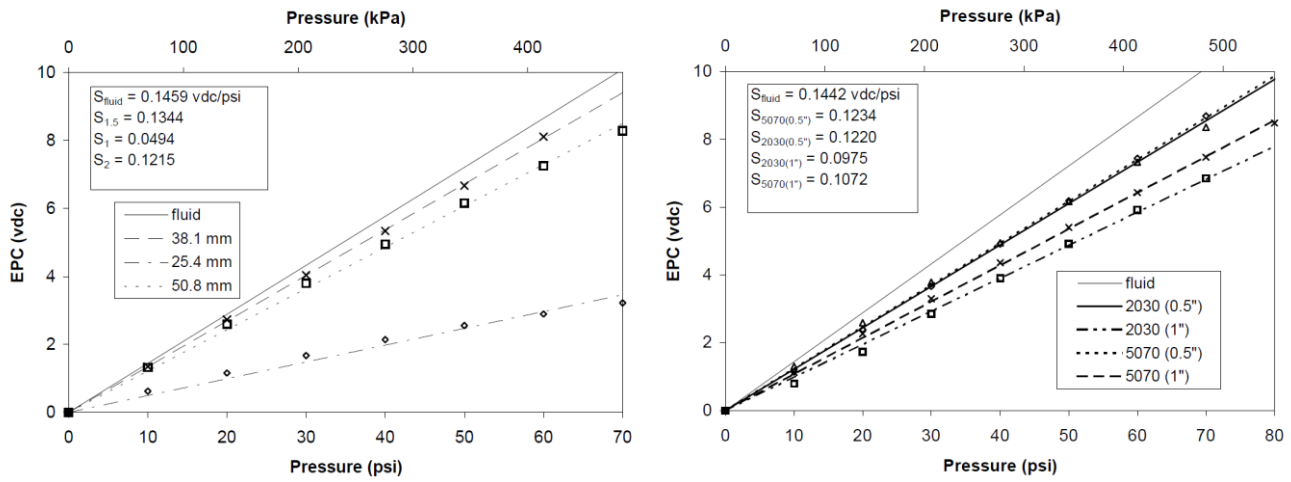


Figure 2-18 Results of Uniaxial Calibration Research for Various Soil Body Diameter (left) and Various Soil Body Height (right). (after Labuz and Theroux, 2005).

Labuz and Theroux (2005) concluded that different configurations of the soil body amount to different sensitivity in measurement. Figure 2-18 (left) shows that a ratio of soil body width to sensing diameter close to 1:1 exhibits exaggerated readings. This phenomenon is due to the low stiffness of the active sensing area compared to the soil stiffness. At the sample diameter of 38.1 mm, the sensitivity increased to nearly reaching the fluid calibration curve due to the soil using the entire sensing area and the silicone annulus ring. At 50.8 mm sample diameter, it was observed that the sensitivity had decreased. This is due to the soil body encompassing the rigid, inactive rim which induces the soil arching behavior.

The experiments were conducted on a small scale apparatus. However, Labuz and Theroux (2005) had stated that beyond the critical sample diameter of 2 times the sensing diameter, no further arching occurs. The experiments that are going to be performed in this research are on a large scale, and well beyond the critical diameter. Therefore calibrations for the load cells used in the metrotunnel experiment are best conducted on the test equipment itself, or on an apparatus large enough to accommodate soil sample diameter of 2 times the sensing diameter.

Sample Height

Figure 2-18 (right) shows the effect of soil body height compared to the sensor readings. It was obtained that taller soil samples had exhibited lower reading sensitivity on the earth pressure cells, which is also attributed to the formation of the larger active arch.

Dave & Dasaka (2013) also conducted an experiment on the effects of varying heights of soil sample on the sensor readings. The experiment involves testing a 4 cm diameter earth pressure cell against sample heights ranging from 0.25 D_{EPC} to 15 D_{EPC} on 3 types of sand. The results of the experiment are shown in Figure 2-19.

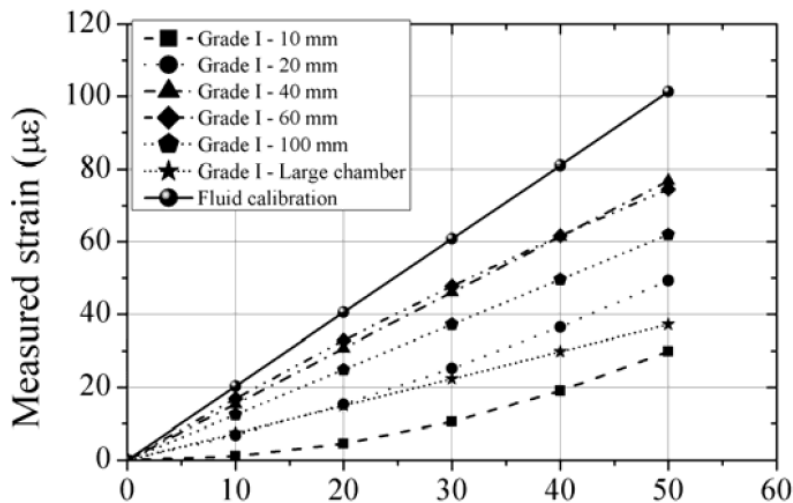


Figure 2-19 Effects of Sand Bed Thickness on Performance of Earth Pressure Cells (after Dave & Dasaka, 2013)

Dave & Dasaka (2013) had observed that at a low ratio of soil body diameter to sensing diameter, the measurements showed erratic readings and largely over-registered loads. This data agrees with the experiments performed by Labuz & Theroux (2005). At a ratio of 1.5, the sensitivity peaked with readings most similar to the fluid reference test. At higher ratio, the sensitivity further decreased with higher, more visible error as the pressure increases. Therefore it was concluded that the optimum soil sample height is at 1.5 times the sensing diameter.

As the test equipment in the tunnel model research features the soil inside a model joint gap, the load cell would most likely be placed horizontally. The 1:3 scale of the model attributes to around 35 mm of “sample height” above the load cell. Therefore to obtain an optimum sensitivity, the load cell would need to have a sensing diameter in the range of 10 – 20 mm.

Cell Aspect Ratio

The cell has to be thin enough to have a ratio between thickness and diameter less than 1:5. With lesser aspect ratio, the earth pressure cell registers more accurate results. This gives a threshold for the selected load cell for this experiment.

Proximity to other cells

The presence of other nearby earth pressure cells might affect the individual cell output. Each cell deflects when soil pressure is applied, hence generating multiple active soil arches. Overlap of the arches might render the sensor to generate more erratic and unpredictable output. In order to ensure the validity of soil stress data readings, it is likely that multiple earth pressure sensors are used in this project. The cells that are going to be employed in the immersion joint experiment would probably be positioned in a horizontal manner, due to the abundance of space in the width direction of the gap compared to the depth. Hence a range of 1.5 times sensing diameter must be maintained in order to optimize the measurement accuracy.

Soil-Diaphragm Stiffness Ratio & Diaphragm deflection

According to Weiler & Kulhawy (1982), the load cell must be designed for low deflection. The lower limit threshold for the ratio between the diameter of the diaphragm and the deflection is 2000-5000. The stiffness ratio between the soil body and the diaphragm must be greater than 0.5 to ensure compatibility in the deflection of both materials and minimizing the reading error. Currently, available load cells in the market provide load cells with very high diaphragm stiffness.

2.4. Metro Tunnel

2.4.1. History

The Rotterdam metro line was first opened to the public in 1968 as the North-South line (Noord-Zuidlijn) and was the first metro line to have been built in The Netherlands. The river Maas runs from East to West through the city. Thus the metro line needed a solution in the form of the metrotunnel.

The Rotterdam Metrotunnel is the one of the earliest immersed tunnel construction in The Netherlands. The actual construction of the tunnel began in 1965, where the tunnel elements were constructed at a temporary casting basin excavated at the side of the river. The elements were towed to the construction site and subsequently immersed and placed onto the excavated trenches under the river Maas.

In 1975, the North-South line was further extended, crossing the river Maas again and reaching Spijkenisse in the south. An extra tunnel was built, which was also an immersed tunnel with similar properties and dimensions to the original tunnel.

Both tunnels implemented the Gina-Omega gasket to prevent leakage from occurring. However, in 2015, leakage was detected along the walls of the tunnel. The leakage event implies that failure of both Gina and Omega gaskets had taken place throughout the lifetime of the tunnel. In the inspections that followed, it was found that the Gina gasket had failed prior and had loaded the Omega gasket to failure.

2.4.2. Technical Specifications

The Rotterdam Metrotunnel is a double-tubed concrete-lined tunnel designed for subway metro trains. As the tunnel was older in design, it tends to have shorter element length albeit more numerous than more modern tunnels. The metrotunnel consists of 36 elements of approximately 90 meters long each. Due to high groundwater level, some of the tunnel elements were also floated inland, which also includes station sections as well (Catalogue of Immersed Tunnel, 1997). It has a total length of 2.8 kilometers, with 1.04 kilometers under the Nieuwe Maas and 1.815 kilometers between Central Station and Leuvenhaven.

The metrotunnel is 6 meters in height and 10 meters in width. The tunnel cross-section of the tunnel is shown in Figure 2-20. The immersion joints are designed to have a gap of 100 mm in between the linings. The roof part of the joint lining has a concrete thickness of 530 mm. Detailed drawing of the joint gap is shown in Figure 2-21.

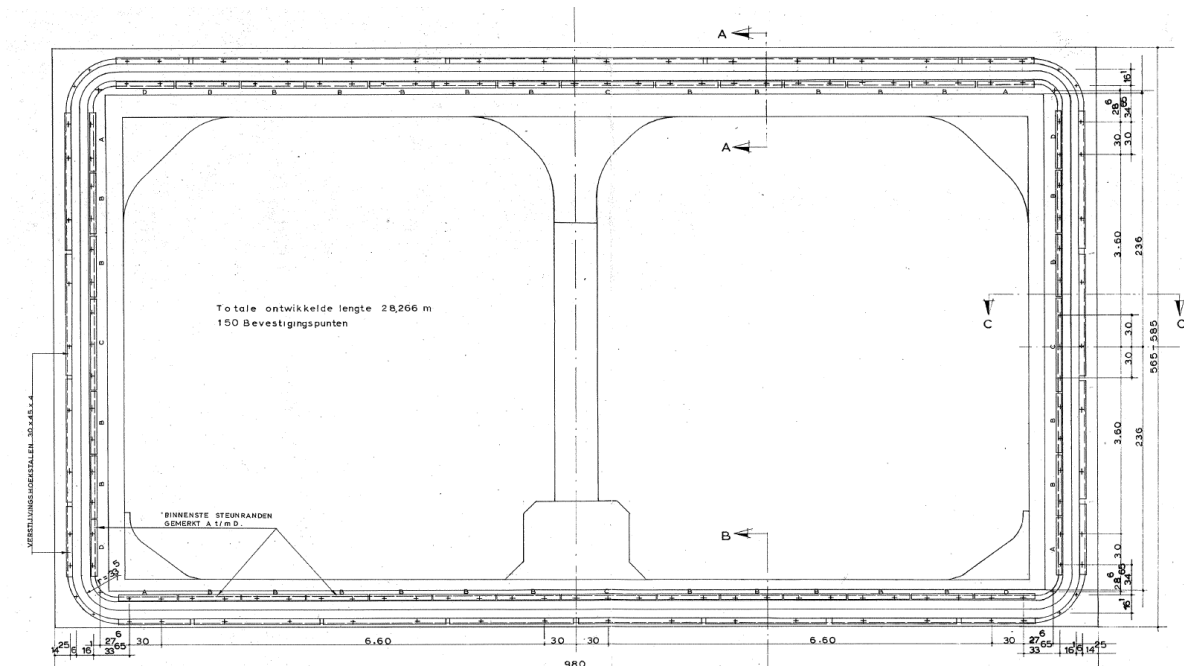


Figure 2-20 Tunnel Cross Section

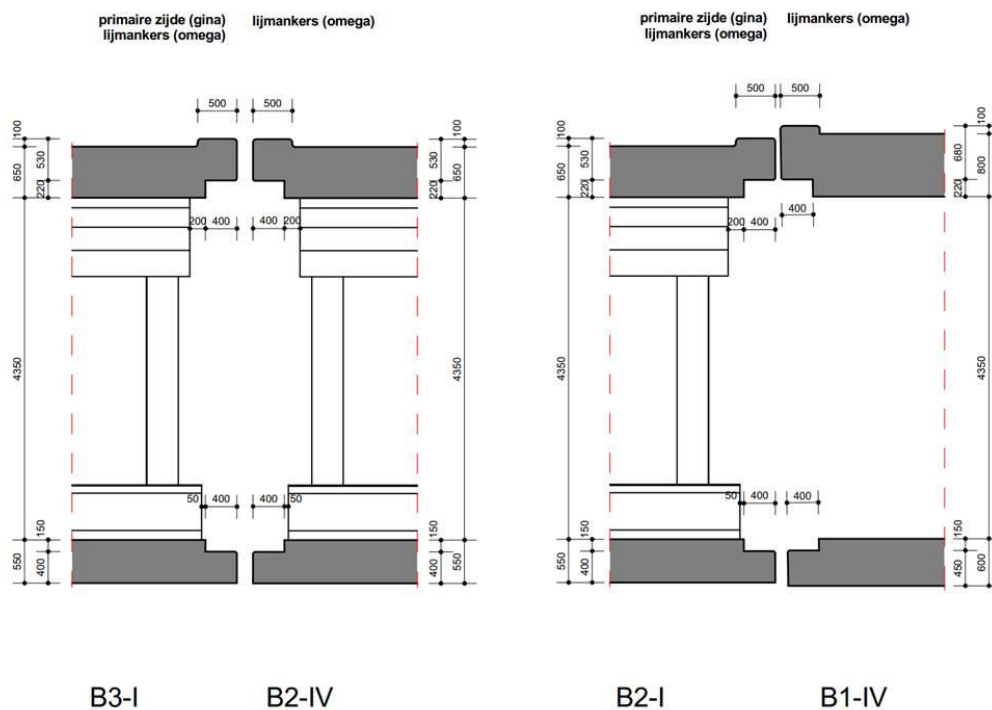


Figure 2-21 Cross Section of the Joint Gap

2.4.3. Gina Profile

The Rotterdam Metrotunnel is the first tunnel in The Netherlands to implement the Gina-Omega gasket solution. The Gina profile used in the tunnel was the Sh-50 variant provided by Trelleborg Ridderkerk B.V. The detailed drawing of the Gina gasket is shown in Figure 2-22.

The Gina gasket was designed for the 10 cm joint gap, with a total uncompressed height of 13.8 cm. The gasket is placed 20 cm from the inside of the tunnel lining, which makes it 25 cm from the outer edge of the lining. The position of the Gina gasket inside the joint gap is illustrated in the drawing shown in Figure 2-23.

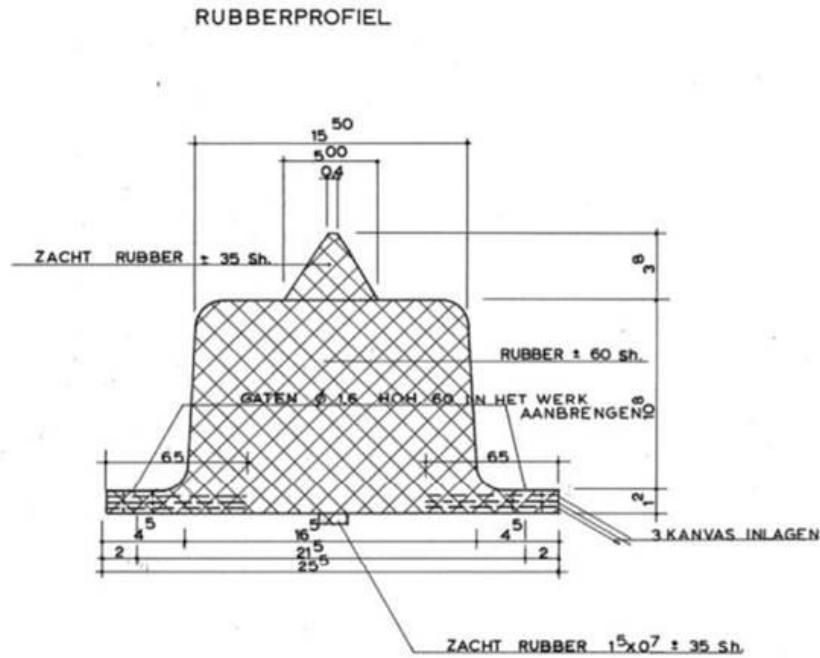


Figure 2-22 Detailed Drawing of Gina Gasket

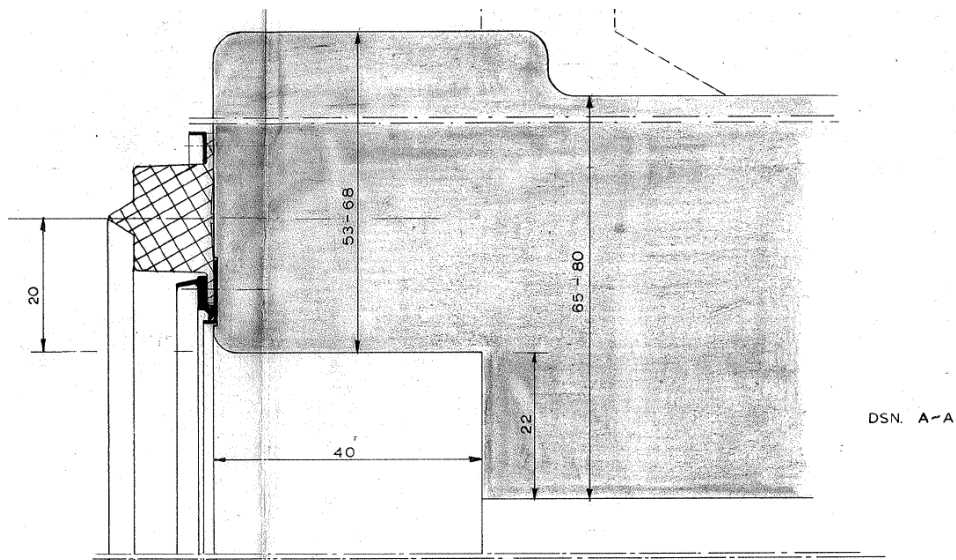


Figure 2-23 Position of Gina Gasket inside Joint Gap

Initially, the Sh-50 gasket has a Young's modulus of 2.20 MPa. However, during the service lifetime of the tunnel, the stiffness might have decreased following the graph shown in Figure 2-24 to 1.40 MPa.

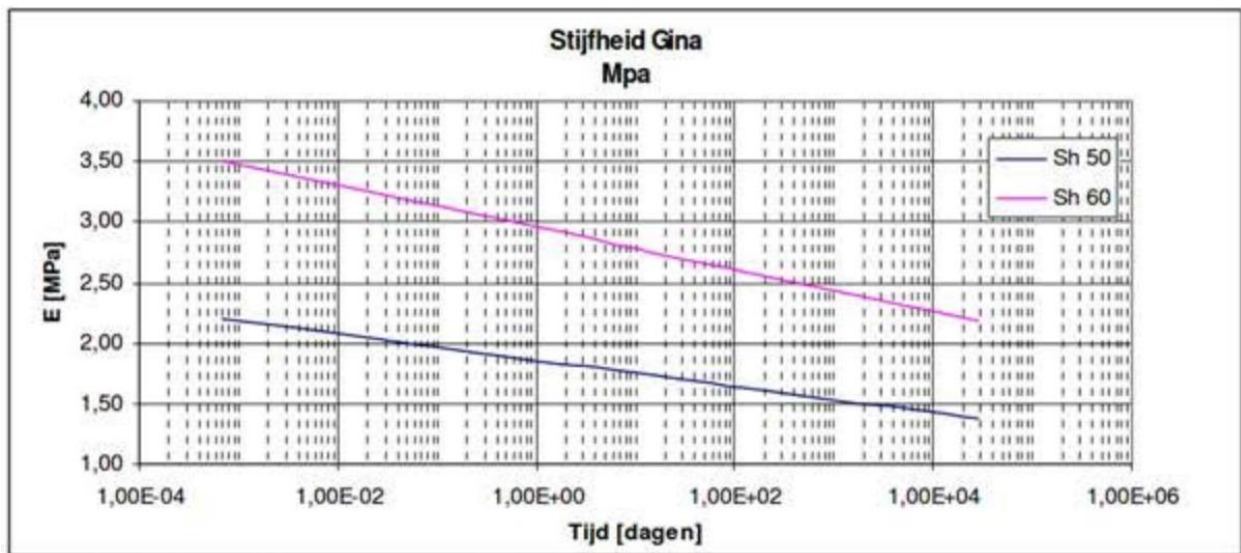


Figure 2-24 Gina Profile Stiffness Decrease Over Time

The Gina gasket was designed with a steel clamp structure on either side of the profile. The steel clamp on the inner side of the gasket has a support strip built on top of the bolt. Detailed drawing of the inner side clamp and the steel support strip is shown in Figure 2-25. Unfortunately, the deflection of the Gina profile had caused the strip to apply high moment load to the clamp. Years of repeated loading throughout the service life had fatigued the steel clamp. Thus, failure of the Gina gasket occurred.

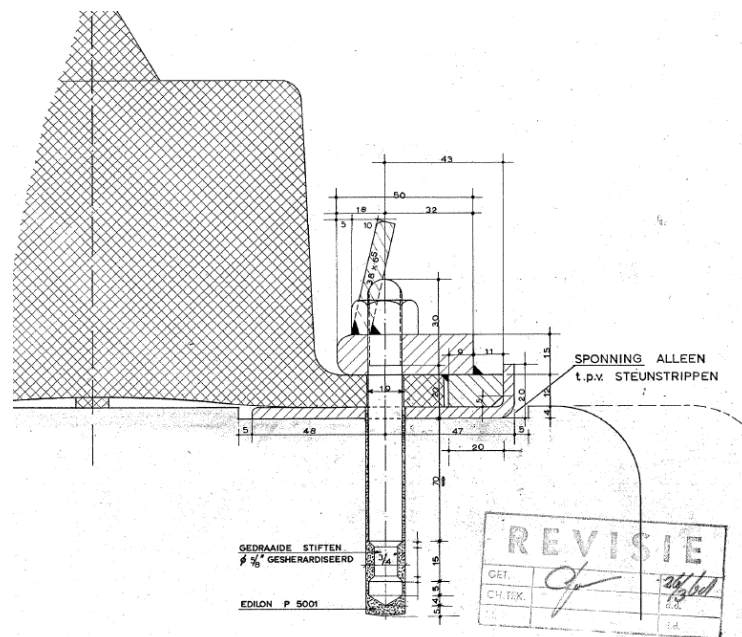


Figure 2-25 Detailed Drawing of Steel Support Strip

2.4.4. Soil Type

The field test results during the rehabilitation of the Metrotunnel shows mainly sandy soil at a depth of 2-5 meters where the tunnel roof is situated. The sand is moderately fine in grain size with a little hint of silt. Results from the field boring test are shown in Appendix B-1 and B-2.

Results of the sieve analysis laboratory experiment also show that the soil is dominated by sand at 81.4% while the silt content is 7.4%. Grain size distribution curves are shown in Appendix B-3 to B-8

The grain size distribution of the sand at depth 3-4 meters is shown in Appendix B-6. It can be observed that the values for the D_{50} and uniformity coefficient are 0.141 and 1.63 respectively. Comparing these values with the parameters displayed in Table 2-2 reveals that the sand is comparable, to an extent, with the Toyoura Sand (TS). Hence calculations regarding stress densification will utilize the parameters of Toyoura Sand.

Chapter 3 Test Equipment and Setup

3.1. Test Equipment

3.1.1. Overview

The equipment is a physical model of the outer side of the immersion joint gap. It is divided into 2 main sections:

- Section (a) models the soil column outside of the joint gap. The soil column is put inside a tubular drum container with an opening at the bottom that connects it to part (b)
- Section (b) models the immersion joint gap, which is rectangular shaped. This section houses the Gina profile pushed against the lining. The lining features a mechanism that allows it to move in a cyclic motion that simulates expansion/contraction of the joint gap throughout the seasons.

For the sake of simplicity, and considering the available materials, the joint gap model would be scaled 1:3. The side view sketch of the equipment is shown in Figure 3-1. The details of the parts are listed below:

1. **Tire.** An inflatable tire is positioned on top of the soil column. The tire could be filled with air to simulate overpressure to the soil column.
2. **Soil Drum.**
3. **Gina Profile.** The model Gina that would be pushed by the lining. The profile, at a model scale, would be supplied by Trelleborg to maintain similar properties as the actual profile.
4. **Moving Lining.** The lining is a model plate that has a mechanism to move towards and away from the Gina profile. The movement will be limited to 10 mm to simulate the actual contraction/expansion of the joint.
5. **Fixed Lining.** The other end of the model lining is fixed in position

The top edges of the lining are designed to have slight curves that mimic the actual tunnel lining. This small detail might further facilitate the densification process as the soil easily intrudes into the gap when the joint expands. Detailed description of the test equipment is discussed further in the coming sections

The test equipment utilizes multiple measuring instruments to quantify the process of stress increase and densification. To answer the research questions shown in part 1.3, several measurements have to be taken. To summarize, the required data are as follows:

- Research Question 1: A measurement in the increase in stresses
- Research Sub Question 1: A way to determine whether densification occurs
- Research Sub Question 2: A way to measure the stress state of the soil

Therefore to be able to fulfill the requirements, 3 types of instruments are used in the equipment:

1. **Load Cell.** In order to measure the increase in stresses in the joint gap, load cells are mounted flush into the static lining plate.
2. **Pocket Penetrometer.** This instrument is used to measure the cone resistance of the sand inside the model joint gap. The pocket penetrometer is mounted at the side of the joint gap model.
3. **Linear Variable Displacement Transducer.** An LVDT unit is used to measure the displacement of the Gina gasket. This transducer is built under the model joint gap with an opening to the underside of the Gina profile

Further details of the instrumentation are discussed in part 3.1.6.

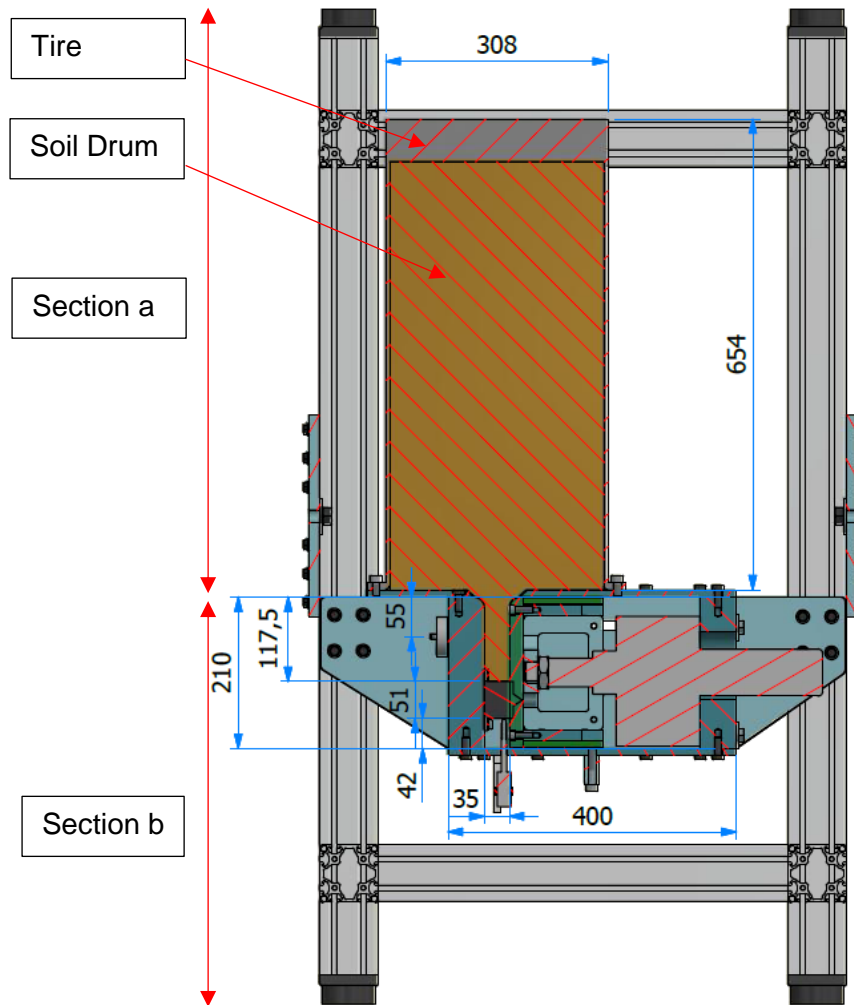


Figure 3-1 Sketch of Test Equipment (Cross Section A-A')

3.1.2. Soil Type

As discussed in part 2.4.4, the soil around the depth of the Metrotunnel roof is dominated by moderately fine silty sand. As the model is only scaled 1:3, the micro part of scaling laws, i.e., soil grain size, does not have much effect on the model. Therefore to maintain the same soil behavior as the prototype, the test equipment should also use moderately fine silty sand. The sand used in the laboratory testing is a mixture of Geba Weiss sand and fine concrete aggregate.

The two types of sand are separately sieved to determine their respective grain size distributions. The sand is subsequently carefully mixed with a ratio of 80% Geba to 20% fine aggregate to obtain a distribution graph most similar to the field sand.

The sand has a similar property to the actual sand in the tunnel joint gap. The grain size distribution of the Mixed sand shows a D_{50} value of 142 μm as well as a coefficient of uniformity of , which is comparable to 141 μm magnitude of D_{50} for the field sand shown in Appendix B-6. Comparison between both grain distributions is shown in Figure 3-2.

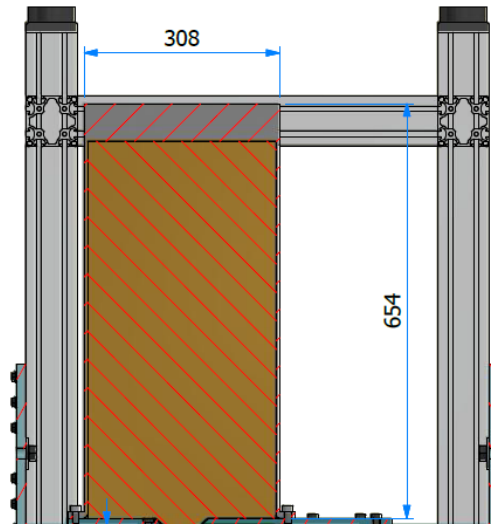


Figure 3-3 Detailed Drawing of Soil Drum (Right)

The soil drum is 30 cm in diameter at 60 cm height, as seen in Figure 3-3. The inflatable tire takes up roughly 1/6th of the height of the soil drum, at 10 cm. The soil type and unit weight used in the calculation had been discussed previously in part 3.1.2.

In order to reset the test equipment after every experiment, the entire device must be rotated and flipped around. Therefore it is important to calculate the weight of the test equipment, and thus the soil, in order to maneuver it safely. The calculations for the soil weight inside the soil drum is shown below.

$$H_{\text{Total}} := 600\text{mm} \quad H_{\text{Tire}} := 100\text{mm} \quad D := 400\text{mm} \quad H_{\text{Soil}} := 500\text{mm}$$

$$A_{\text{drum}} := \pi \cdot \frac{D^2}{4} = 0.126\text{m}^2$$

$$V_{\text{drum}} := A_{\text{drum}} \cdot H_{\text{Total}} = 0.075\text{m}^3$$

$$V_{\text{soil}} := A_{\text{drum}} \cdot H_{\text{Soil}} = 0.063\text{m}^3$$

$$\gamma_{\text{soil}} := 17 \frac{\text{kN}}{\text{m}^3}$$

$$W_{\text{soil}} := \gamma_{\text{soil}} \cdot V_{\text{soil}} = 1.068 \cdot \text{kN}$$

3.1.4. Section (b) Immersion Joint Gap

The second part of the test equipment is the actual scaled model of the immersion joint gap. The part of the joint gap filled with soil and the Gina profile itself is a 1:3 scaled model of the real tunnel. Details of the joint gap (part b) are shown in Figure 3-4. The details are as follows:

1. **Opening.** An aperture is made on the steel plate at the connecting part between the soil column and joint gap. The opening is a slightly larger rectangular hole compared to the joint gap with angled edges throughout the thickness of the plate.
2. **Load Cells.** The load cells are used to measure the stresses of the soil in the joint gap. An increase in the measured stresses may indicate densification of the soil.
3. **LVDT.** An LVDT transducer is used to measure the deformations of the Gina Gasket.
4. **Gina Profile.** The scaled model of the Gina gasket is bolted to the static lining.
5. **Static Lining.** A steel plate with stiff supports that has minimum deformation. The load cell and Gina gasket are bolted to this part.
6. **Moving Lining.** This steel plate is powered by a jack, with the top and bottom parts layered with Teflon sheets. Hence, this model lining is mobile and is able to simulate the motion of the tunnel lining.
7. **Actuator.** The actuator is used to mobilize the active lining and apply a controlled deformation to the joint gap.

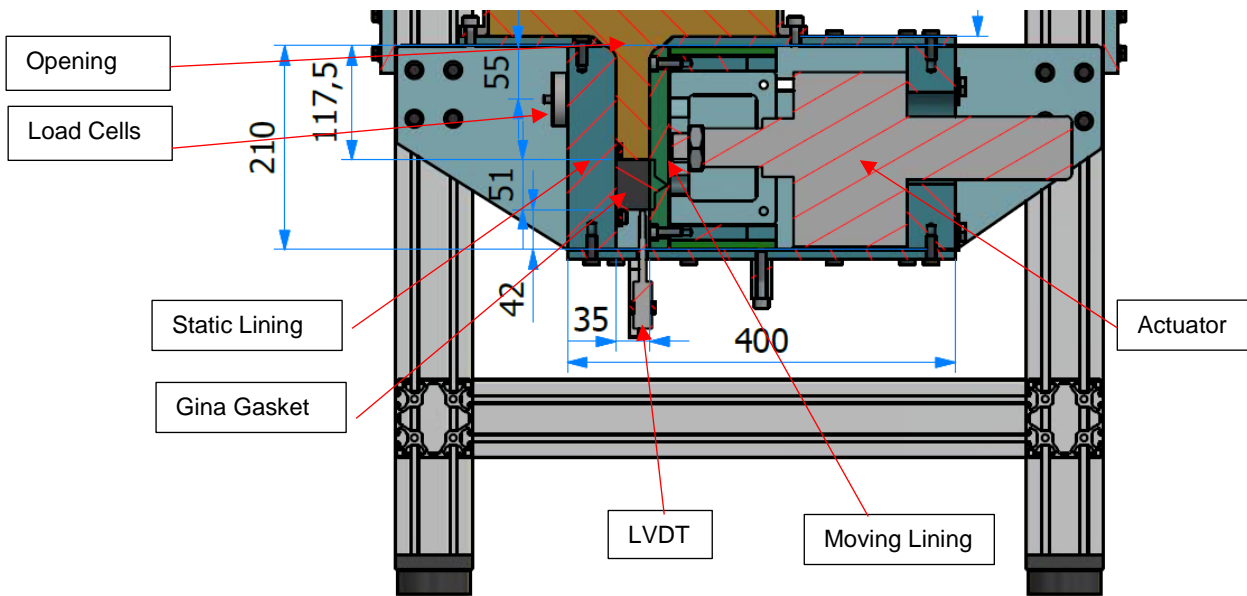


Figure 3-4 Joint Gap Detail (A Side)

Figure 3-5 shows a cross-section of the equipment from another perspective. The details are as follows:

1. **Pocket Penetrometer.** This measuring device is used to determine the cone resistance of the soil inside the model joint gap
2. **Flap.** A metal flap is attached to the side of the model wall, which remains closed throughout the experiment. The opening behind the flap matches the diameter of the penetrometer cone, thus sealing the sand inside when the flap is opened.

From this angle, several other instruments are shown. The pocket penetrometer, shown on the right-hand side of the figure, is attached to the side of the joint gap. The penetrometer rests on a frame that both maintains its position and provides reaction force upon its insertion into the joint gap.

From this side, it is shown that the joint gap model takes up almost the entire length of the soil drum diameter, at 280 mm. The large difference between the joint gap width and length implies that boundary effects have minimum influence on the middle section of the soil inside the joint gap.

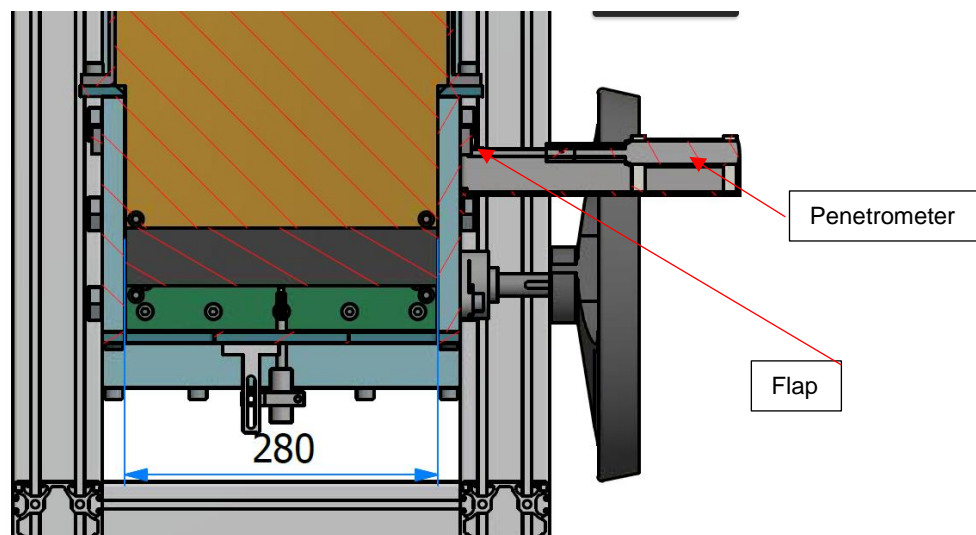


Figure 3-5 Joint Gap Detail (B-Side)

3.1.5. Model Gina Gasket

The model Gina gasket used in this experiment is also supplied by Trelleborg. The gasket is molded out of a similar type of material compared to the original gasket, albeit with much lower elastic modulus to compensate

for the strength limit of the actuator. The elastic modulus of the gasket is at 1.0 MPa, compared to the 2.2 MPa modulus for the Sh-50.

However, as the Gina gasket is made out of similar rubber material, the Poisson's ratio of the model gasket is comparable to the prototype at 0.498. The high Poisson's ratio implies that the gasket is nearly incompressible, and any axial compression is translated into lateral extension. The 2D scheme of the Gina gasket cross-section is shown in Figure 3-6.

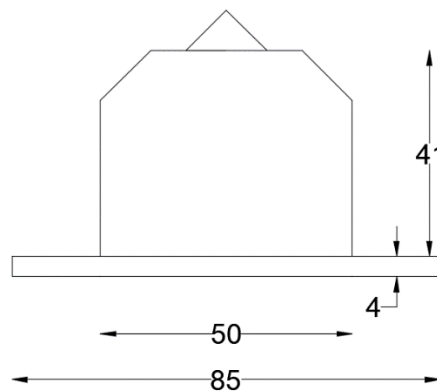


Figure 3-6 2D Scheme of the Gina Gasket

3.1.6. Actuator Force

Detailed calculation of the actuator force is stated in Appendix F. To summarize, the worst case scenario of the Rankine method, with a fully densified sand up to 45° internal friction angle yields 3.4 tons of force. Under special circumstances where the minor stress increases, elastic model calculations yield 4.2 tons as the maximum force. A summary of the calculated forces is shown in Table 3-1

Therefore the actuator strength chosen for this experiment is **5 tons**. The chosen actuator is a manual screw jack from Madler with a maximum jacking strength of 50 kN.

Table 3-1 Summary of Calculated Actuator Forces

No.	Condition	Max Soil Pressure	FoS	Max Soil Pressure after FoS	Max Soil Force	Max Force	Desc.
		kPa		kPa	kN	kN	
1	Rankine - Normal Density	204	2	408	14.28	25.866	-
2	Rankine - Fully Densified	397	1.5	595.5	20.807	33.699	-
3	Coulomb - Normal Density	416	2	832	29.07	43.7	-
4	Coulomb - Fully Densified	3134	1.5	4701	164.53	206.17	Omitted
5	Elastic (loose)	531	1.5	796.5	27.831	42.127	-
6	Elastic (dense)	1767	1.5	2650.5	97.77	120.05	Omitted

3.1.7. Instrumentation

As discussed previously in part 3.1.1, to answer the outlying research questions, measurement devices must be used. A detailed analysis of the research questions is discussed below.

Research Question 1

The focus of the first and main research question is the changes in the stress states of the soil. The hypothesis argues that due to external forces, the soil stresses change, mainly increasing along the tunnel lifetime. It is worth noting that the actual mechanism that causes the changes might be one reason or another, but the main focus of the research question still resides in the possibility that the phenomenon indeed occurs. To be able to quantify the changes in soil stress states, an instrument is required to measure the stresses. Therefore load cells are chosen to be used.

Secondary data is also considered, namely the deflection of the Gina profile. As the stress state increases, the Gina gasket is pushed further downwards to the inner side of the tunnel. Therefore to quantify the Gina deflections, an LVDT is chosen to be used

Research Sub Question 1

The first sub-question inquires whether densification occurs in the soil inside the joint gap throughout the lifetime of the tunnel. The most practical way to determine the density of soil is through the cone penetration test. Considering the small size of the test equipment, it would be impractical to insert an actual CPT cone inside the model joint gap. Therefore a pocket penetrometer is chosen as the method to acquire the cone resistance.

Research Sub Question 2

The last sub-question further requires the tests to be able to accurately quantify the stresses in the soil, as it would be compared to the stresses obtained in the finite element calculation. However, the load cell used to obtain data for the main research question would suffice to answer this sub-question.

3.1.7.1. Load Cell

The load cells used for this experiment is the Burster type 8523-100, shown in the scheme displayed in Figure 3-7. The 8523-100 variant has a diameter of 54.5 mm and height of 16 mm, with a maximum load capacity of 100 N.

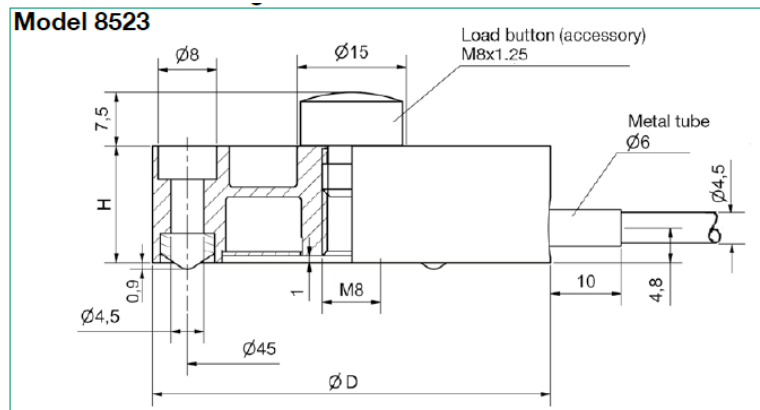


Figure 3-7 Burster Type 8523-100 2D Model

The load cell is bolted to the back side of the static lining plate while a screw connecting it with the loading plate placed through a hole inside. The loading plate is 1 cm in diameter and is mounted flush with the inner edge of the static lining.



Figure 3-8 Load Cell Used in the Model

The load cells measure the stresses of the soil inside the joint gap throughout the experiment. To accurately measure the stresses, the cells must be placed at a central point of the joint gap. The stresses measured by the load cell is the main data required for this research. Therefore it is considered to use multiple load cells, thus validating the measurement readings for each load cell. Two load cells spaced closely to the center of the immersion joint gap is chosen.

The calculation to determine the maximum load on the load cell is stated below. It was obtained that the maximum force for a 10 mm test plate is **32.04 N**, well below the maximum capacity of 100 N.

$$D_{lc} := 10\text{mm}$$

$$A_{lc} := \pi \cdot \frac{D_{lc}^2}{4} = 78.54\text{mm}^2$$

$$\sigma_{\text{hsoil}} = 204\text{ kPa} \quad F_o S_{lc} := 2$$

$$F_{lc} := F_o S_{lc} \cdot \sigma_{\text{hsoil}} \cdot A_{lc} = 32.044\text{N}$$

3.1.7.2. Linear Variable Displacement Transducer

The LVDT used in the experiment is ELE 10 mm transducer. The sensor is 120 mm in total length, with a 50 mm long base. The diameter of the base is 20 mm, and the needle itself is 10 mm.

The actual transducer used in the equipment is displayed in the picture shown in Figure 3-9. The instrument came equipped with a steel mounting bracket, also shown in Figure 3-9. The clamp holds it in place at the right angle to the deflection of the Gina profile.



Figure 3-9 LVDT and Clamp System

The LVDT is placed underneath the model joint gap and fastened to an adjustable frame. The location of LVDT is shown in Figure 3-10.

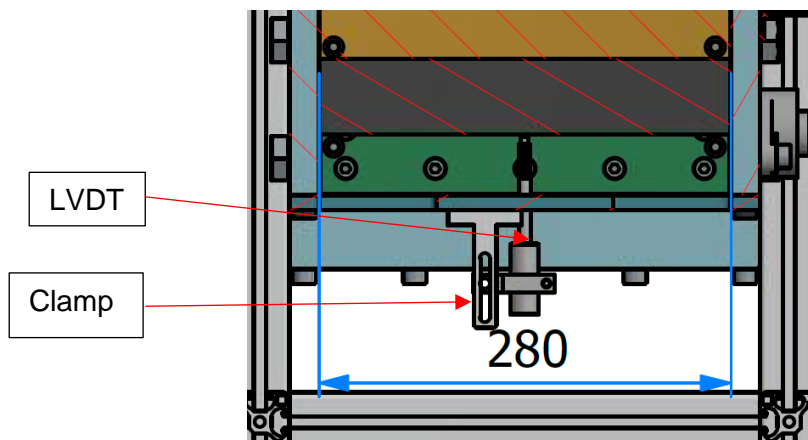


Figure 3-10 2D Scheme of LVDT Placement

3.1.7.3. Pocket Penetrometer

The pocket penetrometer used in the test equipment is the Eijkelkamp model M1.06.03.E. The penetrometer is 17-18 cm in total length, with a 10 cm handle. The penetrometer is spring loaded, with a spring constant of 2.142 kg/cm. The maximum capacity of the instrument is 0.5 MPa with an error of up to 0.0125 MPa. The penetrometer is suitable for up to 0.25" (6.25 mm) of testing depth. The detailed drawing of the penetrometer is shown in the scheme displayed in Figure 3-11.



Figure 3-11 Pocket Penetrometer 2D Scheme

The actual penetrometer used in the test equipment is shown in the picture in Figure 3-12. Due to the shallow testing depth of the instrument compared to the length of the joint gap, the penetrometer is modified to include a longer testing needle. The extra probe length enables the instrument to measure for up to 7 cm into the joint gap. The extended cone might register friction resistance, but this is considered too small and not corrected for.



Figure 3-12 Modified Pocket Penetrometer

At the edge point of insertion, a hole is made at the side of the joint gap model wall at the size of the penetrometer probe. To keep the sand inside the joint gap to leak outwards, a metal flap, with an opening size similar to the probe diameter, is installed right next to the hole. During the cyclic loading process, the flap remains closed, thus sealing the sand inside. Just before the penetrometer measurement begins, the flap is opened, allowing the penetrometer needle to be inserted.

3.2. General Experiment Procedure

In order to maintain consistency of the results for every individual test, standards in testing must be defined in the form of standardized procedures. The experiment procedure is divided into 2 succeeding stages, namely set up and testing. The steps in the lab procedure are discussed in the following subchapters.

As a general rule, every test is performed at least 3 times to be able to obtain valid results.

3.2.1. Setup Procedure

The calibration stage consists of the steps required to prepare the equipment for testing. The steps in the calibration procedure are as follows:

Equipment Reset

- i. The equipment is in a flipped position and resting on the top side of the soil drum. The tire inside the drum is unpressurized.
- ii. Lift the equipment to suspend it in midair. Rattle the equipment slightly to ensure most of the sand exits the joint gap.
- iii. Ensure that the joint gap is at 35 mm width

- iv. The equipment is subsequently gently flipped the right side up and lowered to the ground
- v. Air pressure is subsequently pumped into the tire to the desired magnitude of overpressure

3.2.2. Experiment Procedure

Prior to Experiment

The initial conditions of the test must first be recorded to be taken as reference.

- i. Start recording the load cell and LVDT readings
- ii. Perform pocket penetrometer test
 - a) Ensure that equipment is right side up and the load cell readings are stable which indicates that the sand is stable
 - b) Reset the penetrometer reading band to zero
 - c) Clamp penetrometer to the slider
 - d) Open the flap, slowly slide penetrometer probe in
 - e) Slide penetrometer probe out
 - f) Quickly close the flap

During Experiment

- i. Begin the series of loading-unloading cycle
 - a. Crank the worm gear half range outwards before starting time measurement
 - b. Crank the worm gear full range forwards, and subsequently full range backward for one full cycle
 - c. Repeat for as many cycles as needed.
- ii. Periodically check load cell reading every 5 cycles
- iii. Stop time measurement after all cycles are completed.

Post Experiment

- i. Stop recording the reading of the load cell and LVDT
- ii. Perform pocket penetrometer test
 - a. Ensure that equipment is right side up and the load cell readings are stable which indicates that the sand is stable
 - b. Reset the penetrometer reading band to zero
 - c. Clamp penetrometer to the slider
 - d. Open the flap, slowly slide penetrometer probe in
 - e. Slide penetrometer probe out
 - f. Quickly close the flap

3.2.3. Control Tests

Before any experiment could be performed, the equipment, along with its instruments, must first be tested. Multiple tests are designed to evaluate the consistency of the setup, and the reliability of the measurement readings.

3.2.3.1. Zero Cycle Test

The first control test involves taking readings from all of the measurement instruments without moving the actuators and altering the joint gap width. The primary intention of this test is to measure the consistency of the properties of the test sand. Therefore the pocket penetrometer test is the main focus of this configuration, due to its ability to determine the sand density.

Before every test is performed, the soil inside the joint gap must be reset to obtain a looser density. The equipment is reset by rotating it upside down and subsequently rotating it right side up, giving a looser sand profile inside the joint gap. However, the density of the newly loosened sand might not be consistent with every rotation. Therefore this control test must be performed to have an idea of the behavior of the sand after every resetting procedure.

The test scheme consists of basically performing the setup procedure without proceeding to the cyclic loading stage. After every equipment reset the following measurements are taken:

- Pocket penetrometer test
- Soil pressure reading from the load cell

3.2.3.2. Stepwise Penetrometer Test

The next control test determines the effect of penetrometer tests to the soil sample inside the model joint gap. During each penetrometer measurement, the probe is inserted into the soil to a depth of 7 cm. This action might disturb the soil inside the joint gap and provide false readings to the density and the stresses of the soil. However the exact significance of the effect is still undetermined. Thus this type of control test is designed.

The stepwise penetrometer test involves performing subsequent experiments with a varying number of cycles. The results of the penetrometer tests are compared with one another, and subsequently with the normal experiments. The expected result of this test is the consistency in densification pattern. In the case that the measurements show a clear pattern of sand densification, it would be safe to assume that the pocket penetrometer tests do not have many detrimental effects on the soil inside the joint gap.

3.2.3.3. Sand-less Test

The underlying principle of the hypothesis used in this experiment revolves around the fact that the Gina gasket deforms in one direction only. The sand in above the Gina gasket is assumed to have a densified enough to a state that the gasket is unable to deform outwards any longer. Due to the nature of rubber incompressibility, it is assumed that most of the outwards deflection are entirely transformed into inwards deflection.

Obtaining the knowledge of the actual effects of the soil to the deflection of the Gina gasket is crucial to proving the hypothesis. Therefore it was decided that a control compression test for the Gina gasket, where the sand is not present, would be performed. The sand-less test would give measurable deflections of the Gina in its unconfined state, hence having less deflection inwards in theory.

3.3. Test Configurations

The main premise of the test would be a scaled replica of the roof/top part of the joint gap, considering the fact that it would be unsafe for the equipment if it were to be tilted sideways. Hence the soil is loaded with its own self-weight to be able to enter the joint gap. This condition makes it inappropriate to conduct tests for the joint gap wall on this equipment, and the results might be inaccurate.

3.3.1. Reference Configuration

The first configuration to be tested is designated as the main configuration, in which all the variables that are used in it are normal/average values and would most likely happen in most parts of the tunnel. This configuration would subsequently be used as a reference to any other configurations that follow. The variables of the main configuration are as follows:

3.3.1.1. Overpressure of 0.58 bar

The magnitude of overpressure takes into account the minimum thickness of the soil cover on top of immersed tunnels when it is situated underneath a river or canal. As the minimum soil cover is 4 meters, the soil pressure is as follows:

$$\begin{aligned}\sigma_v &= \gamma * H \\ \sigma_v &= 17 \frac{\text{kN}}{\text{m}^3} * 4 \text{ m} \\ \sigma_v &= 68 \text{ kPa}\end{aligned}$$

As the soil pressure inside the drum is expected to be 10.2 kPa, the required overpressure becomes:

$$\sigma_{air} = 68 \text{ kPa} - 10.2 \text{ kPa} = 57.8 \text{ kPa}$$

Therefore the tire inside the drum would have an added 0.58 bar of air pressure pumped into it.

3.3.1.2. Stroke length of 1.5 mm

The expansion and contraction of the joint gaps depend on the tunnel materials and length of each element. In average, the original tunnel contracts and expands at a maximum range of 10 mm throughout the years. Therefore the scaled model would have it at one-third of the original deformation range, which calculates to be 3.5 mm. However as the capacity of the screw jack is limited, the stroke length will be reduced to 1.5 mm.

3.3.1.3. Up to 50 Loading and Unloading Cycles

It was decided that the main configuration would include 50 cycles of loading and unloading to simulate the past 50-year period of contraction and expansion of the joint gap. Considering the strength of the screw jack, and possible further densification of the soil, the reference configuration will be tested for 25 cycles. The number of cycles will be increased to 50 if circumstances allow.

3.3.2. Variations in the Configuration

3.3.2.1. Variations in Stroke Length

The size and exact material properties of the tunnel element might vary in real life. The variation might affect the range of which the joint gap expands and contracts. Therefore several varieties of lining stroke length would be tested to correlate the effects on the densification. The variations are as follows:

- a. Stroke length of 0.5 mm
- b. Stroke length of 1.0 mm
- c. Stroke length of 2.5 mm

3.3.2.2. Variations in Number of Cycles

The Gina profile in the Rotterdam Metrotunnel had failed after approximately 50 years of annual loading and unloading cycles. However, it is still undetermined whether or not the densification process occurs throughout the years or if it peaks at a certain amount of time. It is also unclear if the soil would densify further given more time. Therefore it is proposed that the experiment would include configurations in which the number of strokes in a single test is varied. The expected outcome would be a trend in the increase of soil stresses against years of exposure to seasonal changes in temperature (number of strokes).

The suggested test configuration would be an incrementally increasing number of load cycles in order to compare the results with the reference configuration. The number of strokes is as follows:

- a. 10 Cycles
- b. 20 Cycles
- c. 25 Cycles

The results of the experiments would subsequently be analyzed. In the case that the results show no peak in soil stresses, the configuration would change to simulate extended periods of time in which the cycle of loading and unloading continues. The final configuration regarding the number of strokes would be:

- d. 75 cycles.

3.3.3. Summary of Configurations & Test Conditions

To ease the referencing of every configuration in the report, each configuration was assigned a code pertaining to its test conditions. A summary of the various test configurations is shown in Table 3-2. As discussed before; each configuration will be tested 3 times to ensure data consistency. The suffix "XX" in

every test code signals the trial number of the test. The suffix “YY” in the sandless test signals the test configuration stroke length which it is a control of.

Table 3-2 Summary of Test Configurations

Test	Test Code	Test Conditions						
		Overburden			Stroke Length		Number of Cycles	
		Depth (m)	Overburden (kPa)	Tire Pressure (kPa)	Tunnel Deflection (mm)	Stroke Length (mm)		
Part 1 - Calibration Tests								
1.1	Zero Cycle	TC1-XX	4	68	57.8	0	0	0
1.2	Stepwise Penetrometer	TC2-XX	4	68	57.8	10	3.5	
Part 2 - Main tests								
2.1	Reference	TVS15-XX	4	68	57.8	4.5	3.5	25
2.2	Variables							
2.2.1	Stroke 0.5 mm	TVS05-XX	4	68	57.8	1.5	0.5	75
2.2.2	Stroke 1.0 mm	TVS10-XX	4	68	57.8	3	1	50
2.2.3	Stroke 2.5 mm	TVS25-XX	4	68	57.8	7.5	2.5	20
2.2.4	Stroke 3.5 mm	TVS35-XX	4	68	57.8	10.5	3.5	10
Part 3 - Post-Calibration Tests								
3.1	Sand-less Test	TC3-YY-XX	0	0	0	10	Varies	25

3.3.4. Extra Configurations

The following test configurations are only taken into account given the capabilities and practicality of the equipment, and enough spare time after the aforementioned configurations have been performed.

3.3.4.1. Daily Changes in Temperature

The hypothesis states that the yearly changes in temperature are the main reason behind the densification of the soil inside the gap. However one must not rule out the possibility that the daily changes in temperature might also influence the soil behavior. Therefore it was suggested that the experiment would include a simulation of changing daily temperatures

Daily changes in temperature are relatively more subtle albeit much more frequent than the seasonal temperature changes. Therefore the model would have to accommodate for a large number of cycles with a much smaller stroke length. The feasibility of this configuration would very much depend on the capabilities of the equipment.

3.3.4.2. Variations in Stroke Rate

As stated before, the cycle period is mainly governed by the practicality aspects of the equipment. Furthermore, long-term behavior of dry, unsaturated sand usually does not change much from the short-term behavior. However, the experiment is performed under a concise time range compared to the original tunnel. Therefore, there might be some difference of soil behavior between the model and the tunnel itself. Therefore variations in stroke rate are considered.

3.4. Experiment Timeline

Taking into account the time estimates of each test variant from part 3.3, a test plan of the entire experiment is constructed. The first factor to consider is that each test configuration is required to be performed at least 3 times. Taking into consideration that each individual test ranges around 90 minutes to perform, it is safe to assume that each set of 3 tests in a single configuration could be performed in a single day with spare time for another test in case of failure.

In conclusion, the entire experiment is estimated to take 10 working days, with 5 working days as spare time. The illustration of the test plan is shown in Table 3-3.

Chapter 4 Laboratory Test Result Analysis

4.1. Test Results

4.1.1. Overview

In total, 25 test configurations were performed, of which only two results were invalid. Test TVS10-01 was overloaded at cycle 35. Therefore the experiment was terminated at cycle 39, and only the results up until cycle 35 were taken into account. Configuration TC2-50-01 consists of 7 separate tests with a varying number of cycles. Table 4-1 shows the complete list of conducted tests.

Table 4-1 Performed Tests

No	Test Code	Test Date	Stroke Length (mm)	Strain (%)	Loading Cycles	Readings			Status	Notes
						D	P	LC		
1	TVS05-01	7/11/2017	0.5	1.43	56	<input checked="" type="checkbox"/>	<input checked="" type="checkbox"/>			
2	TVS05-02	7/13/2017	0.5	1.43	77	<input checked="" type="checkbox"/>	<input checked="" type="checkbox"/>			
3	TVS05-03	7/13/2017	0.5	1.43	77	<input checked="" type="checkbox"/>	<input checked="" type="checkbox"/>			
4	TVS05-04	7/19/2017	0.5	1.43	74	<input checked="" type="checkbox"/>	<input checked="" type="checkbox"/>	<input checked="" type="checkbox"/>		
5	TVS05-05	7/31/2017	0.5	1.43	77	<input checked="" type="checkbox"/>	<input checked="" type="checkbox"/>	<input checked="" type="checkbox"/>		
6	TVS10-01	7/11/2017	1	2.86	39	<input checked="" type="checkbox"/>	<input checked="" type="checkbox"/>		Heavy overloading at cycle 35	
7	TVS10-02	7/11/2017	1	2.86	53	<input checked="" type="checkbox"/>	<input checked="" type="checkbox"/>			
8	TVS10-03	7/13/2017	1	2.86	52	<input checked="" type="checkbox"/>	<input checked="" type="checkbox"/>			
9	TVS10-04	7/19/2017	1	2.86	54	<input checked="" type="checkbox"/>	<input checked="" type="checkbox"/>			
10	TVS10-05	7/31/2017	1	2.86	47	<input checked="" type="checkbox"/>	<input checked="" type="checkbox"/>	<input checked="" type="checkbox"/>		
11	TVS10-06	8/1/2017	1	2.86	53	<input checked="" type="checkbox"/>	<input checked="" type="checkbox"/>	<input checked="" type="checkbox"/>		
12	TVS15-01	7/7/2017	1.5	4.29	5	<input checked="" type="checkbox"/>			Target cycle not reached	
13	TVS15-02	7/10/2017	1.5	4.29	20	<input checked="" type="checkbox"/>			Inconsistent loading	
14	TVS15-03	7/10/2017	1.5	4.29	22	<input checked="" type="checkbox"/>			Penetrometer test not taken	
15	TVS15-04	7/10/2017	1.5	4.29	20	<input checked="" type="checkbox"/>	<input checked="" type="checkbox"/>			
16	TVS15-05	7/11/2017	1.5	4.29	21	<input checked="" type="checkbox"/>	<input checked="" type="checkbox"/>			
17	TVS15-06	7/11/2017	1.5	4.29	26	<input checked="" type="checkbox"/>	<input checked="" type="checkbox"/>	<input checked="" type="checkbox"/>		
18	TVS15-07	8/1/2017	1.5	4.29	25	<input checked="" type="checkbox"/>	<input checked="" type="checkbox"/>	<input checked="" type="checkbox"/>		
19	TVS15-08	8/1/2017	1.5	4.29	25	<input checked="" type="checkbox"/>	<input checked="" type="checkbox"/>			
20	TVS25-01	7/19/2017	2.5	7.14	7	<input checked="" type="checkbox"/>	<input checked="" type="checkbox"/>			
21	TVS25-02	8/2/2017	2.5	7.14	7	<input checked="" type="checkbox"/>	<input checked="" type="checkbox"/>	<input checked="" type="checkbox"/>		
22	TC2-50-01	Various	1	2.86	Various	<input checked="" type="checkbox"/>	<input checked="" type="checkbox"/>			
23	TC3-05-01	7/17/2017	0.5	1.43	25	<input checked="" type="checkbox"/>				
24	TC3-10-01	7/17/2017	1	2.86	26	<input checked="" type="checkbox"/>				
25	TC3-15-15	7/17/2017	1.5	4.29	23	<input checked="" type="checkbox"/>				

	Success		Failed		Success with exceptions
--	---------	--	--------	--	-------------------------

	D = Displacement measurements
	P = Penetrometer measurements
	LC = Load cell measurements

4.1.2. Stresses

Typical Test Results

Figure 4-1 shows the soil stresses for test TVS15-08, which applies 1.5 mm stroke length. Two load cells were used for every experiment, noted by LC1 and LC2 in the graph. Both values are subsequently averaged, and the resulting peak points plotted. The peak points are compared with experiment results at varying stroke lengths.

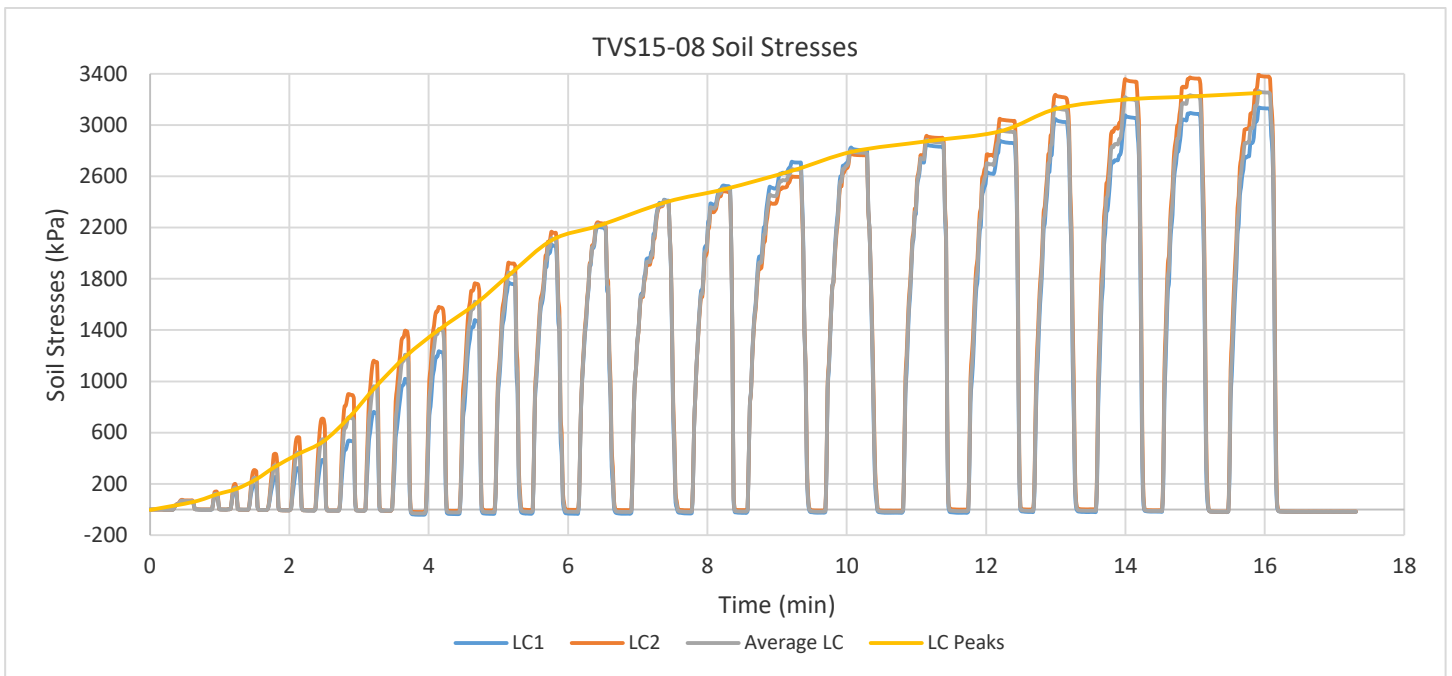


Figure 4-1 TVS15-08 Soil Stresses Results

4.1.3. Gasket Bottom Side Deflections

Typical Test Results

Figure 4-2 shows the graph for test configuration TVS15-05, which is the variation in which 1.5 mm stroke length was used. The graph plots the deflection of the Gina gasket against time, which is shown by the blue line. The orange and gray lines indicate the peak deflections and rebound points of the Gina gasket respectively. It is shown that even though the system is loaded with the same stroke length every cycle, the Gina gasket seems to deflect downwards continually.

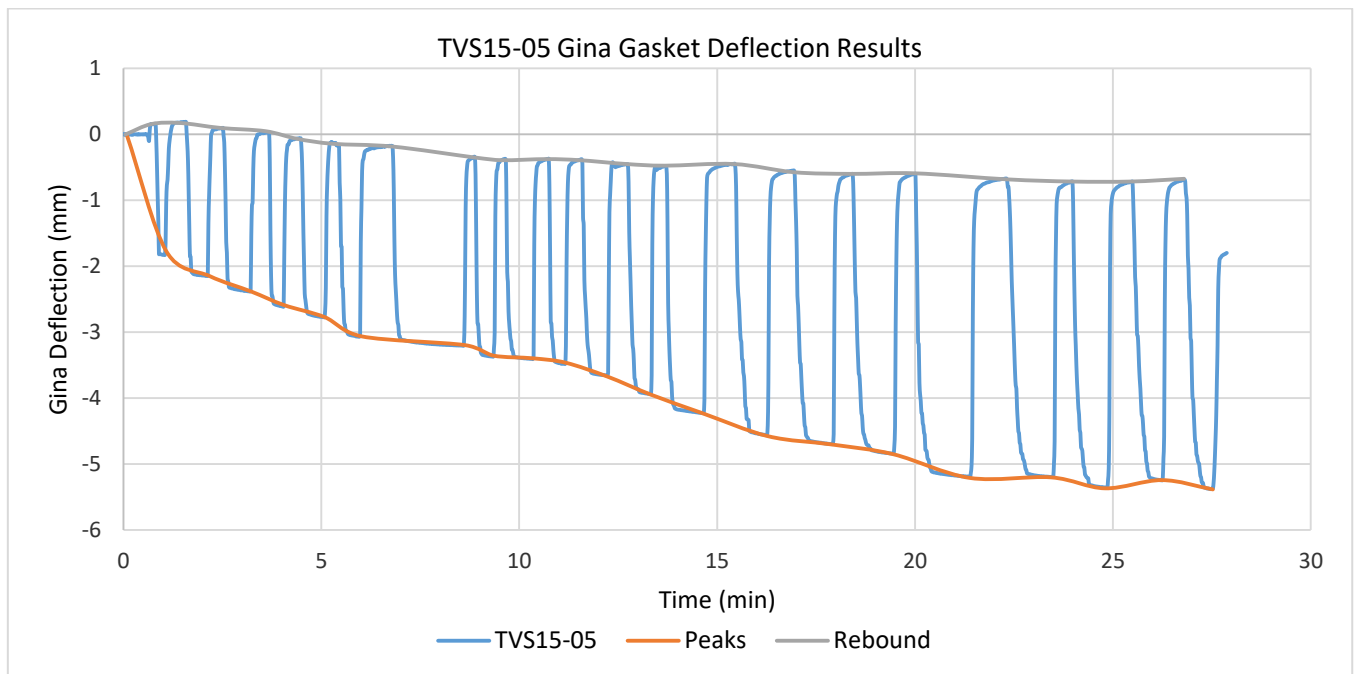


Figure 4-2 Gina Gasket Deflection Results for TVS15-05

Sand-less Tests

Figure 4-3 shows the graph for the sand less control test TC3-15-01, which has the same stroke length as the test results displayed in Figure 4-2. It can be observed that without the influence of the sand, both the gasket deflection peak and rebound points remains relatively constant throughout the test despite initial

overloading and stroke inaccuracies. Comparing the gasket deflection values of both graphs shows that the sand has a significant effect on the overall gasket deflection.

Figure 4-4 compares 3 different stroke lengths for the sand-less control test. It can be observed that although the gasket deflections are more significant at higher stroke lengths, the resulting deflection differs only in the order of 0.1 mm. Hence the deflection is significantly lower compared to the tests performed with sand shown in Figure 4-2.

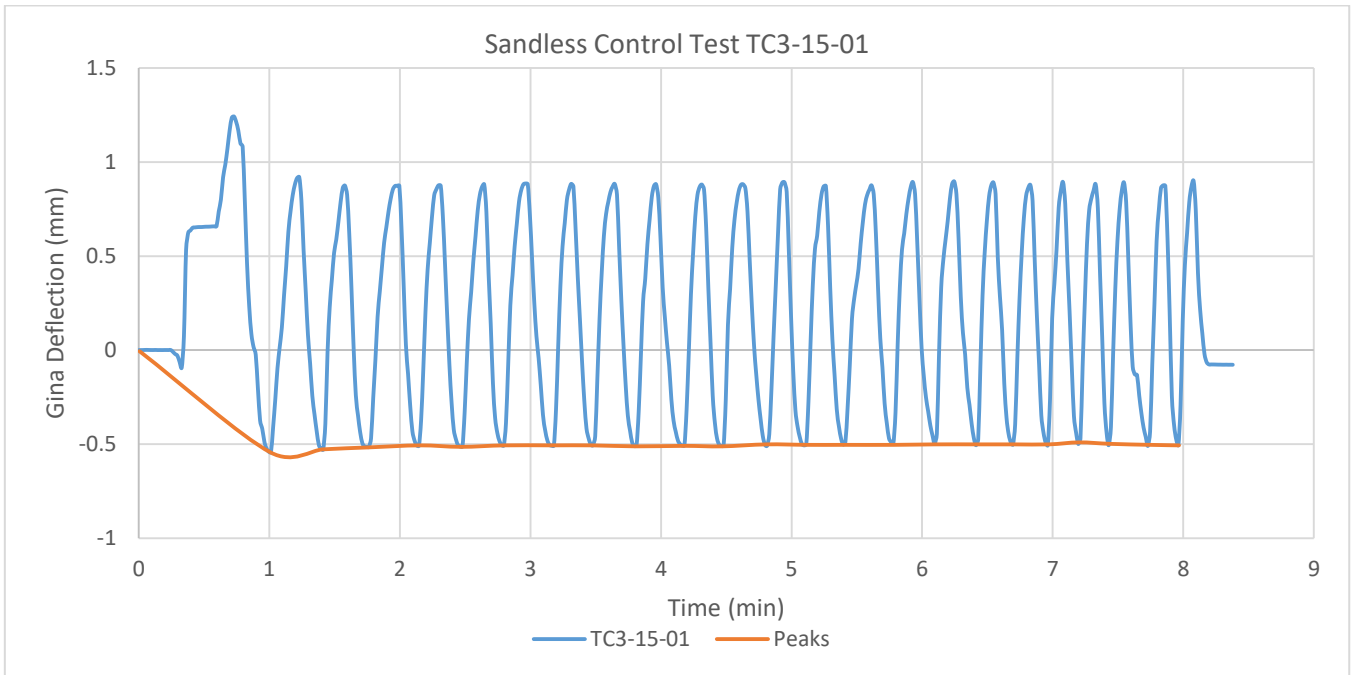


Figure 4-3 Gina Gasket Deflection Results for Control Test TC3-15-01

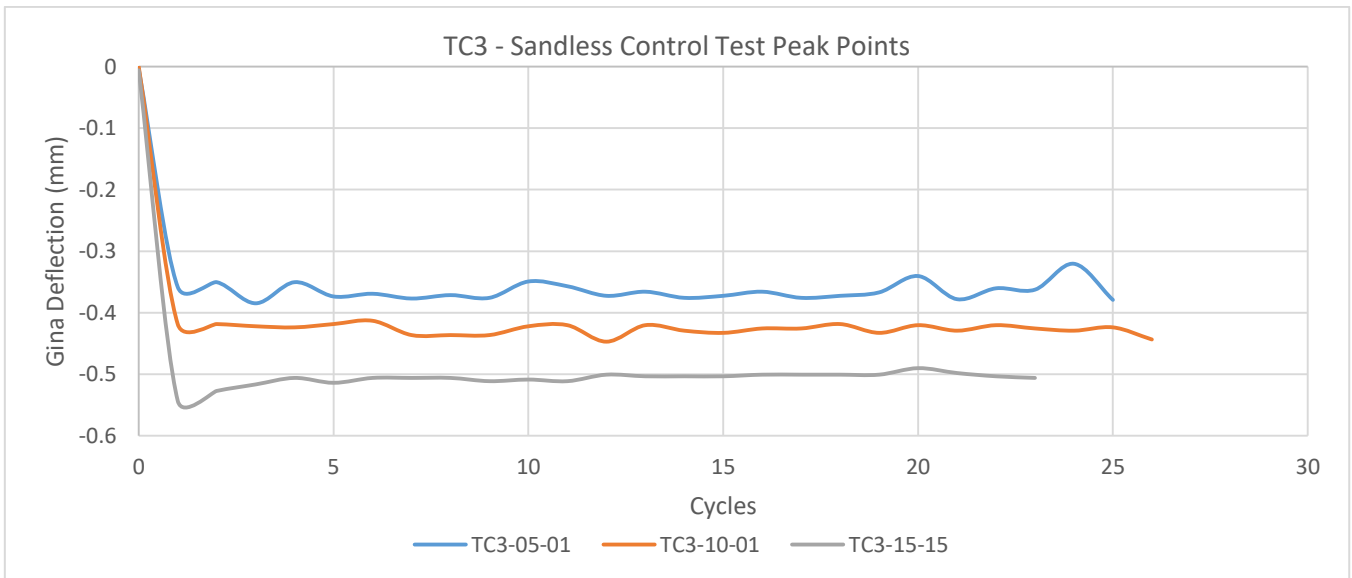


Figure 4-4 TC3 Peak Points

4.1.4. Penetrometer Test

The penetrometer test results from multiple tests are shown in Table 4-2. The 2 available flaps in the device, namely the “wheel side flap” and the “far side flap”, are used to measure 2 different penetrometer tests in order to have reliable test results for every experiment. During preparation of tests TVS05-01 to TVS05-03, the test device spent too much time sideways, hence the over-densification of the far side flap compared to the wheel side flap.

Table 4-2 Pocket Penetrometer Test Results

Location		qc (MPa)									
		TVS05-01	TVS05-02	TVS05-03	TVS05-04	TVS05-05	TVS10-01	TVS10-02	TVS10-03	TVS10-04	TVS10-05
Wheel Side	Start	0.015	0.015	0.02	0.01	0.01	0.015	0.02	0.02	0.015	0.01
	End	0.175	0.13	0.175	0.185	0.175	0.13	0.2	0.16	0.175	0.19
Far Side	Start	0.06	0.05	0.06	0.01	0.01	0.02	0.02	0.06	0.025	0.01
	End	0.42	0.25	0.3	2.25	0.16	0.13	0.19	0.16	0.17	0.19
Average	Start	0.0375	0.0325	0.04	0.01	0.01	0.0175	0.02	0.04	0.02	0.01
	End	0.2975	0.19	0.2375	1.2175	0.1675	0.13	0.195	0.16	0.1725	0.19
Cycles		56	77	77	74	77	39	53	52	54	47
Location		TVS10-06	TVS15-03	TVS15-04	TVS15-05	TVS15-06	TVS15-07	TVS15-08	TVS25-01	TVS25-02	
Wheel Side	Start	0.01	-	0.03	0.02	0.015	0.01	0.01	0.015	0.01	
	End	0.2	-	0.29	0.22	0.11	0.12	0.09	0.1	0.09	
Far Side	Start	0.01	-	0.03	0.02	0.02	0.01	0.01	0.02	0.01	
	End	0.175	-	0.3	0.24	0.125	0.1	0.08	0.12	0.08	
Average	Start	0.01	-	0.03	0.02	0.0175	0.01	0.01	0.0175	0.01	
	End	0.1875	-	0.295	0.23	0.1175	0.11	0.085	0.11	0.085	
Cycles		53	22	20	21	26	25	25	6	7	

Table 4-3 shows the results of the stepwise penetrometer control test. It can be observed that the cone resistance steadily increases with every increasing cycle. It is shown that during the first 30 cycles, the density increases more rapidly compared to the following loading cycles.

Multiple tests were performed for greater cycles due to inconsistencies in the readings. The first set of tests, (TC2-40-01 and TC2-50-01) give fluctuating readings that result in higher cone resistance for cycles 35 and 40 compared to cycles 45 and 50. The second set of tests (TC2-40-02 and TC2-50-02) give predictable increasing density readings.

Table 4-3 TC2 Pocket Penetrometer Test Results

Location		qc (MPa)													
		TC2-10-01	TC2-10-01	TC2-20-01	TC2-20-01	TC2-30-01	TC2-30-01	TC2-40-01	TC2-40-01	TC2-40-02	TC2-40-02	TC2-50-01	TC2-50-01	TC2-50-02	TC2-50-02
Wheel Side	Start		0.02		0.02		0.02		0.02		0.01		0.02		0.02
	End		0.06		0.075		0.11		0.2		0.13		0.15		0.18
Far Side	Start	0.02		0.02		0.02		0.02		0.01		0.02		0.02	
	End	0.03		0.075		0.09		0.175		0.08		0.135		0.14	
Cycles		5	10	15	20	25	30	35	40	35	40	45	50	45	50

4.2. Analysis

4.2.1. Gina Gasket Deflection Analysis

Peak points of the gasket deflection graph from similar configurations were plotted on the same graph shown in Figure 4-5. It can be observed that the different peak point graphs form similar gradients albeit with different values. This indicates consistent soil behavior between the experiments of the same stroke length.

The peak points graph for every configuration generally has much more deflection than their respective control tests. Larger stroke lengths amount to more substantial Gina gasket deflections.

A general downward trend of the peak point suggests that the soil exerts incrementally increasing load on the gasket over each loading cycle. The increase in load may be translated to an increase in soil stresses, allowed by a densification mechanism of the joint gap soil. Similar results are observed in the TVS10 and TVS05 configuration tests, which utilizes 1.0 mm and 0.5 mm stroke lengths for every loading cycle respectively.

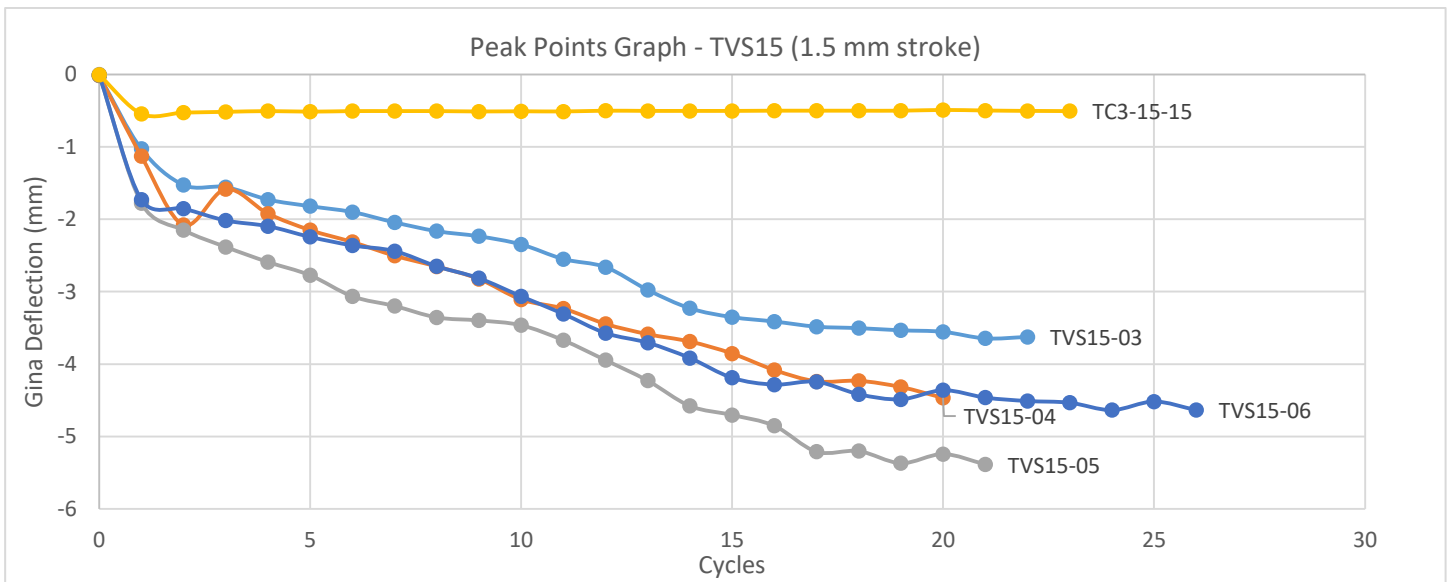


Figure 4-5 TVS15 Peak Points Graph

Figure 4-6 shows the peak point graphs for every configuration normalized with their respective stroke lengths. Experiment results with similar stroke lengths are plotted together in Figure 4-7.

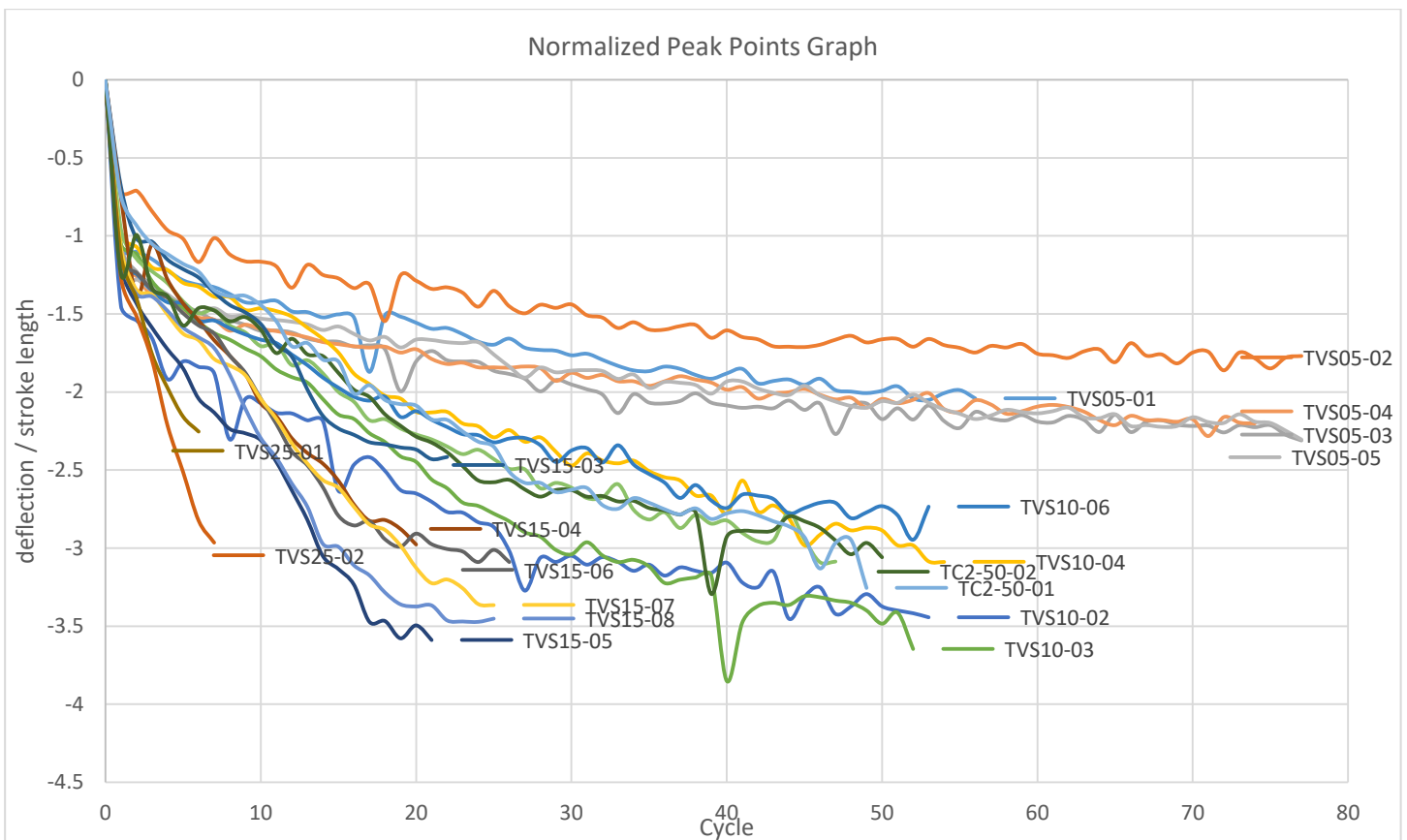


Figure 4-6 Normalized Peak Points Graph

It can be observed from Figure 4-7 that the deflection results between each test at its corresponding stroke length are similar to each other. This shows that the test results are valid and reliable, and signifies to the extent that the soil demonstrates similar behavior.

However observing different stroke lengths reveals that the curve gradient differs from each other. The curve becomes steeper as the stroke length increases. This suggests that the soil undergoes escalating plastic deformation which allows more soil to enter the joint gap, hence increasing the soil density and propagating the effect.

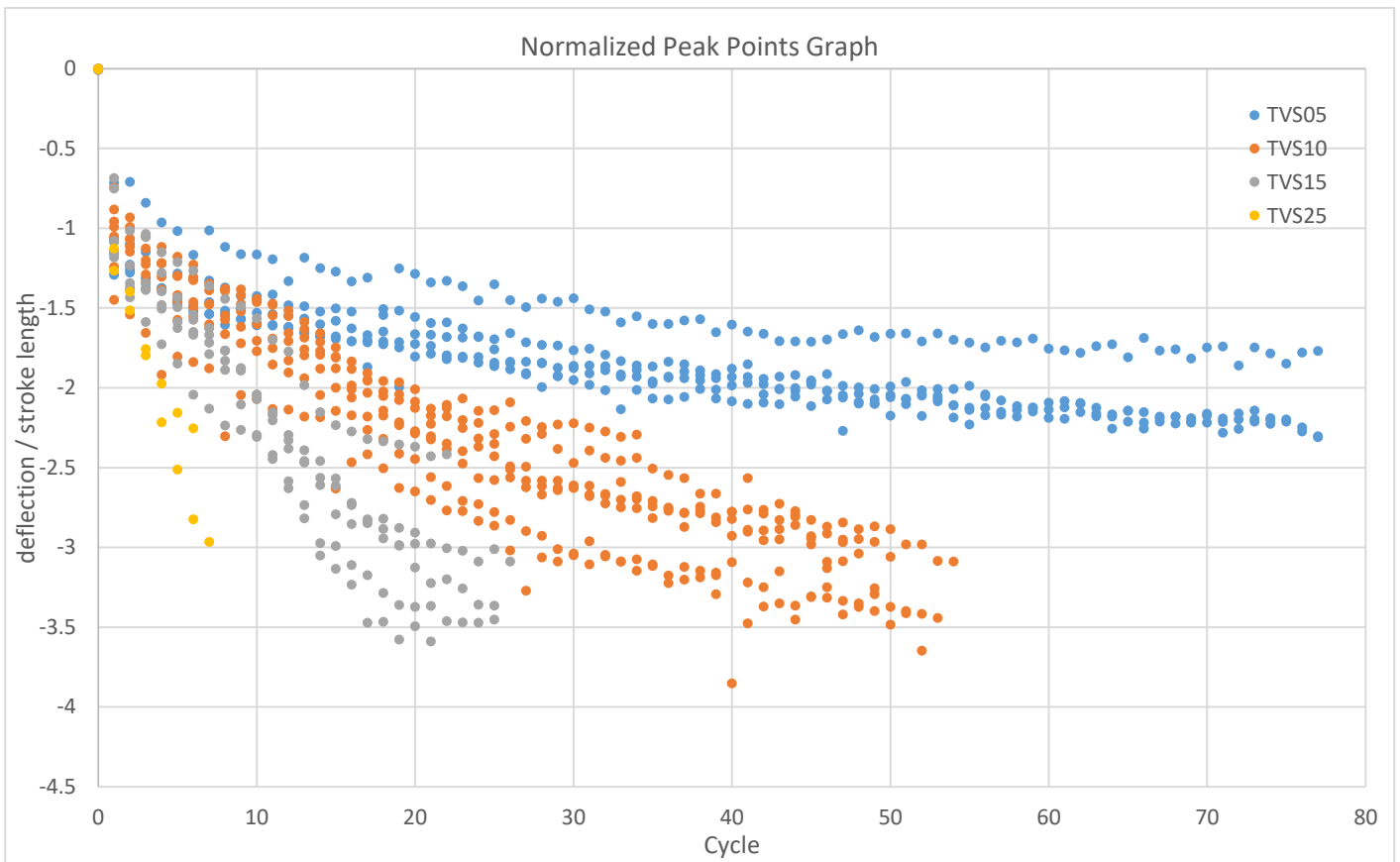


Figure 4-7 Normalized Peak Points Graph at Varying Stroke Lengths

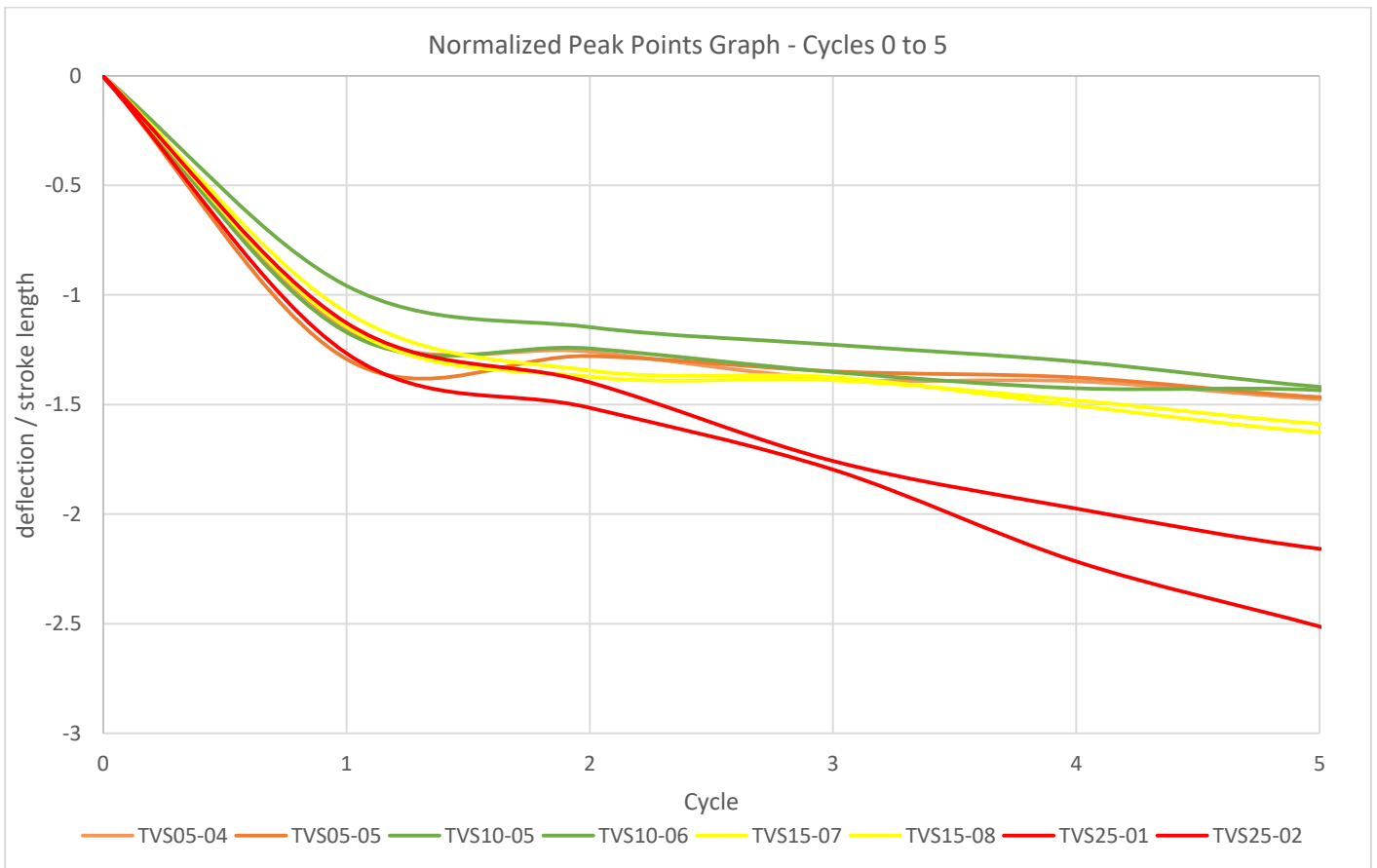


Figure 4-8 Normalized Peak Points Graph at Varying Stroke Lengths, Cycle 0 to Cycle 5

A detailed look at the first 5 cycles of the graph in Figure 4-7 is shown in Figure 4-8. The graph plots select results at varying stroke lengths, with similar stroke lengths denoted by the same color. Results of the first 5

cycles show that the initial normalized deflection of the Gina gasket is similar for every stroke length. Comparing these values with the gasket deflection at higher number of cycles reveals that the rate of increase in gasket deflection rises with increasing stroke lengths.

4.2.2. Soil Stress Analysis

Soil Stress over Time

Figure 4-9 shows the stress peak points for each experiment normalized with its corresponding stroke length over the number of cycles. Each test of the same stroke length produces similar values of stresses at comparable gradients, thus validating the experiment results.

However, the gradient varies between different stroke lengths. An increase in stroke length equates to a rise in the gradient, signifying a more rapid increase in stresses. Higher stroke lengths translate to higher strains, thus applying more compaction to the sand. This results in more void space in the sand and allows for more backfill sand to enter the joint gap. This, in turn, increases the sand stiffness more rapidly and results in a greater rate stress increase.

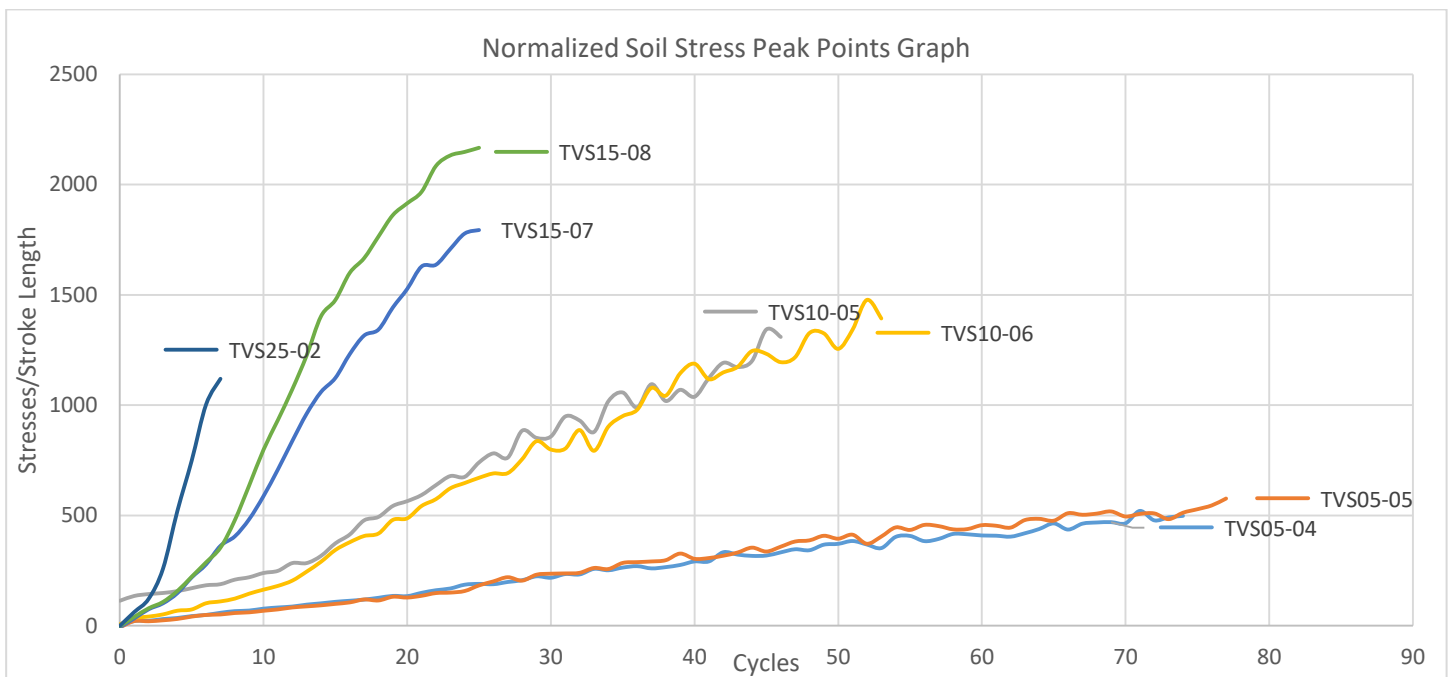


Figure 4-9 Normalized Soil Stress Peak Points Graph

Soil Stress vs. Gina Deflection

Figure 4-10 is a typical plot of the horizontal soil stress to its corresponding gasket deflection over the entire loading cycle. It can be observed that during the loading part of every cycle, the system follows a certain gradient. However, hysteretic behavior is present during unloading, where the stress relief is much more rapid compared to the rebound of the Gina gasket. The hysteretic behavior is more apparent at later cycles and at higher gasket deflections, with more noticeable lagging of gasket rebound compared to the stress decrease.

The hysteretic behavior indicates that loss of energy is present during a cycle. The energy loss is due to the sand retaining its shape during unloading. Thus void is formed during the process, allowing for the backfill sand to enter the joint gap.

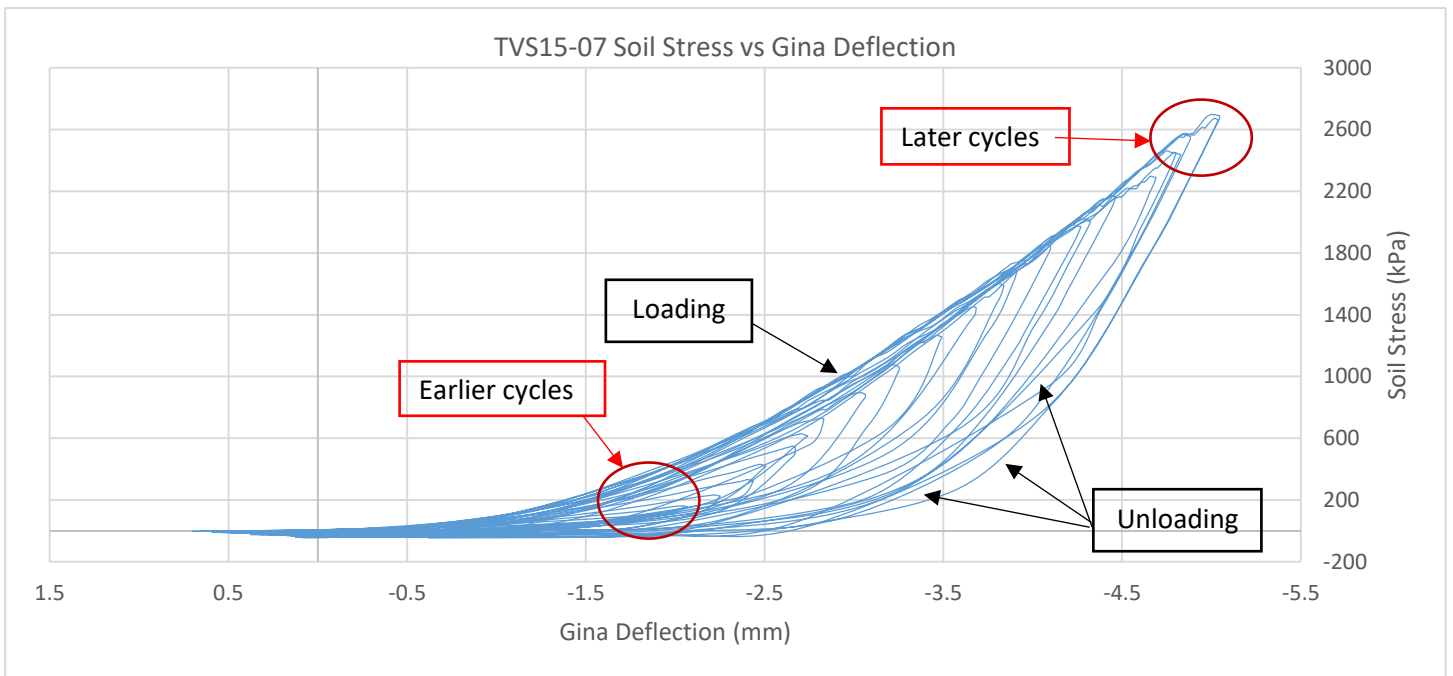


Figure 4-10 TVS15-07 Soil Stress vs. Gina Deflection

The graph is plotted along with two other configurations of varying stroke lengths and number of cycles in Figure 4-11. The data shown in Figure 4-11 are all of the data points from the experiment results, similar to Figure 4-10, albeit shown as marker points for better visualization.

All 3 sample configurations also show hysteretic behavior during unloading to a varying degree. The 3 data clusters form similar loading curves, with comparable gradients at later cycles.

The 2.5 mm stroke length configuration was not considered due to its low number of cycles.

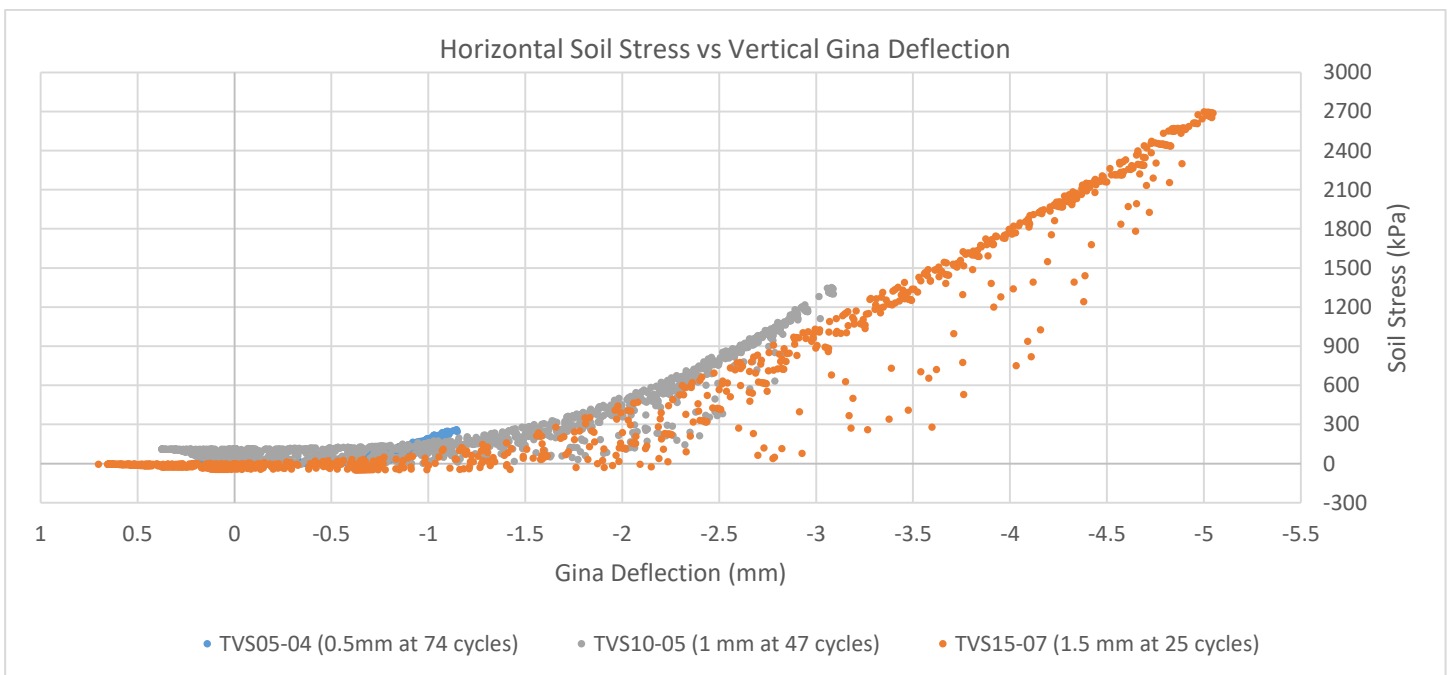


Figure 4-11 Stress vs. Gina Deflection at Varying Configurations

4.2.3. Stress Path Analysis

Due to limitations in the testing device, determining the stress path from the results requires several assumptions to be made.

1. The device is equipped with stress sensors in the main horizontal direction, which contains the press plate. However the secondary horizontal direction lacks any sensors at all, and the stresses are assumed to be identical with the former.
2. The stresses in the vertical direction are assumed to be maintained at the overburden stress level. Increase in vertical stresses from wall friction is not taken into account.

Figure 4-12 shows the stress path from configuration TVS05-05. As with the graphs discussed in 4.2.2, the stress path shows an apparent hysteretic behavior. During the loading process, the sand generally follows a linear line. However, during unloading, the stress path deviates from the loading path, rising in intensity after subsequent cycles. During unloading, the stress path rebounds as it passes the zero deflection point. The rebound is due to lowering of the principal stress to the point of principal axis rotation.

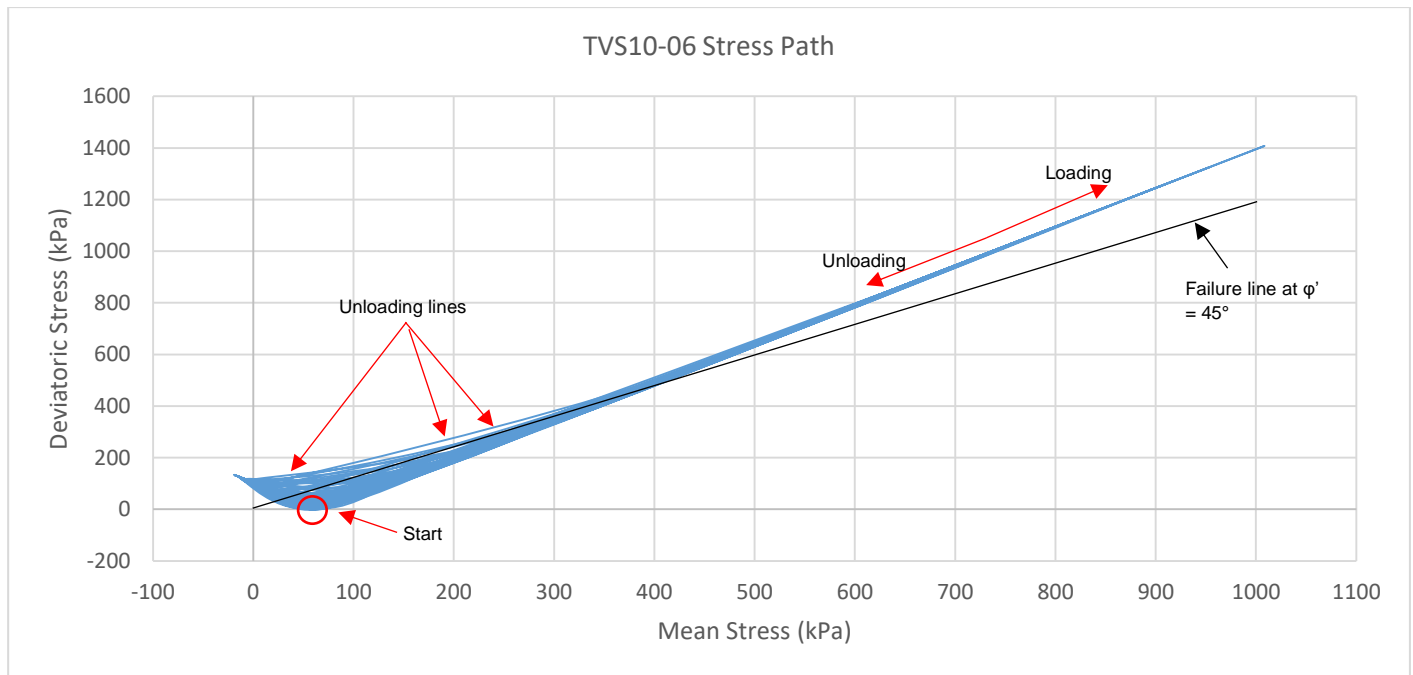


Figure 4-12 TVS10-06 Stress Path

4.2.4. Evolution of Soil Density

Figure 4-13 visualizes the penetrometer test results shown in Table 4-2. Results with similar stroke lengths were plotted with the same color, and a trend line is subsequently drawn through. Similar to the stress increase discussed in part 4.2.2, the trend line results also increase in gradient with increasing stroke lengths. This signifies a greater rate of densification at higher strains.

Conclusions taken from the penetrometer test results are as follows:

1. The highest values of the cone resistance at 2-3 MPa are indicative for values of sand categorized as medium-low to medium density. This suggests that the Gina gasket might fail even before the sand reaches full density.
2. Results of TVS05 and TVS10 in Figure 4-13 show that the cone resistance value continues to increase well after the 50th cycle.
3. At higher strains, the increase in cone resistance is more rapid

Figure 4-14 plots the TC2 test results shown in Table 4-2 as scatter data points with a trend line drawn through. The cone resistance steadily increases with time. As discussed in section 4.1.4, tests at 35 to 50 cycles are performed multiple times. The divergence might be due to several factors, namely:

1. Natural ground arches might form above the joint gap, as suggested previously in sections 2.2.4 and 2.2.5 which results in fewer sand particles entering the gap, thus less densification. Due to the nature of the equipment rotation, arches might fail to form, allowing more sand to enter and resulting in more densification
2. Some leakage of sand was present during testing, occurring primarily at the side walls of the equipment, where the penetrometer tests were performed.

- The intrinsic non-uniformity of the sand. Due to the fact that the sand was a mixture of 2 different sand types, there might be instances where the resulting mixture is not uniform enough.

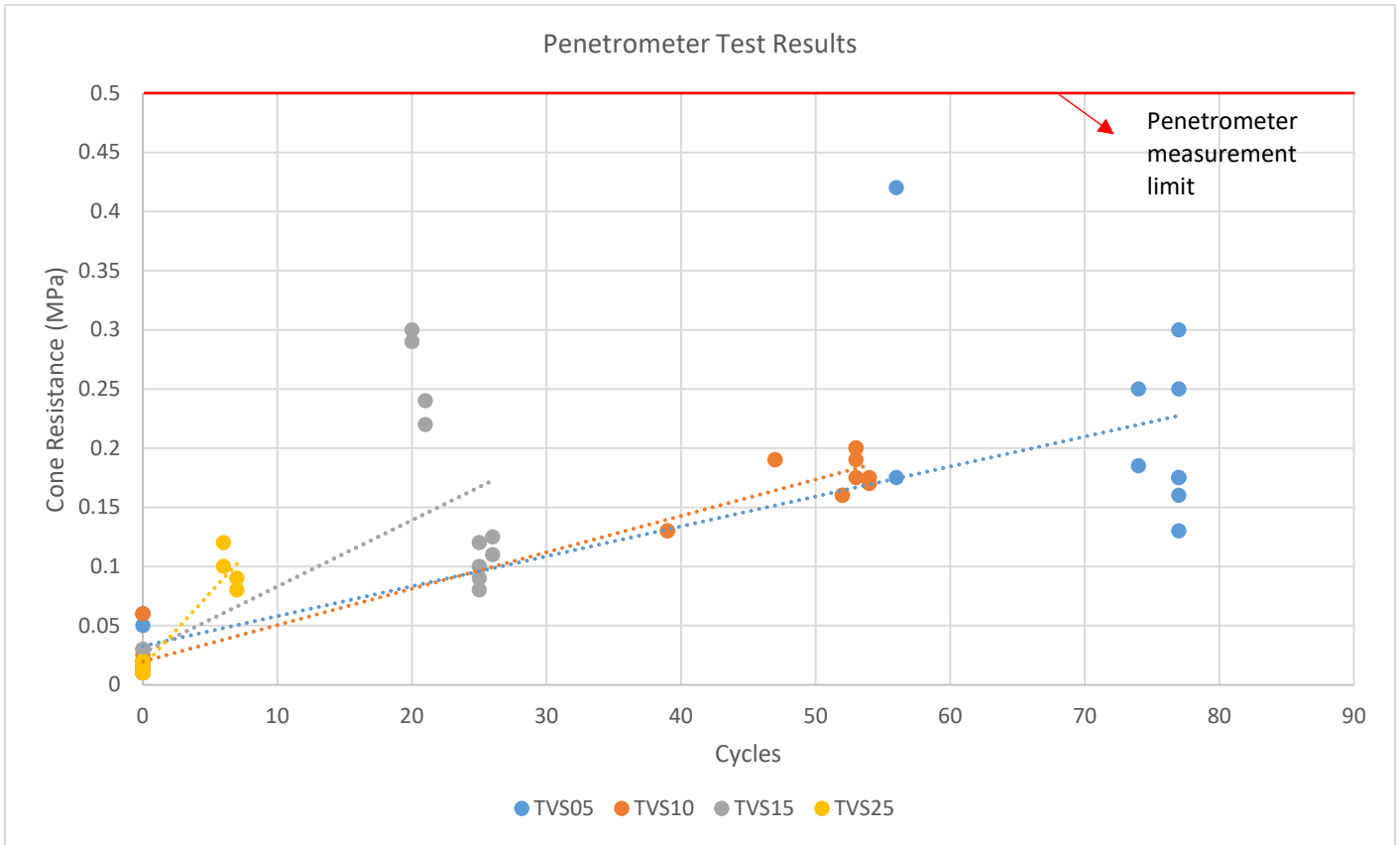


Figure 4-13 Penetrometer Test Results Graph

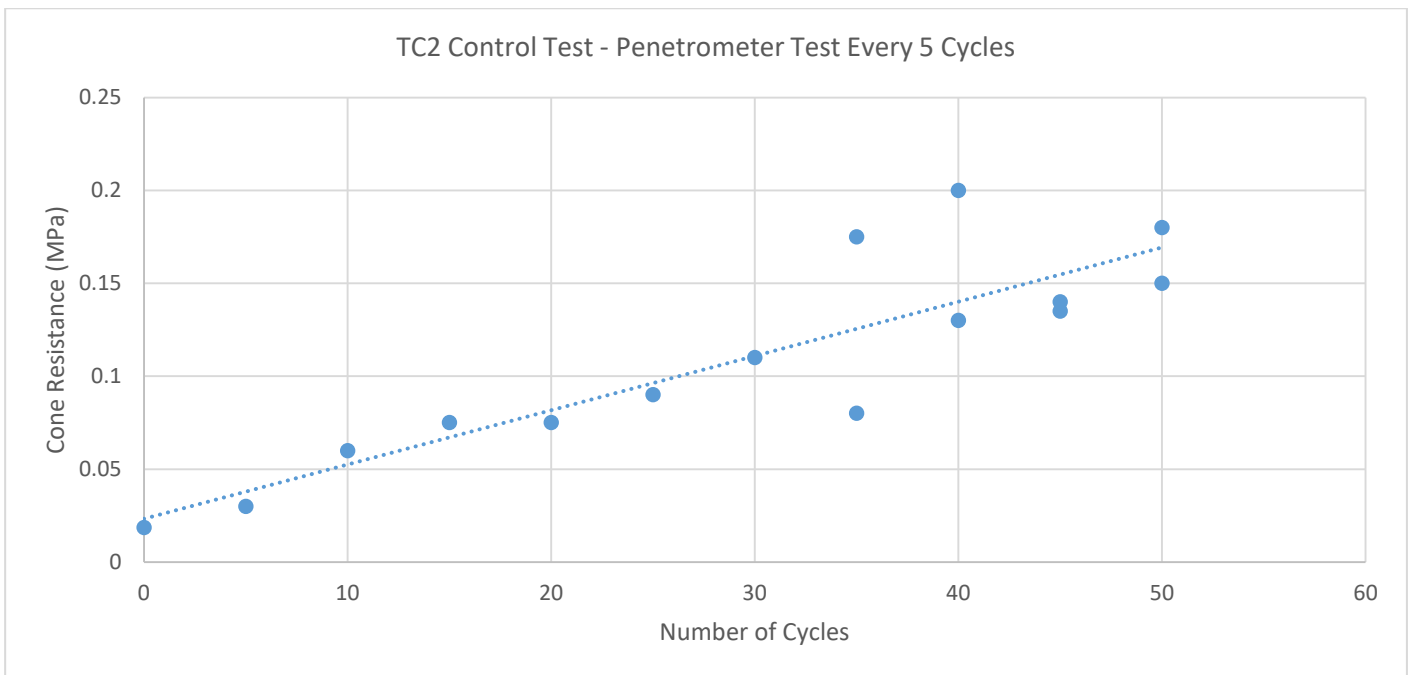


Figure 4-14 TC2 Test Results Graph (Penetrometer Test Every 5 Cycles)

Discussion on Penetrometer Test Results

Due to the limitations of the pocket penetrometer, the test is performed at a normal model gap width of 35 mm instead of full compression. Therefore the cone resistance values shown in Table 4-2 do not represent the worst-case condition.

Several penetrometer tests were conducted at full joint gap compression. However, the results are unable to be displayed, as the sand cone resistance is higher than the pocket penetrometer maximum measurement limit of 0.5 MPa. The red line shown in Figure 4-13 represents the upper range of the pocket penetrometer measurement capability, which also serves as the lower boundary estimation of the cone resistance value at joint full compression. Hence, the true cone resistance measurement at full compression might be much more significant than this value.

Relative Density

The values of relative density are correlated based on Schmertmann (1978), Baldi et al. (1986), Kulhawy & Mayne (1990) and Jamiolkowski et al. (2001). Several assumptions are made for this analysis:

1. The analysis mainly utilizes the Schmertmann correlation (1976), which takes into account soil vertical effective pressure to determine relative density instead of the more modern mean stress correlation. This is due to the lack of stress measuring instrument in the third horizontal axis perpendicular to the loading axis, rendering mean stress calculation inaccurate.
2. The vertical effective stress used in this analysis is assumed to be the overburden pressure exerted by the tire at 68 kPa.

The values of sand relative density are shown in Table 4-4. It can be observed that the relative density values are in the order of 20 to 30 percent, which is in the range of medium to low-density sand. However, as noted in the preceding section 4.1.4, the penetrometer tests were performed on a partly unloaded condition.

Table 4-4 Analyzed Values of Relative Density from Penetrometer Test Results

Location		Dr (%)									
		TVS05-01	TVS05-02	TVS05-03	TVS05-04	TVS05-05	TVS10-01	TVS10-02	TVS10-03	TVS10-04	TVS10-05
Wheel Side	Start	0	0	0	0	0	0	0	0	0	0
	End	23.543114	19.61926	23.54311	24.27666	23.54311	19.61926	25.30579	22.36019	23.54311	24.62869
Far Side	Start	9.4128157	7.006091	9.412816	0	0	0	0	9.412816	0	0
	End	35.099686	28.25138	30.6581	28.25138	22.36019	19.61926	24.62869	22.36019	23.16047	24.62869
Average	Start	4.71	3.50	4.71	0.00	0.00	0.00	0.00	4.71	0.00	0.00
	End	29.32	23.94	27.10	26.26	22.95	19.62	24.97	22.36	23.35	24.63
Cycles		56	77	77	74	77	39	53	52	54	47
Location		Dr (%)									
		TVS10-06	TVS15-03	TVS15-04	TVS15-05	TVS15-06	TVS15-07	TVS15-08	TVS25-01	TVS25-02	
Wheel Side	Start	0	-	0.262968	0	0	0	0	0	0	0
	End	25.305787	-	30.21059	26.56392	17.41408	18.56266	14.76513	16.15594	14.76513	
Far Side	Start	0	-	0.262968	0	0	0	0	0	0	0
	End	23.543114	-	30.6581	27.71251	19.10153	16.15594	13.21035	18.56266	13.21035	
Average	Start	0.00	-	0.26	0.00	0.00	0.00	0.00	0.00	0.00	0.00
	End	24.42	-	30.43	27.14	18.26	17.36	13.99	17.36	13.99	
Cycles		53	22	20	21	26	25	25	6	7	

Chapter 5 Finite Element Analysis

5.1. Overview

A simple finite element analysis is performed using the program Plaxis to predict the behavior of the model joint gap. The analysis utilized the well-known and simple hardening soil model to simplify the calculations and parameter determination. Plaxis is unable to model soil densification. Thus, an increase in sand density is assumed in the construction stages. The analysis is therefore divided mainly into 5 increasing density values from the normal condition of the sand to the fully densified condition.

5.2. Parameters

5.2.1. Model Sand

The parameters of the sand are assumed to be similar to the Baskarp Sand test results courtesy of Anaraki (2008), with some parameters added for calculation purposes. The elastic moduli are correlated from assumed cone resistance values. The sand cohesion is assumed as 1 kPa to ease the numerical calculation process. The parameters used in the analysis is shown in Table 5-1.

Table 5-1 Parameters of Baskarp Sand for hardening soil model in Plaxis

Hardening Soil Model Parameters								
No	Parameter	Symbol	Simulation Code					Unit
			M3-10	M3-25	M3-50	M3-100	M3-150	
1	Mass density	ρ_d	2,645	2,645	2,645	2,645	2,645	t/m ³
2	Dry density	γ_d	17	17	17	17	17	kN/m ³
3	Saturated density	γ_{sat}	18	18	18	18	18	kN/m ³
4	Friction Angle	ϕ	27	27	30	35	40	°
5	Minimum void ratio	e_{min}	0,548	0,548	0,548	0,548	0,548	
6	Maximum void ratio	e_{max}	0,929	0,929	0,929	0,929	0,929	
7	Initial void ratio	e_{init}	0,929	0,929	0,929	0,9	0,7	
8	Cohesion	c	1	1	1	1	1	kPa
9	Secant Modulus	E_{oed}	6	13	25	50	75	MPa
10	Tangential Modulus	E_{50}	10	25	50	100	150	MPa
11	Unloading-Reloading Modulus	E_{ur}	30	75	150	300	450	MPa

The fully densified condition is the assumed state that the sand undergoes after a certain amount of loading cycles. Full densification of the sand implies a maximum friction angle of 40° and a reduced initial void ratio of 0.7.

5.2.2. Gina Gasket

The Gina gasket is assigned as a linear elastic, non-porous model. The parameters of the gasket are shown in Table 5-2.

Table 5-2 Parameters for the Gina gasket

Gina Model Parameters				
No	Parameter	Symbol	Value	Unit
1	Mass density	ρ_d	2.645	t/m ³
2	Dry density	γ_d	0.1046	kN/m ³
3	Saturated Density	γ_{sat}	0.1046	kN/m ³
4	Elastic Modulus	E	1	MPa
5	Initial void ratio	e_{ini}	0.5	
6	Poisson's Ratio	ν (nu)	0.495	

5.2.3. Interface

The interface parameter input for the sand models the interaction between the sand and the steel model lining. Kishida (1987) stated that the roughness of the steel, along with the friction angle of the sand affects the interaction strength, with the highest recorded friction coefficient of 0.75. Taking into account the low friction angle, and the relatively smooth steel plate, the interface strength is set at 0.6 times the soil strength.

The interface stiffness is set at a different ratio than the strength. As the sand displacement occurs parallel to the interface, the stiffness parameter that governs this action is the shear stiffness. However, calculation of the shear stiffness is different to that of the normal stiffness, which follows the formula

$$G_i = R_{inter}^2 G_{soil} \leq G_{soil}$$

$$E_{oed,i} = 2G_i \frac{1 - \nu_i}{1 - 2\nu_i}$$

The desired shear stiffness of the interface is 1/4th that of the soil. Therefore to accommodate the difference in the strength and stiffness ratios, special interface material models were assigned. The properties are shown in Table 5-3. The interface strength between the Gina gasket and the sand is set as rigid to ease the calculation process, as the sand is assumed to be always in direct contact with the gasket.

Table 5-3 Interface parameter input

Interface Properties					
No	Model	Friction Angle (°)	E_{oed} (Mpa)	E_{50} (Mpa)	E_{ur} (Mpa)
1	M3-10	18	2	2.5	7.5
2	M3-25	20	2.5	3.75	11.25
3	M3-50	23	4.3	7.5	22.5
4	M3-100	27	6.9	13	39
5	M3-150	30	8.45	16.5	49.5

5.3. Model Structure

Overview

The geometry of both the model is shown in Figure 5-1, which features the 35 mm gap that contains the sand sample at the top, and the compressed Gina gasket at the bottom. The top boundary is unrestrained while including a uniform load with a magnitude of 68 kPa which simulates the maximum overburden pressure.

The bottom boundary is modeled as a fixed Gina gasket to enable the generation of initial stresses. However, the bottom part is deactivated during the loading steps to allow for the gasket to experience shear deformation. The side boundaries are the steel plate, with interfaces assigned to simulate

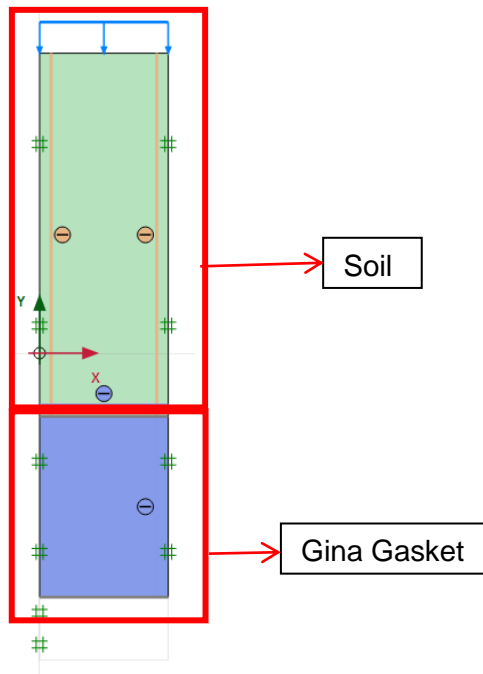


Figure 5-1 Model Geometry

Limitations to the Model

The finite element model structure is a simplified version of the test equipment. The limitations include:

1. The simplified geometry of the Gina gasket. Accurate gasket shape and bolt placement will render the model unstable as the model becomes asymmetrical
2. Hardening soil model assumes that every loading process follows the virgin compression curve. In reality, the sand has undergone compression from the preceding cycle.
3. Assumed interface values, discussed in section 5.2.3

Simplifications were made to ease the computation process for the computer as well as to conserve running time. This allows for multiple simulation configurations to be analyzed.

5.4. Calculation Steps

Plaxis lacks the option to model soil densification required for this project. Therefore the densification behavior must be assumed by varying the soil parameters at each stage of calculation. Each condition is assigned a code for ease of reference. The list of model codes is shown in Table 5-4

Table 5-4 Calculation Conditions

No	Cone Resistance (MPa)	E50 Value (MPa)	Loading Condition	Code
1	2	10	Loading 1.0 mm	M3-10-FS
2	2	10	Unloading 1.0 mm	M3-10-UF
3	5	25	Loading 1.0 mm	M3-25-FS
4	5	25	Unloading 1.0 mm	M3-25-UF
5	10	50	Loading 1.0 mm	M3-50-FS
6	10	50	Unloading 1.0 mm	M3-50-UF
7	20	100	Loading 1.0 mm	M3-100-FS
8	20	100	Unloading 1.0 mm	M3-100-UF
9	30	150	Loading 1.0 mm	M3-150-FS
10	30	150	Unloading 1.0 mm	M3-150-UF

The calculation steps consist of 3 parts: the generation of initial stresses due to overburden pressure, the displacement of the steel plate model lining, and the subsequent unloading. The calculation stages are shown in Figure 5-2.

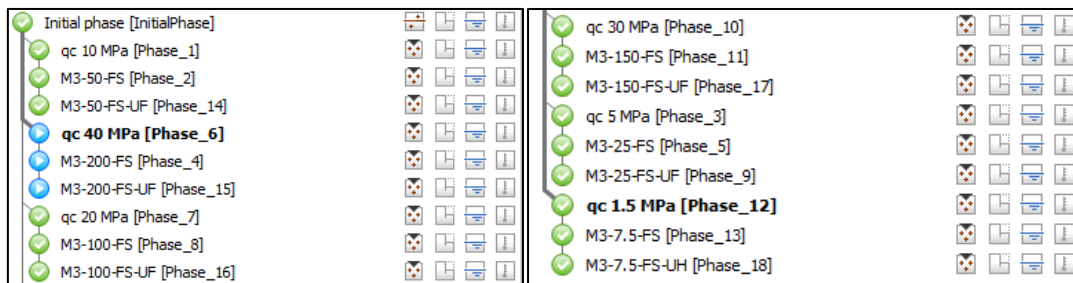


Figure 5-2 Calculation Stages

5.5. Model Results

5.5.1. Soil Stresses

Loading

During the loading stage, the soil stresses generally accumulate in the center of the soil body. One example is shown in Figure 5-3, where the highest values of the horizontal soil stress of stage M3-50-FS is concentrated in the middle. The high horizontal stresses are due to the deflecting lining wall acting on the horizontal axis, which functions as the highest load exerted on the soil. The stresses decrease greatly when approaching the top and bottom of the model. This is due to the soil body being able to move both downwards due to the elastic Gina gasket, and upwards into the overburden soil.

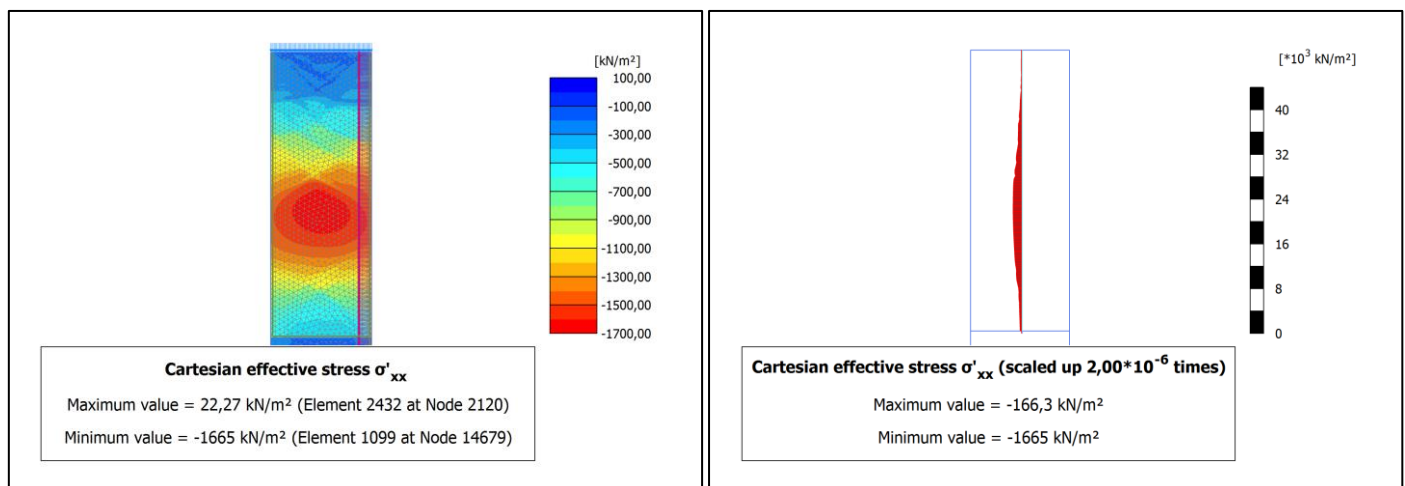


Figure 5-3 Horizontal Cartesian Effective Stresses of M3-50-FS

The vertical effective stress is reasonably less in magnitude compared to the horizontal stresses. This is due to the overburden and the friction acting as confining pressure, which is significantly lower than the deflection of the side wall. However, the vertical stresses are significantly greater than the overburden pressure. This condition is due to the friction from the walls confining the sand. Figure 5-4 shows the vertical effective stress.

Nevertheless, in both cases, it is demonstrated that the stresses are concentrated in the middle of the soil body, while gradually decreasing closer to the top and bottom edges. This suggests that the largest confinement occurs in the middle, while much less confinement is present at the edges.

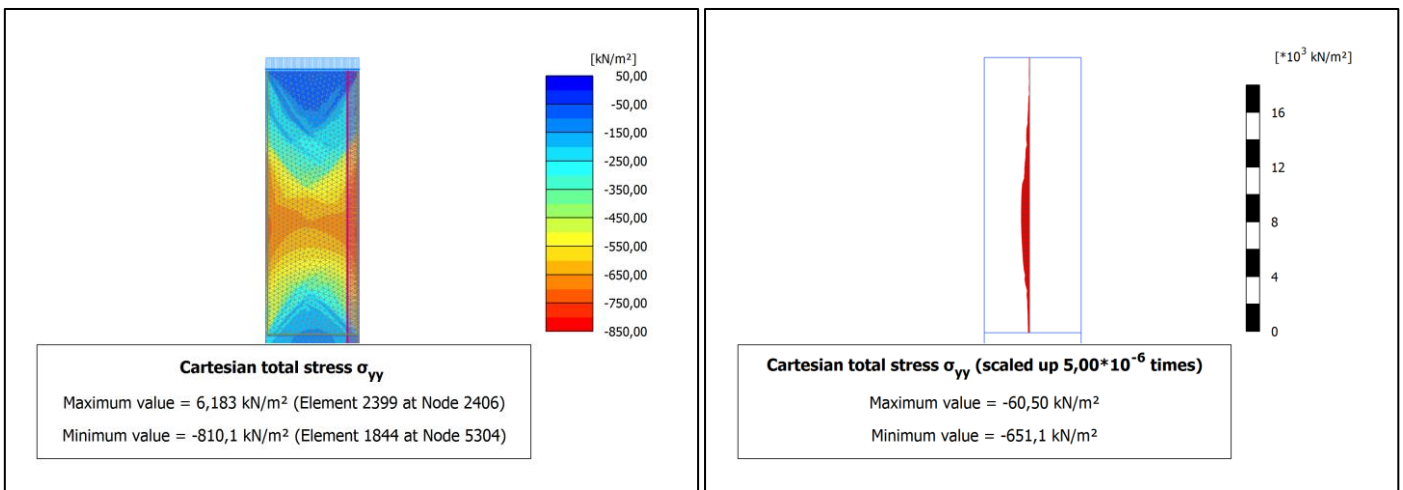


Figure 5-4 Vertical Effective Cartesian Stresses of M3-50-FS

Unloading

Figure 5-5 (left) shows the horizontal effective stress diagram during unloading, which features several geometric lines and patterns. Observing the shear stress diagram shown in Figure 5-5 (right) reveals that the geometric patterns are areas with zero shear, i.e., failure wedges. More on the failure pattern of the model will be explained in section 5.5.2

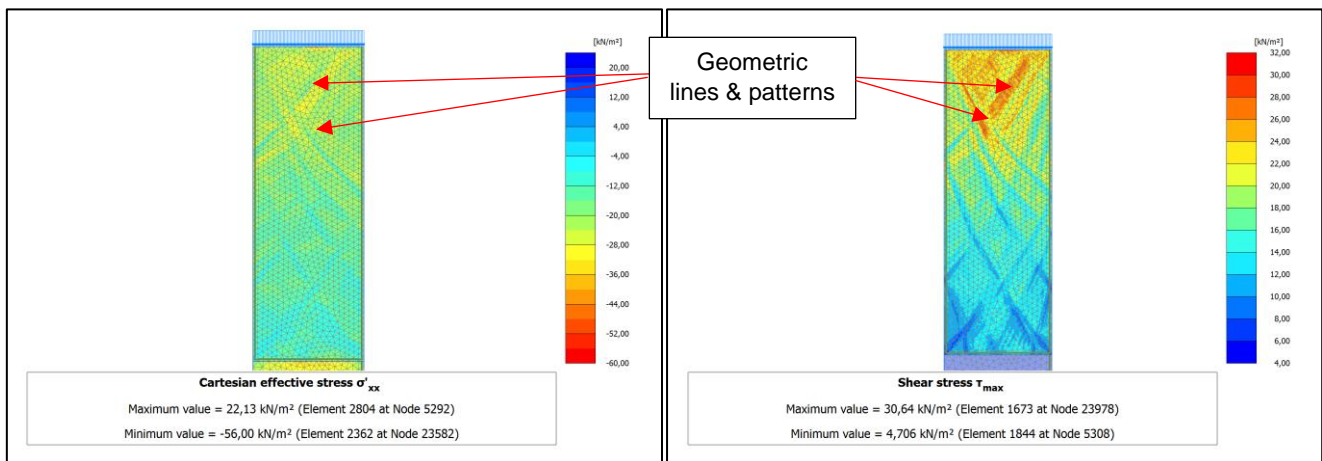


Figure 5-5 (left) Horizontal Effective Stresses, (right) Shear Stresses of M3-50-UF

Principal Stress Rotation

The principal stress directions are dependent on the external loads exerted on the soil element. In the unloading stage of the simulation, the overburden pressure is kept at 68 kPa, while the side plate returns to its original position. This implies that during unloading, the overburden pressure acts as the major load while no pressure is exerted on the sides. This, in turn, rotates the principal stress directions in between the two loading stages, as shown in Figure 5-6.

A rotation in the principal stresses suggests that the soil follows a different stress path, hence the different stress states between the two loading stages. Wrzesinski & Lechowicz (2013) showed that a rotation in principal stresses during loading amounts to a decrease in undrained soil strength. The effects of strength reduction are also more pronounced as the axis rotation approaches 90 degrees. The decline of strength might trigger unexpected failure patterns in the soil, which in turn allows rearrangement of soil particles and a reduction in volume.

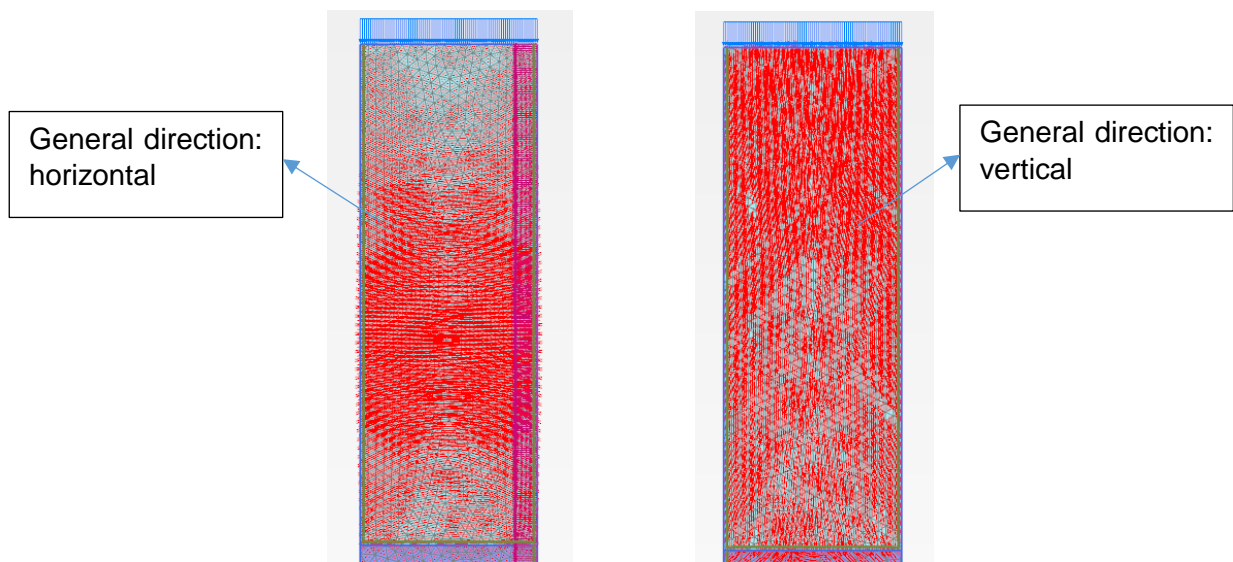


Figure 5-6 Principal Stress Directions M3-50 (left) loading, (right) Unloading

5.5.2. Plastic Points

Failure Pattern

The plastic points of M3-50 simulation condition are displayed in Figure 5-7, where it is observed that the failure wedges are different in each stage. Figure 5-7 (left) show that the failure wedges are located at the corner edges of the soil body, extending to a shallow center position, consistent with the general shear band in biaxial tests (Desrues, 1985 and Han et al., 1993). Most of the center part is dominated by cap + hardening points, which explains the decrease in soil volume and a substantial increase in soil stresses.

During the unloading stage, it is observed that the soil undergoes a further failure mechanism. Shear bands form across the height of the soil body, which suggests the soil body had failed and collapsed. The failure bands are noticeably deeper, as the entire soil body yields during unloading.

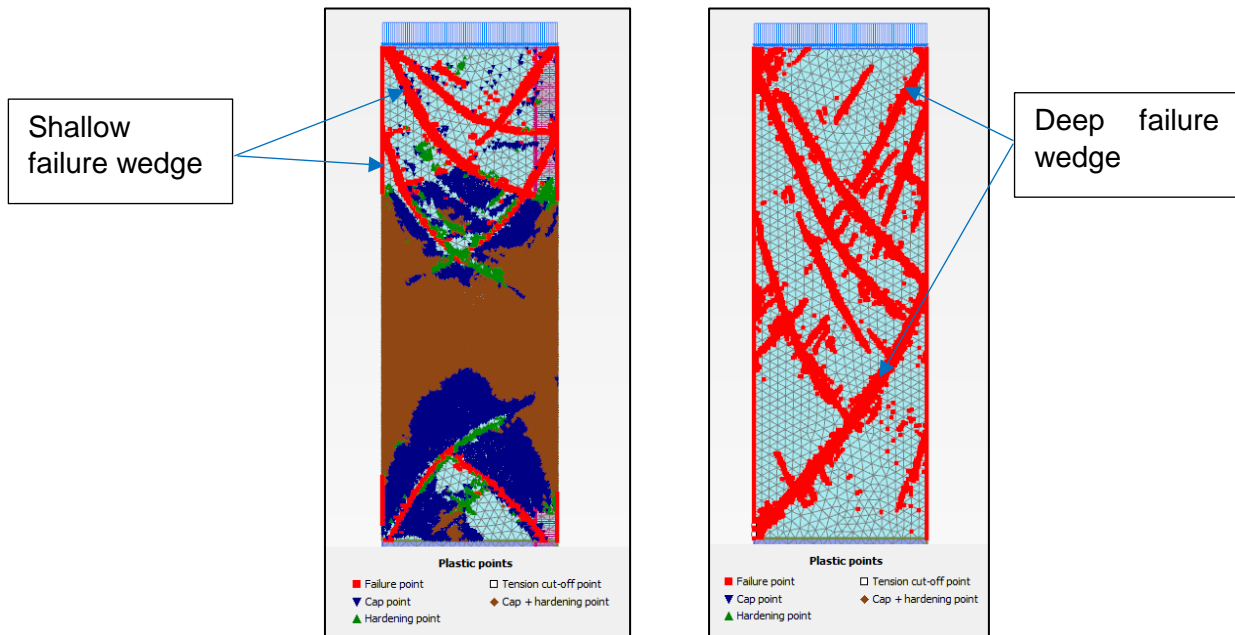


Figure 5-7 Plastic Points M3-50 (left) Loading, (right) Unloading

5.5.3. Deformations

Top Edge Deformations

A closer look at the deformation patterns shows that further compression occurs during the unloading process. Figure 5-8 (left) show that some heaving occurs during the loading cycle. However, it is also noted that the hardening soil model accommodates plastic deformation of the soil, which is horizontal in this case. The

process is shown in Figure 5-8 (right), where the unloading process reveals that the soil had compressed in volume.

Figure 5-8 (right) also indicates that the soil is introduced to further compression as the soil body rearranges itself, the principal direction changes and the vertical overburden pressure becomes the major principal stress. This particular deformation is carried around to the succeeding loading cycle.

In this particular simulation, the overburden pressure is modeled as a line load, and no physical material exists above the soil body. However in the test setup, the void would most likely be filled with the overlying soil, therefore potentially trapping more soil inside the joint gap.

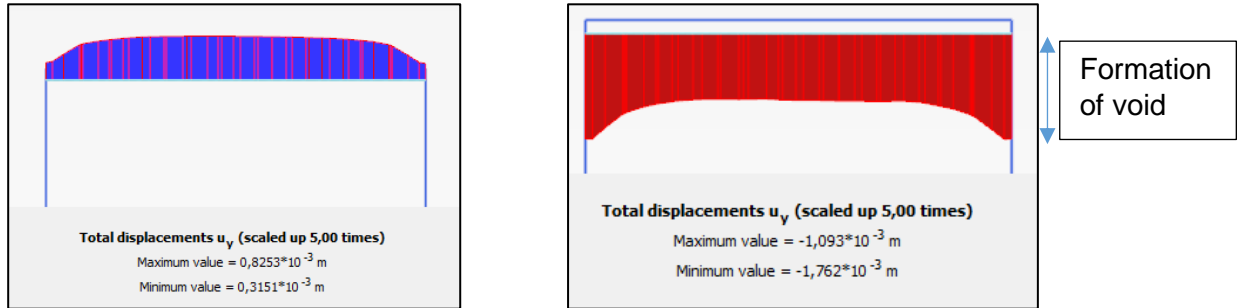


Figure 5-8 Top Edge Displacement (left) First Cycle, (center) Unloading, (right) Second Cycle

Gina Gasket Bottom Side Deformations

Figure 5-9 displays the development of gasket deflection at each stage. In the loading phase, the gasket is pushed downwards as the joint gap contracts. However, during unloading, the gasket does not return to its original position, where a small amount of deflection remains after unloading, as shown in Figure 5-9.

Overall, the vertical gasket deflection shows generally lower values when compared to the laboratory experiments.

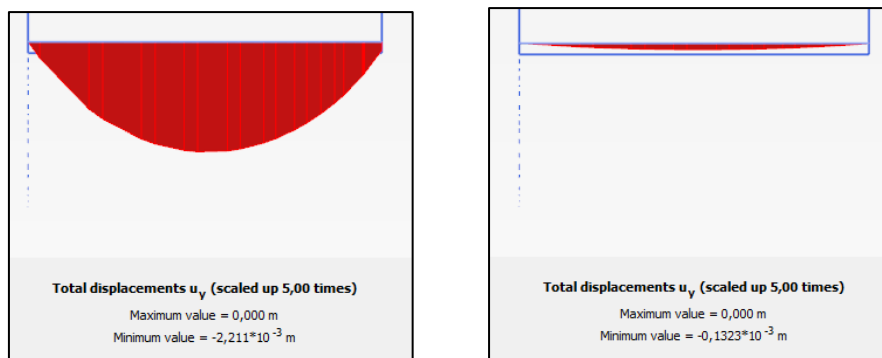


Figure 5-9 Gina Gasket Bottom Side Deflection (left) Loading, (right) Unloading

5.6. Effects of Changing Soil Density

5.6.1. Horizontal Stresses

The effect of increasing soil density has a particular effect on the soil stresses. An increase in sand friction angle translates to a proportionally greater increase in soil stress. Higher soil friction angle also amounts to a sharper gradient in the changes in stress conditions of the soil. Figure 5-10 shows that changes in density alter the failure wedge of the soil body.

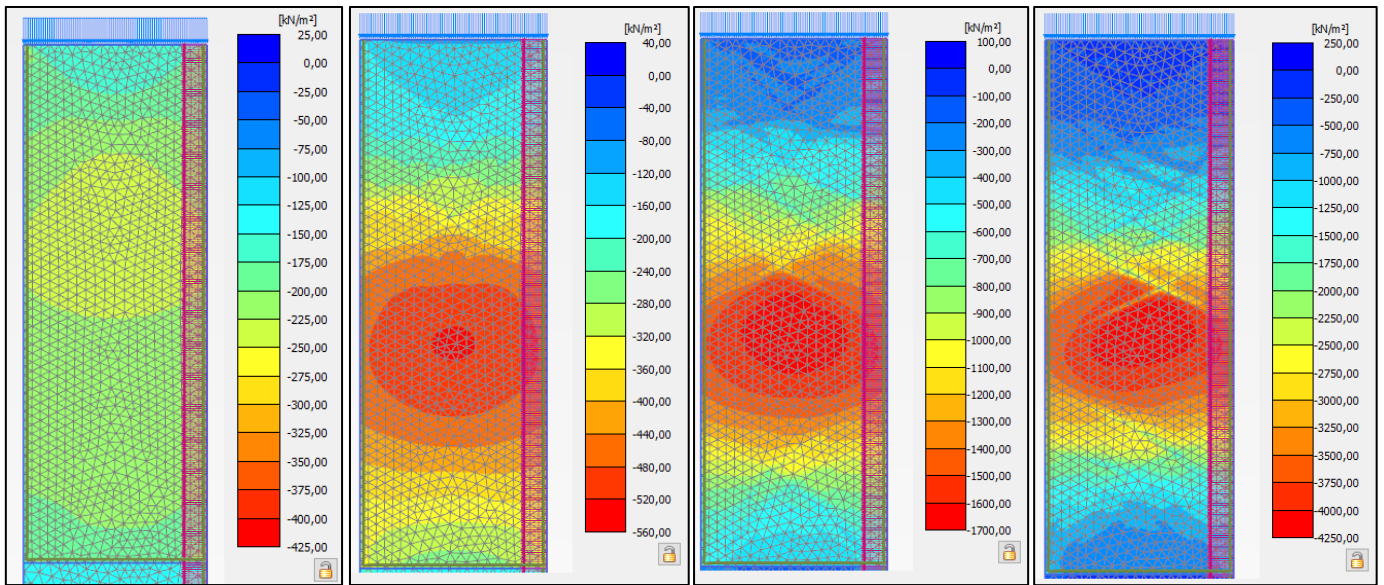


Figure 5-10 Effective Horizontal Stresses (left to right), M3-10-FS, M3-25-FS, M3-50-FS, M3-100-FS

The magnitudes of the stresses obtained in this analysis far exceed the load cell readings obtained in the laboratory experiments, especially at higher soil densities. Figure 5-11 shows the horizontal soil stresses plotted against the vertical gasket displacement of each simulation configuration with the results of simulation M3-150 is omitted due to its high magnitude of stress. It can be observed that at the E_{50} value of 100 MPa, the horizontal soil stresses reach 4 MPa, much greater than the recorded stresses obtained from the laboratory experiments. A more detailed comparison is discussed in section 6.1.

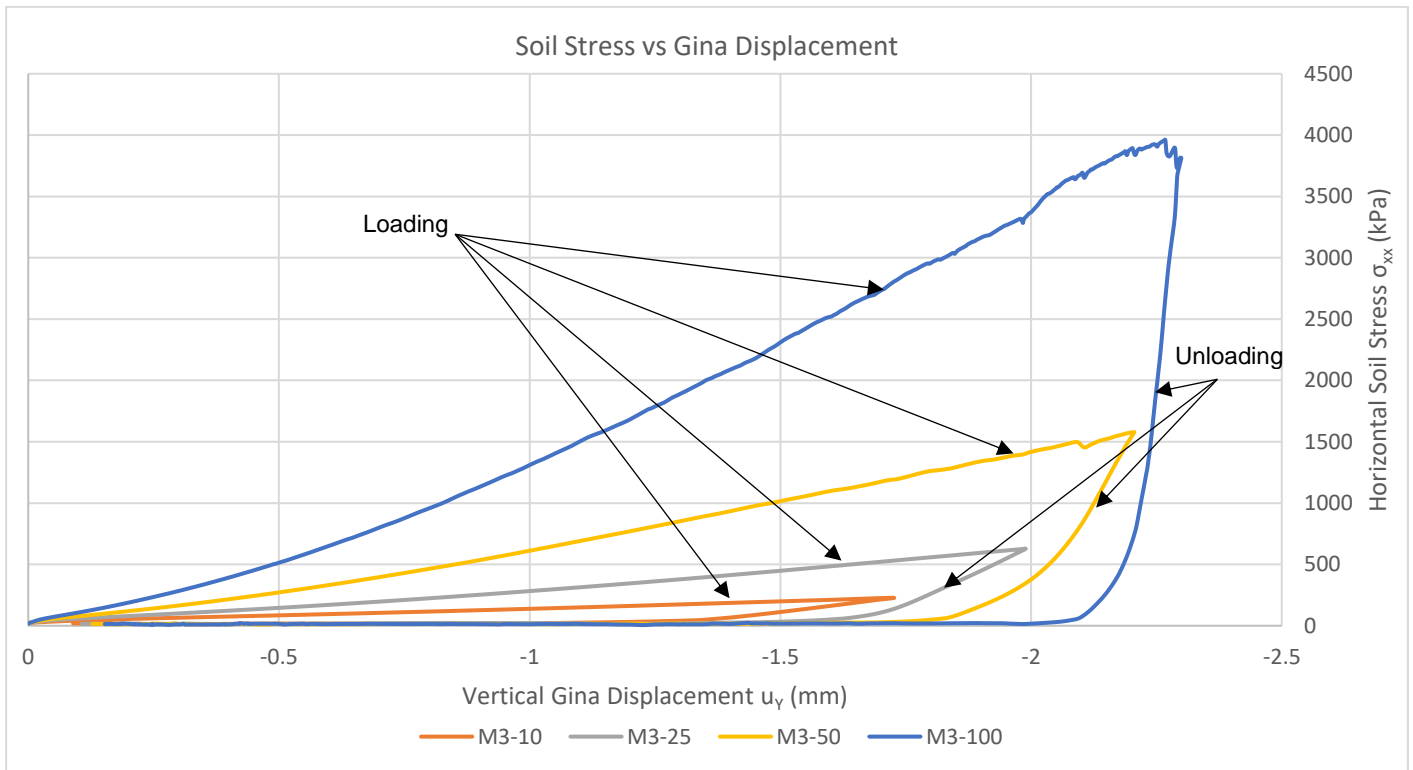


Figure 5-11 Horizontal Soil Stresses vs. Vertical Gina Displacement of Finite Element Simulation

5.6.2. Soil Deformations

Soil Top Deformation

The deformation of the top edge of the gap at the first cycle is shown in the graph displayed in Figure 5-12. It is observed that at every density, the top soil heaves and forms a crest. As the soil density increases, the height of the crest also increases. The increase in the crest height is apparently halted at higher densities.

It can be observed that at every density, the soil forms a void, as shown in Figure 5-13. Voids at the top of the joint gap might allow the overlying sand to enter the joint gap and further densifying the system. The size of the void changes with every density, however, considering that the joint gap sand is loose at the start of the first loading cycle, it can be assumed that the largest void forms at the beginning of each experiment.

The formation of voids occurs not only due to the yielding of the soil near the interfaces but also in part due to the change in the geometric form of the Gina gasket.

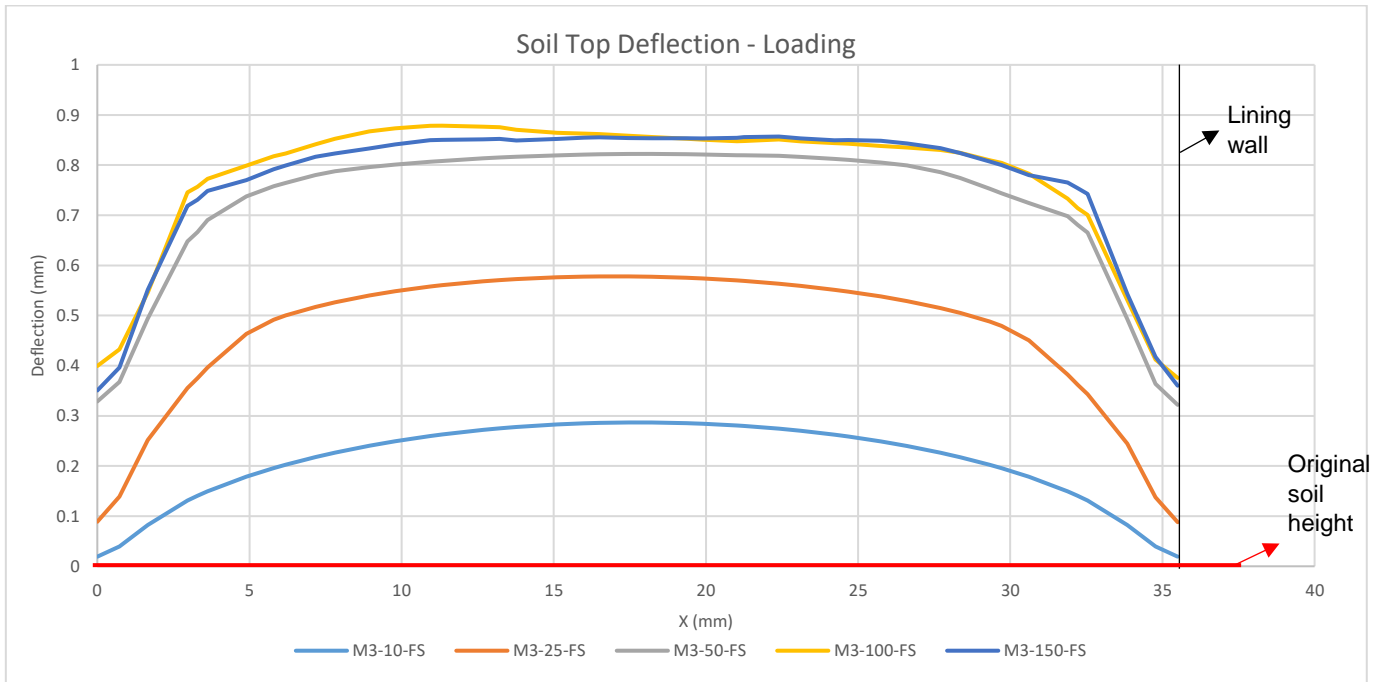


Figure 5-12 Soil Top Deflection during the Loading Stage at different densities

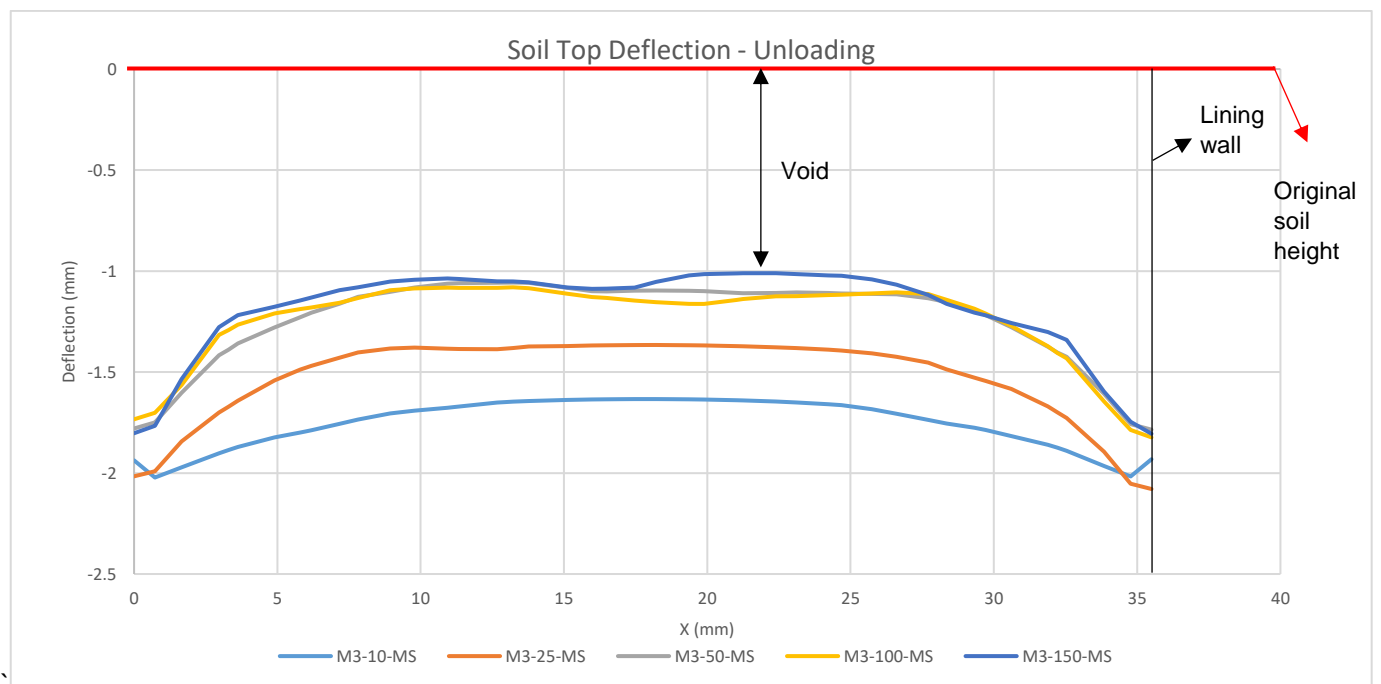


Figure 5-13 Soil Top Deflection during the unloading stage at different densities

5.6.3. Gina Gasket Deformations

Bottom Side Deflection

Figure 5-14 shows the initial gasket deflection during the first loading cycle. The Gina deflection is shown to increase with sand density. However, at higher densities, the change in deflection noticeably decreases. The threshold in the gasket deflection is due to the maximum shear deformation of the gasket.

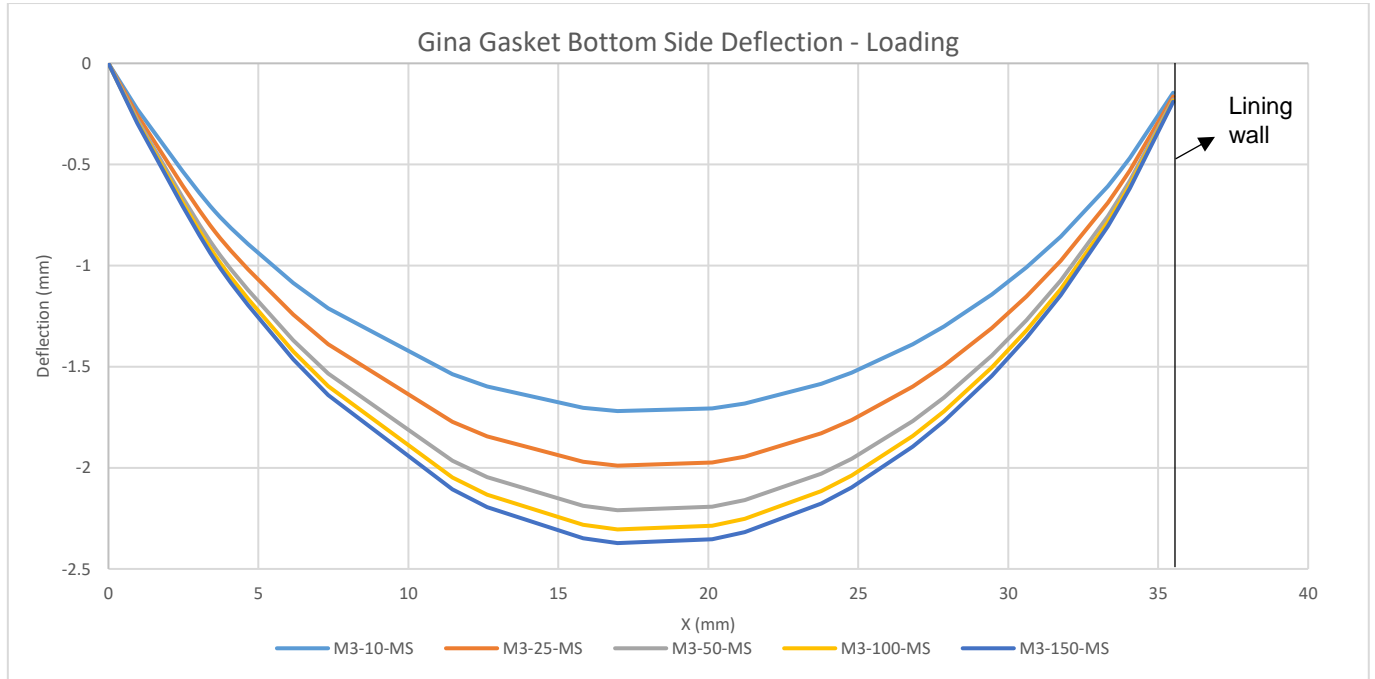


Figure 5-14 Gina Gasket Bottom Side Deflection during the Loading Stage at Different Densities

Chapter 6 Discussions

6.1. Laboratory Experiment Results versus Finite Element Analysis Results

Overview

The finite element model utilizes 1.0 mm stroke length at 2.8% strain. Therefore the comparison analysis is made with experiment TVS10-06 which have a similar magnitude of strain.

6.1.1. Evolution of Soil Stresses in a Cycle

The two models show different outputs in terms of recorded soil stresses. Figure 6-1 displays the results of experiment TVS10-06 at cycle 52 compared to finite element analysis M3-50 at the E_{50} value of 50 MPa. The former is plotted against time, while the latter is plotted against the calculation step.

It is shown that during the loading phase, the load cells read a sharp and rapid increase in stresses as opposed to the steady stress increase of the finite element simulation. This condition is due to the nature of the calculation. However, the unloading process shows a sharp decline in stresses similar to the laboratory experiment results.

The stresses obtained from the finite element analysis indicate that at the E_{50} value of 50 MPa, which correlates to 10 MPa magnitude of cone resistance, the stresses have reached the magnitudes of the last cycle in the experiment. This validates the analysis made in section 4.2.4, where the sand only reached moderate levels of density before displaying high levels of stress comparable to the last cycle.

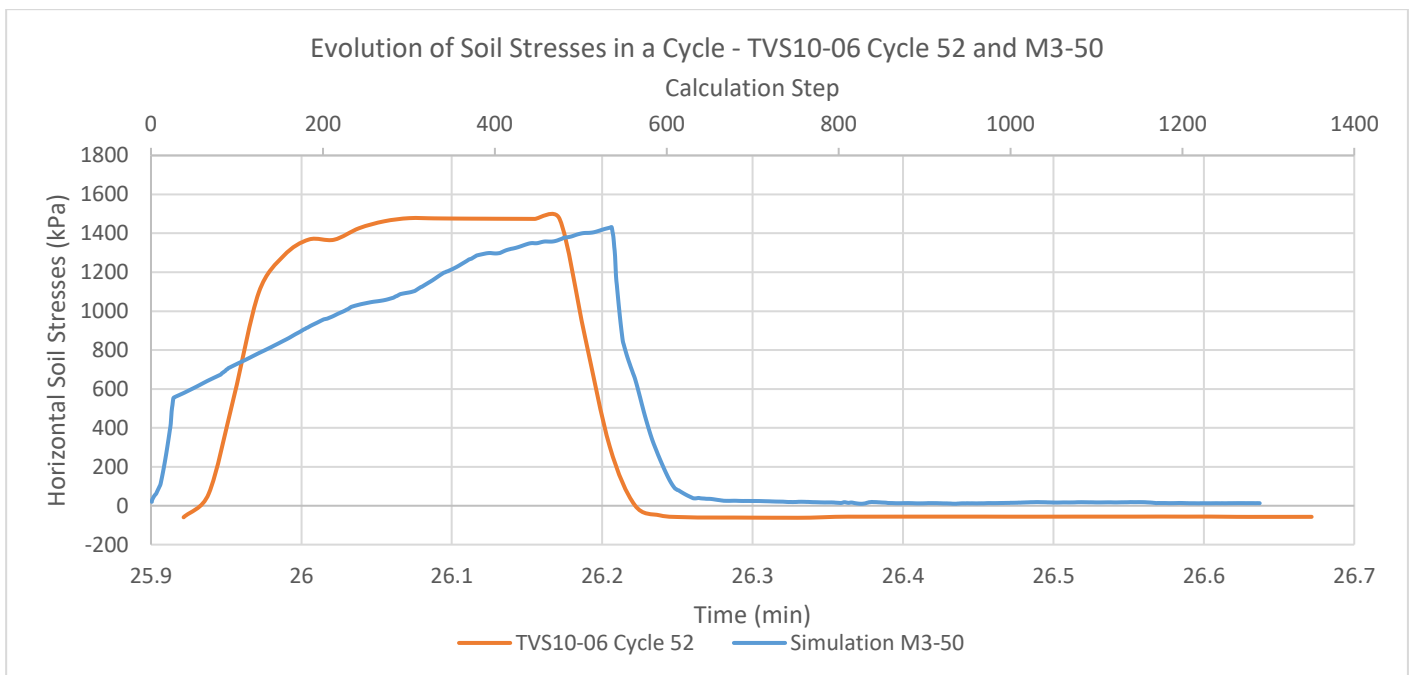


Figure 6-1 Soil Stress Comparison (TVS10-06 Cycle 52 and M3-50)

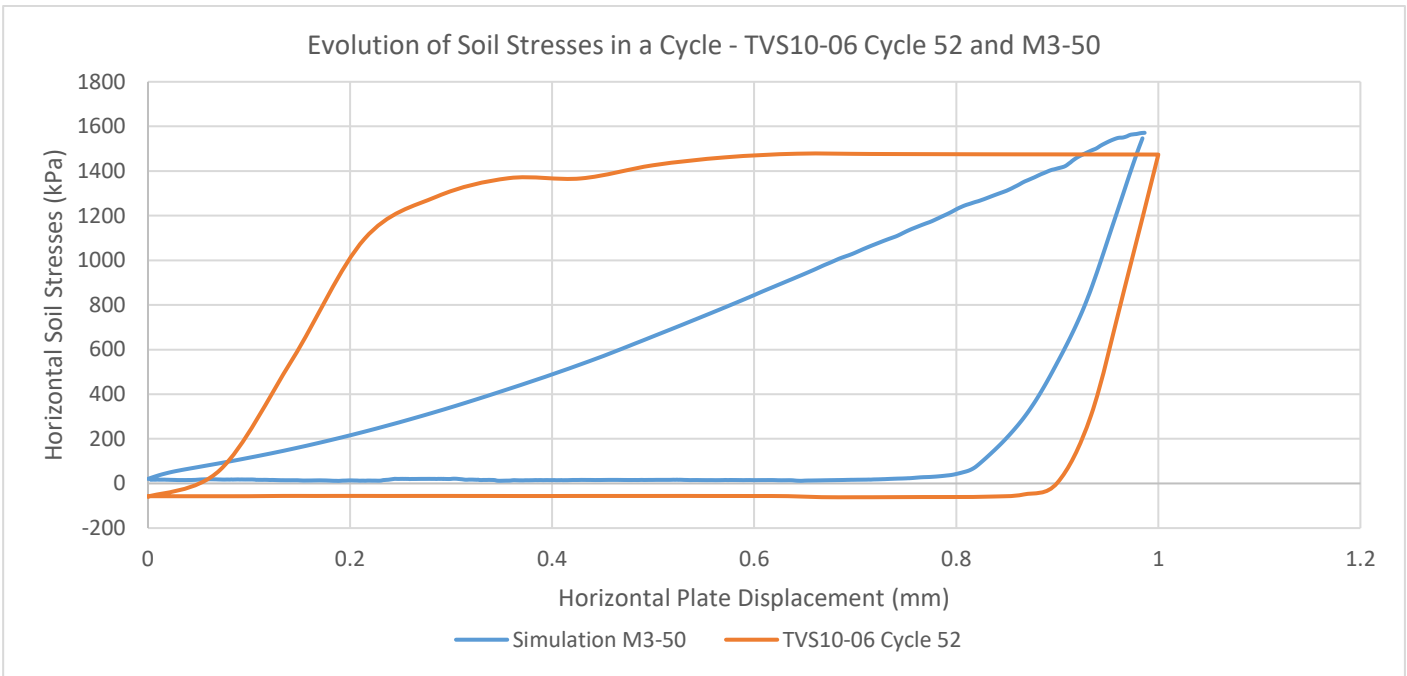


Figure 6-2 Horizontal Soil Stresses vs. Horizontal Plate Displacement – TVS10-06 Cycle 52 and M3-50

6.1.2. Soil Stresses vs. Gasket Displacement

Figure 6-3 shows the progression of stresses both during the laboratory experiment and the finite element analysis. In addition to the stresses, the values of gasket deflection for both types of analyses are different.

1. The vertical Gina displacement is generally lower in the finite element analysis compared to the laboratory experiment
2. The gasket rebound is not present in the finite element analysis

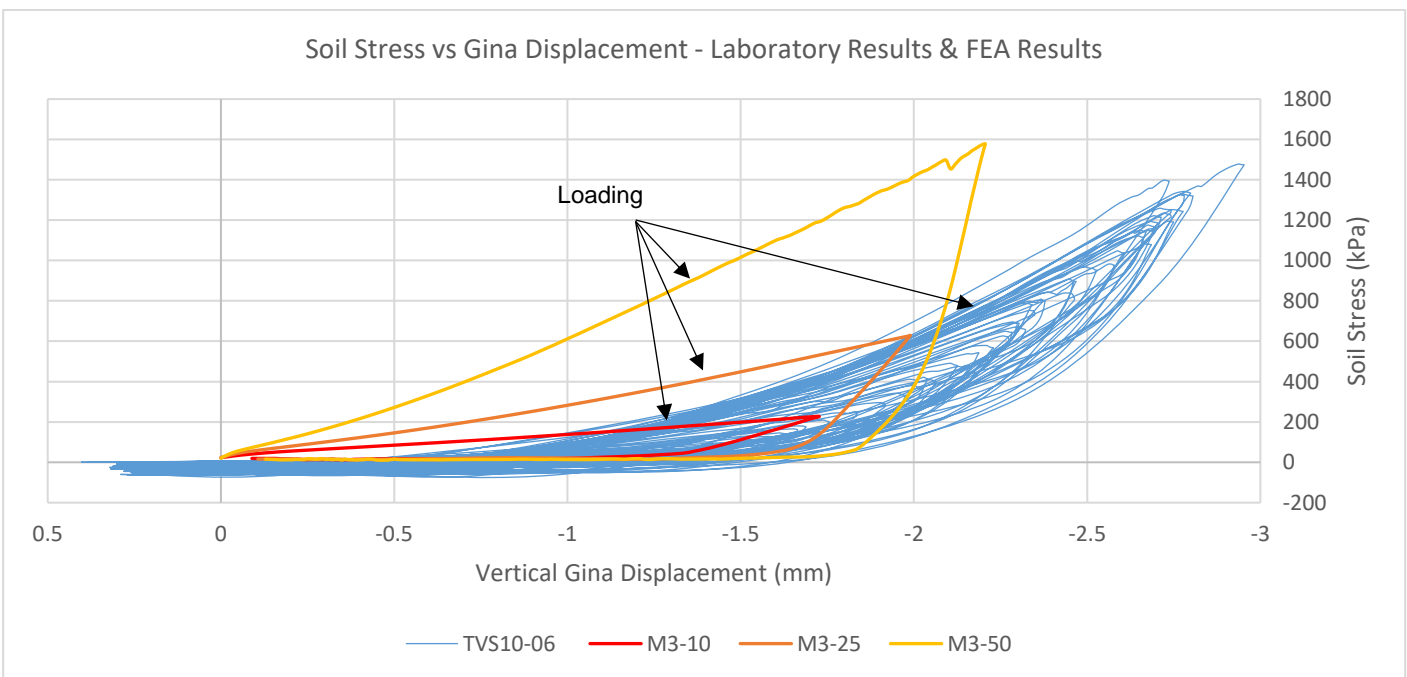


Figure 6-3 Soil Stress vs. Gina Displacement Comparison between TVS10-06 and Plaxis Analysis

These differences are due to the nature of the hardening soil model, which only takes into account the virgin compression curve, resulting in lesser values of displacement. Furthermore, the effect of densification and the addition of new materials into the system is not supported by the hardening soil model.

However, the gradients of both loading and unloading curves are comparable between the two analysis methods. Therefore, adjustments are made for the finite element analysis curves, which results in the graph shown in Figure 6-4. The adjustments are as follows:

1. Gasket deflections are offset for the different simulations; 0.7 mm for M3-50, 0.3mm for M3-25 and 0 mm for M3-10
2. The unloading-reloading stiffness E_{ur} is decreased from 3 times E_{50} to 2 times E_{50}

After the adjustments were made, the behavior of both analysis types is more comparable. The loading curves are similar in gradient while the unloading curve shows similar stiff behavior, albeit with different gradients. Further decreasing the E_{ur} to 1.5 times E_{50} might be able to fit the unloading curves better. However, Plaxis does not allow values of E_{ur} to be less than twice that of E_{50} .

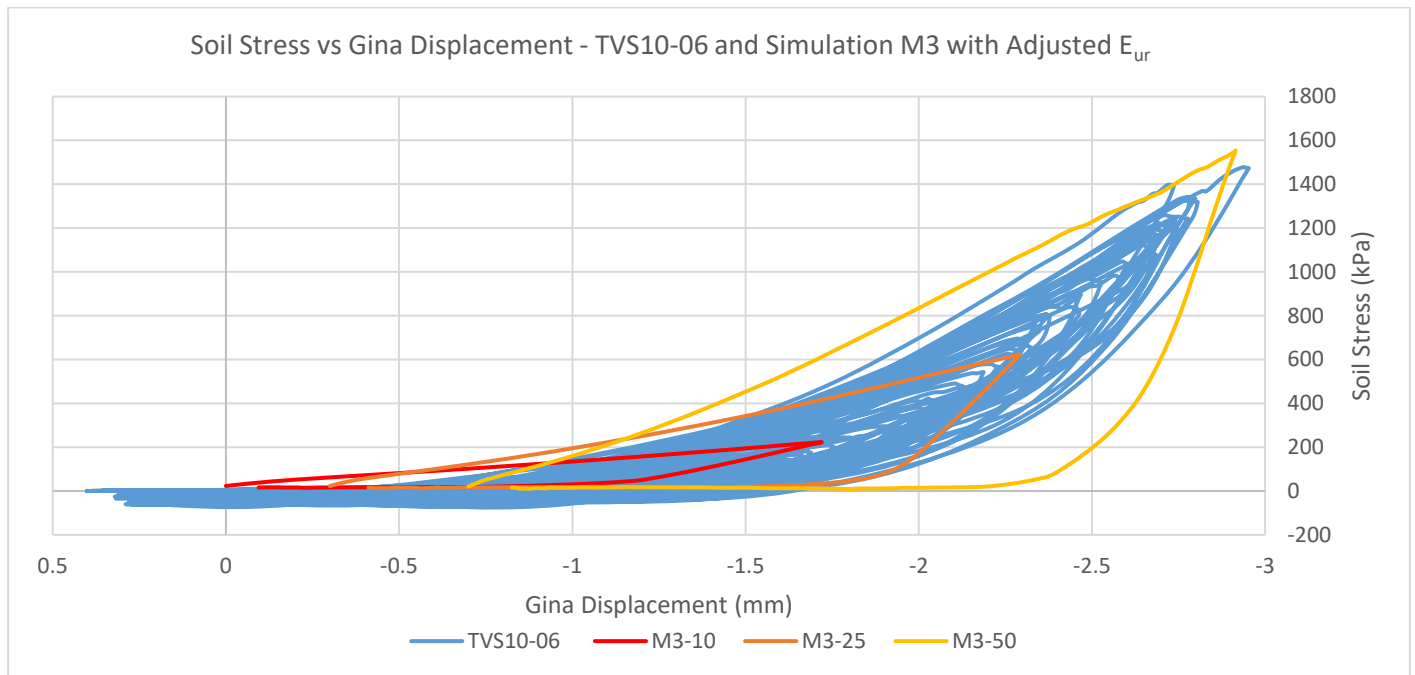


Figure 6-4 Soil Stress vs. Gina Displacement Comparison between TVS10-06 and Plaxis Analysis with adjusted E_{ur}

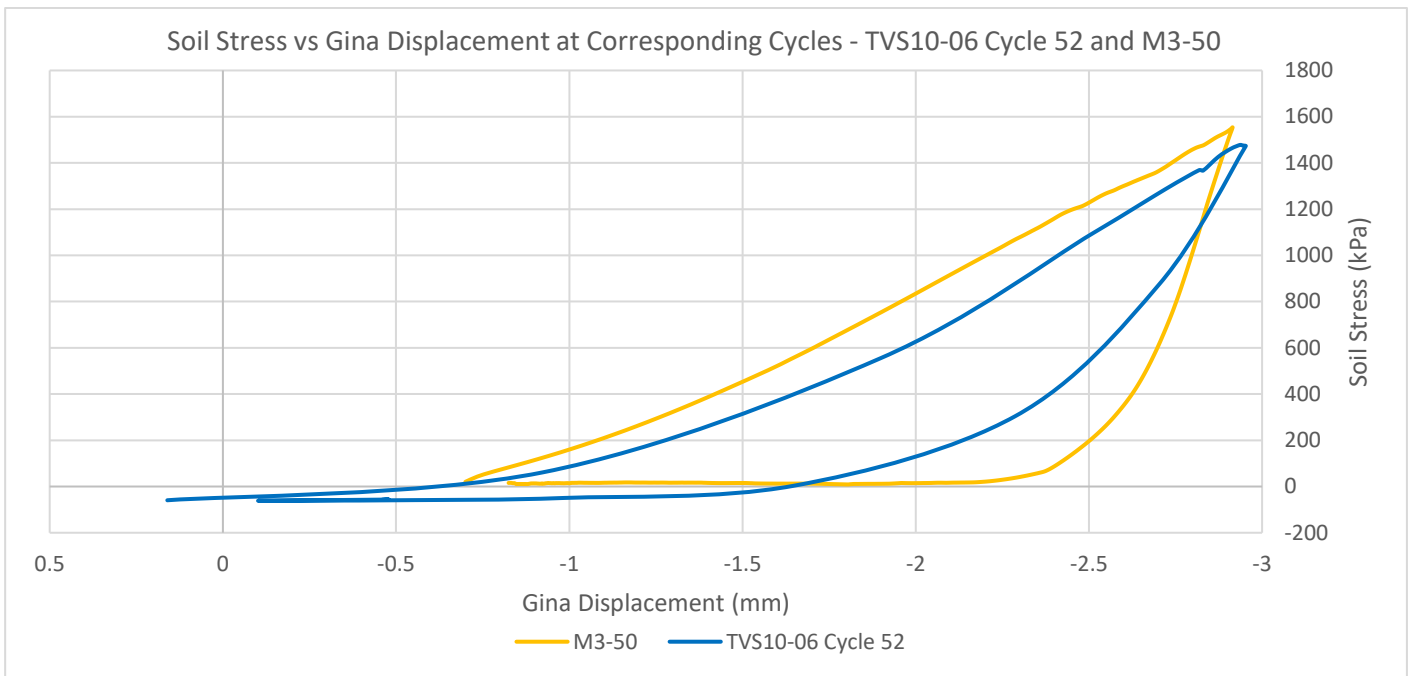


Figure 6-5 Horizontal Soil Stress vs. Vertical Gina Displacement Comparison between TVS10-06 at Cycle 52 and M3-50

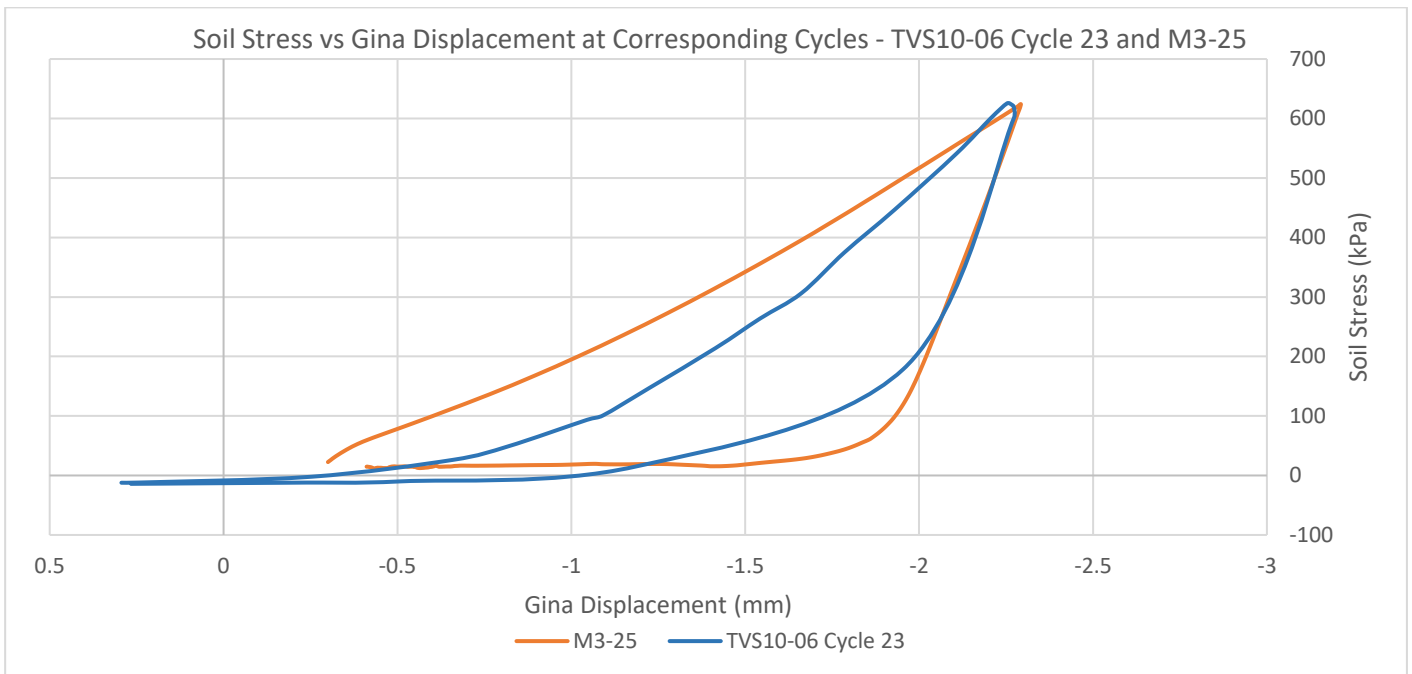


Figure 6-6 Horizontal Soil Stress vs. Vertical Gina Displacement Comparison between TVS10-06 at Cycle 23 and M3-25

Figure 6-5 and Figure 6-6 show the same graphs displayed in Figure 6-4. The former compares the experiment results at cycle 52 with finite element simulation M3-50 while the latter compares cycle 23 with simulation M3-25. It can be concluded from the two figures that the behavior shown in the finite element model is comparable to that of the physical model.

6.2. Sand Effective Vertical Stress

Overview

The stress path analysis discussed in section 4.2.3 assumes a constant vertical soil stress at the magnitude of the overburden pressure. Hence the vertical soil stresses have an insignificant effect on the constructed stress path. However, the finite element analysis results show that the vertical stresses rise during loading and fall during unloading.

In the comparative analysis conducted in section 6.1, the finite element model was readjusted to fit the experiment results better. Hence, it can subsequently be used to predict the soil behavior and, to an extent, estimate the vertical effective stresses occurring in the experiment.

6.2.1. Role of Interface Friction

Figure 6-7 shows that the vertical stresses during unloading are much greater than assumed. The values of 320 kPa and 760 kPa for simulation M3-25 and M3-50 respectively are significantly more than the previously assumed overburden pressure of 68 kPa. However, it can also be observed that during unloading, the vertical pressure rapidly decreases, which is in line with the previous assumption. The implications of these findings are as follows:

1. Higher stress might amount to greater densification of the joint gap sand.
2. The resulting principal stress directions might rotate from horizontal to vertical earlier than assumed. Rotation of principal stresses decreases the capacity of the soil (Wrzesinski & Lechowicz, 2013), the hence earlier rotation would theoretically allow the soil to fail earlier than initially assessed.

Therefore it can be concluded that the side friction plays a major role in the behavior of the joint gap sand.

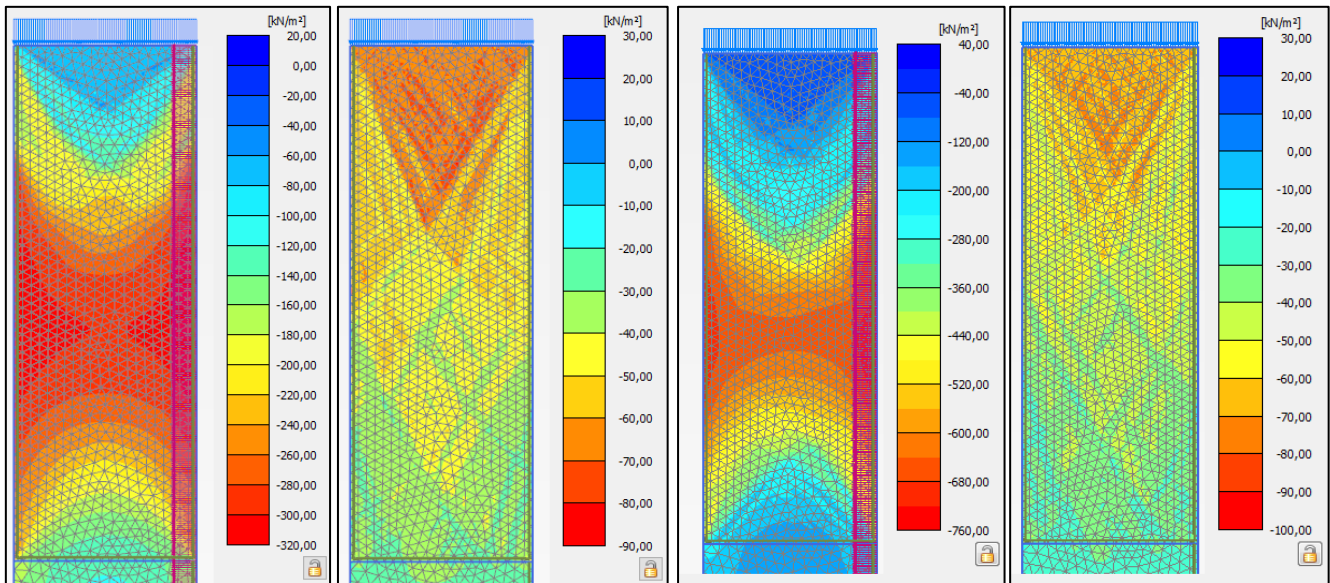


Figure 6-7 Vertical Effective Soil Stresses (left to right) M3-25 Loading, M3-25 Unloading, M3-50 Loading, M3-50 Unloading

6.2.2. Stress Path Analysis with Adjusted Parameters and Assumptions

The apparent increase in vertical stress signifies that the assumption made for the stress path analysis in section 4.2.3 is incorrect. Therefore the assumptions were further adjusted as follows:

- During loading, the vertical stress increases linearly from 68 kPa to the maximum vertical stresses obtained from the finite element analysis. The magnitudes of the maximum vertical stresses are as follows:
 - 152 kPa for cycles 1 to 20
 - 313 kPa for cycles 21 to 40
 - 728 kPa for cycles 41 to 52
- During unloading, the vertical stress decreases linearly from the maximum vertical stress to 68 kPa
- Out of the plane horizontal stress is defined as 0.5 times the greatest value between the vertical stress and the main horizontal stress.

The resulting stress path is shown in Figure 6-8. It can be observed that the graph is shifted more to the right compared to the stress path shown in Figure 4-12. This implies that the rotation of the principal axis occurs earlier than expected.

However, some of the points are still located above the maximum failure line, which signifies that some assumptions are still wrong. Accurate measurement of the vertical and horizontal stresses is required in order to perform a more detailed stress path analysis.

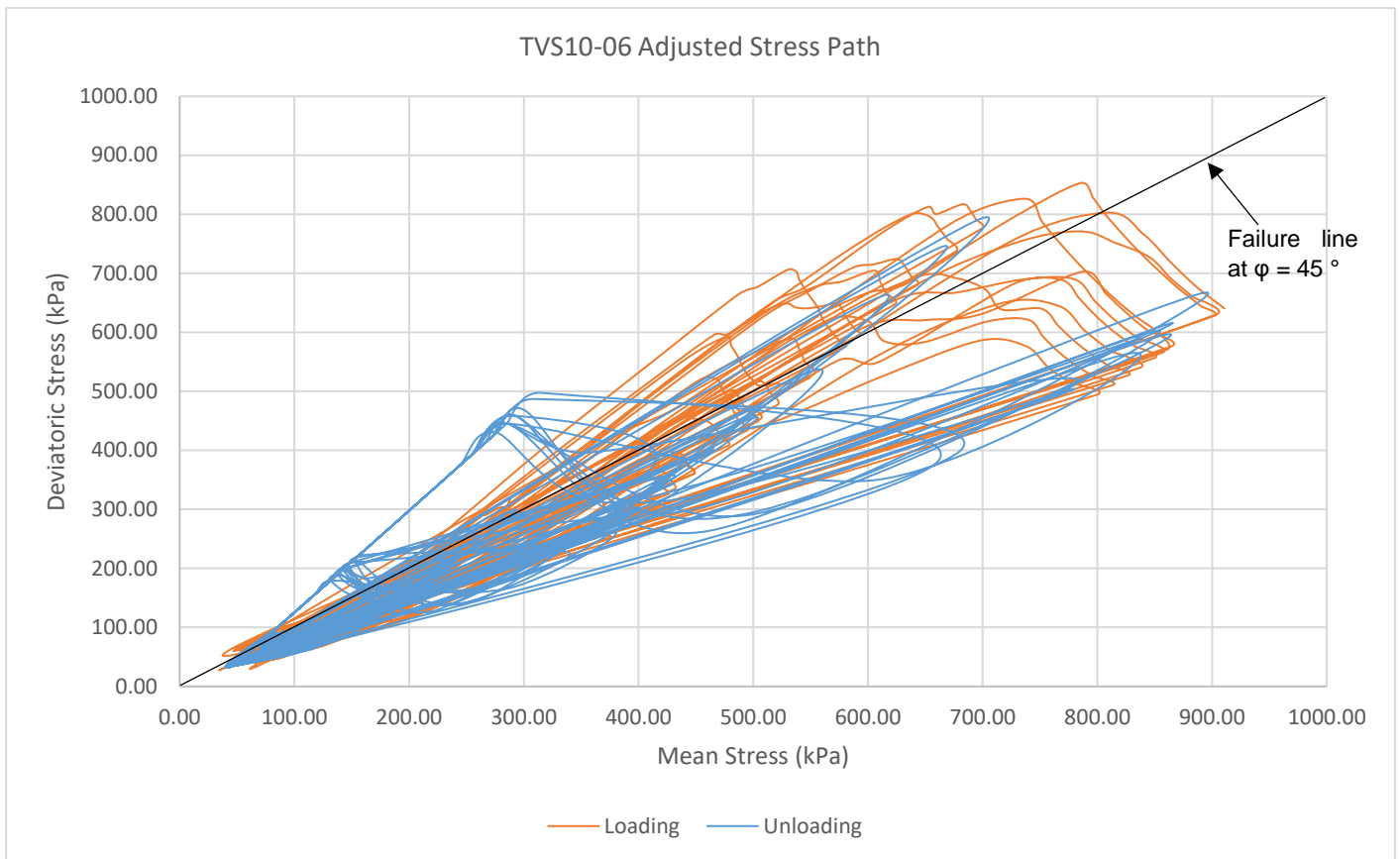


Figure 6-8 Stress Path with Adjusted Parameters for TVS10-06

6.3. Force Analysis

Overview

Rehabilitation of the Rotterdam Metrotunnel immersion joints involves pushing back the Gina gasket using steel strips mounted on the inside of the tunnel. The strips apply force to the gasket in order to push the soil out of the joint gap and return the gasket to its original position. A finite element analysis is performed in order to estimate the magnitude of the force.

6.3.1. Model Structure and Calculation Conditions

The model structure is similar to the original M3 finite element model explained in section 5.3 with several modifications added. The model structure is shown in Figure 6-9.

To obtain forces, the bottom side of the Gina must be fixed in place. A horizontal steel plate model is added on the bottom side of the gasket, with another vertical plate connected to the middle part. The bottom end of the vertical plate is fixed both translationally and rotationally at the bottom boundary line.

The gasket underwent failure after approximately 50 cycles of loading and unloading. Hence, the simulation utilizes sand material model M3-50, which had previously been adjusted to fit the experiment at cycle 52 in section 6.1.

The calculation steps of the simulation commence with the full compression of the joint gap. The magnitude of the gasket deflection produced in this stage is noted and applied as a fixed upwards displacement in the subsequent stage. This gasket pushing back action is denoted by the black arrow in Figure 6-10. Two conditions are considered in these stages; pushing back 1/3, and the entirety of the gasket bottom area. The former involves activating the 1/3 middle part of the horizontal plate while latter involves activating the entire horizontal steel plate during the pushing back action, denoted by the horizontal blue line shown in Figure 6-10. These two distinct calculation modes represent the lower and upper boundary approach of the analysis respectively.

A similar analysis is also performed at full expansion of the joint gap width. The calculation analysis of this analysis is shown in Figure 6-11 while the descriptions are listed in Table 6-1.

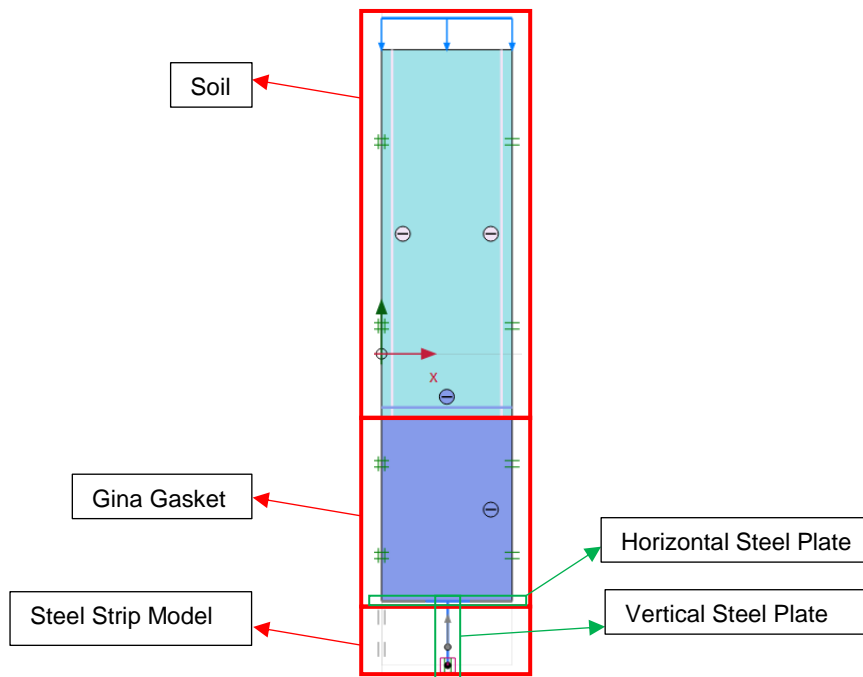


Figure 6-9 Modified Plaxis Model Structure

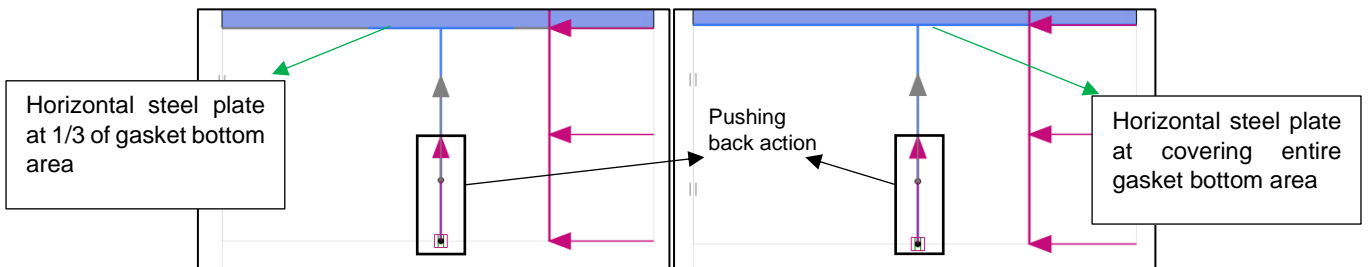


Figure 6-10 Detailed Model of Steel Support Strip (left) Hori Covering 1/3 Gasket Bottom Area, (right) Support Strip Covering Entire Gasket Bottom Area

Table 6-1 Force Analysis Calculation Conditions

No	Phase	Calculation Conditions
1	qc 10 Mpa	Self weight load
2	M3-50-FS	Gap full contraction/loading
3	M3-50-FS-FA 1/3	Pushing back 1/3 gasket area at full gap contraction
4	M3-50-FS-FA Full	Pushing back entire gasket area at full gap contraction
5	M3-50-UF	Gap full expansion/unloading
6	M3-50-UF-FA 1/3	Pushing back 1/3 gasket area at full gap expansion
7	M3-50-UF-FA Full	Pushing back full gasket area at full gap expansion

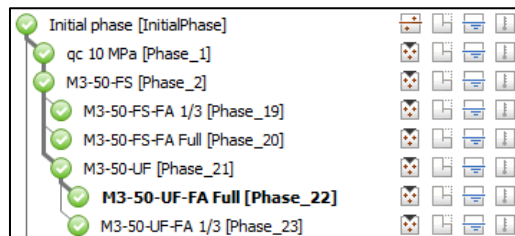


Figure 6-11 Force Analysis Calculation Stages

6.3.2. Results and Analysis

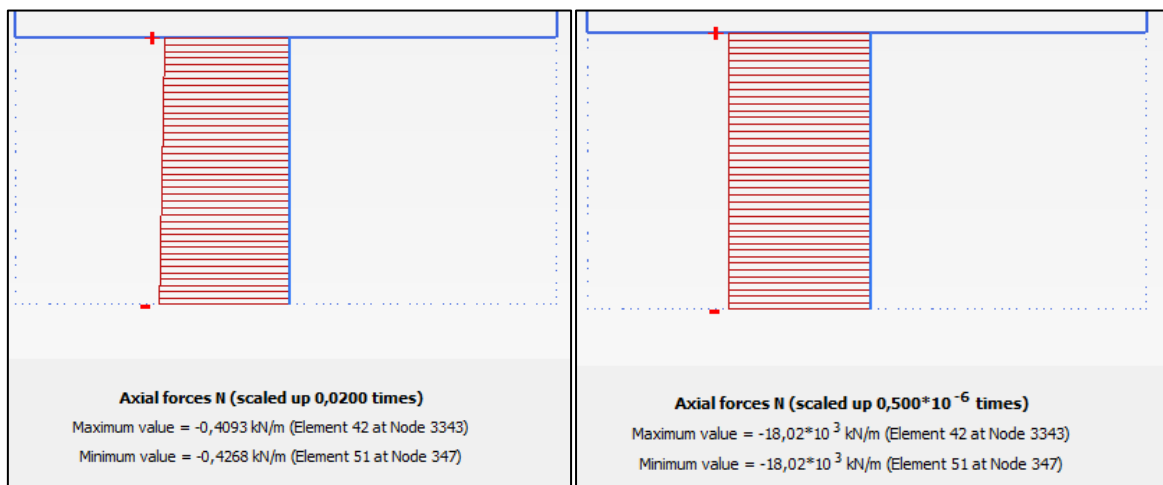
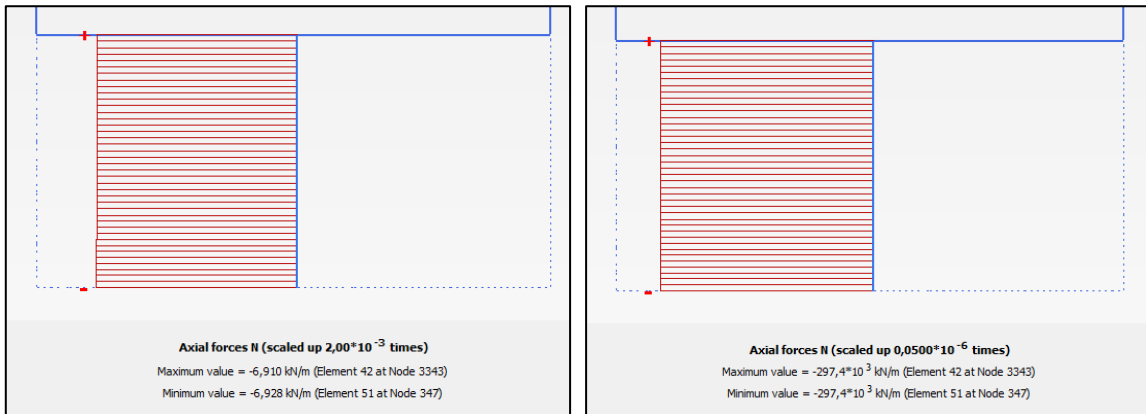
Pushing-back Force

The resulting pushing-back forces at full joint contraction are 6.928 kN/m for the lower boundary and 297400 kN/m for the upper boundary, as shown in Figure 6-12. At full joint expansion, the forces are much lower: 0.4268 kN/m for the lower boundary and 18020 kN/m as shown in Figure 6-13. Taking into account a scale

of 1:3 between the model and the prototype, the predicted forces occurring in the prototype are shown in Table 6-2.

Table 6-2 Force Analysis Results

No	Calculation Stage	Joint Gap Condition	Gasket Area Pushed	Model Force (kN/m)	Estimated Force in Prototype (kN/m)
1	M3-50-FS-FA 1/3	Full Contraction	1/3	6.9	20.7
2	M3-50-UF-FA 1/3	Full Expansion	1/3	0.4	1.2
3	M3-50-FS-FA Full	Full Contraction	All	297000	891000
4	M3-50-UF-FA Full	Full Expansion	All	18020	54060



Analysis on Gasket Vertical Deflection

The difference in forces between the upper and lower boundary analysis is consistently large due to the behavior of the Gina gasket in the model. Figure 6-14 and Figure 6-15 show the vertical gasket deflection for full joint contraction and full joint expansion respectively. It can be observed in both figures that for pushing-back actions that affect 1/3 of the gasket area (figures on the left), the steel plate pushes the gasket aside while the soil above the gasket retains its position.

However, for pushing back actions that affect the entire gasket bottom area (figures on the right), the steel plate manages to push some of the sand upwards. Hence it can be assumed that some of the sand inside the gap is pushed out of the joint gap.

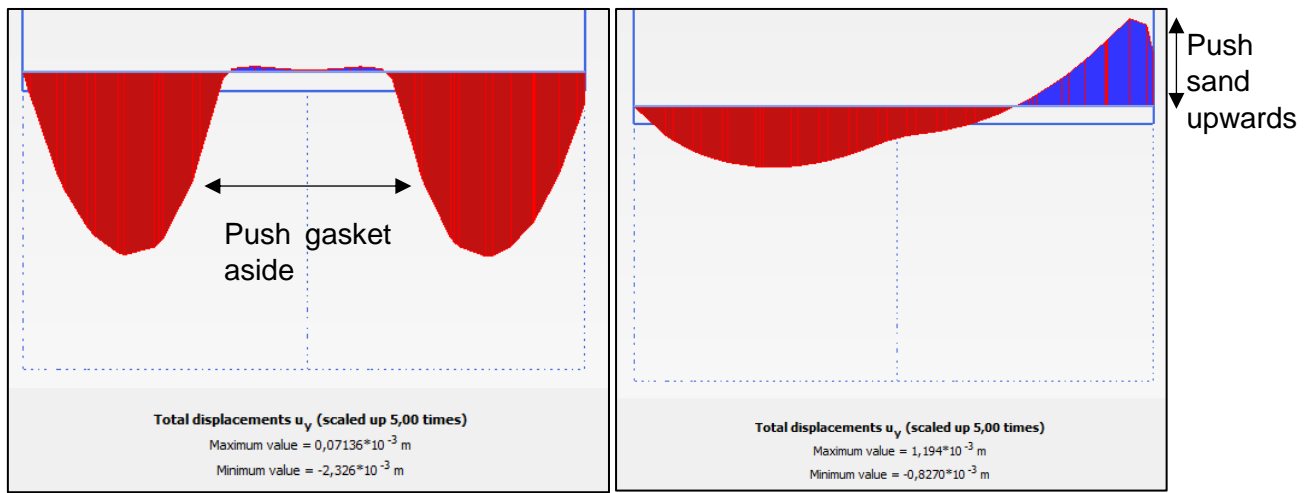


Figure 6-14 Gina Gasket Bottom Deflections (left) M3-50-FS-FA 1/3, (right) M3-50-FS-FA Full

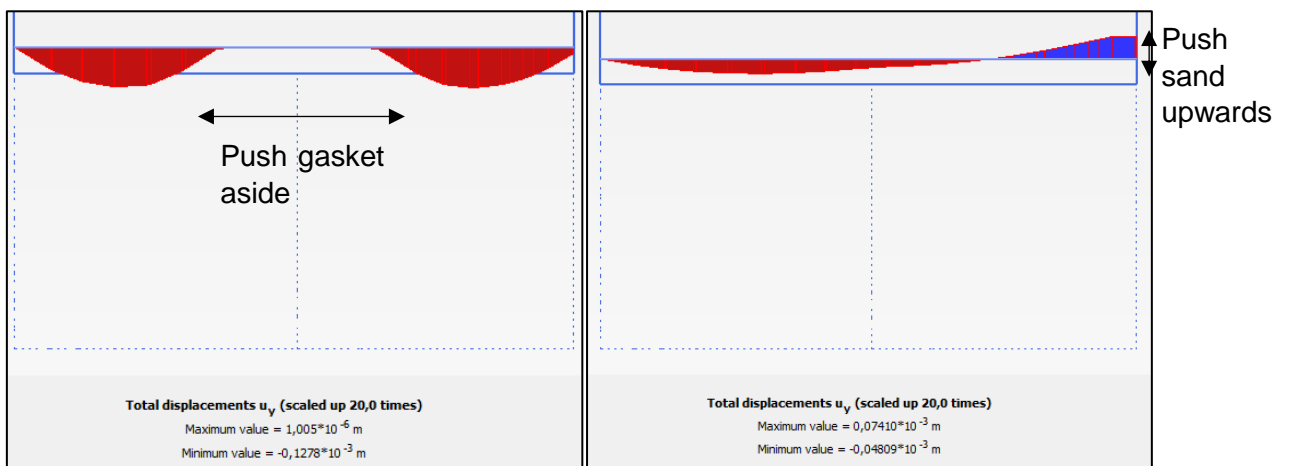


Figure 6-15 Gina Gasket Bottom Deflections (left) M3-50-UF-FA 1/3, (right) M3-50-UF-FA Full

Discussions and Conclusions on Force Analysis

The force analysis generally produces large forces in order to push the entire gasket bottom side upwards. This shows that the sand inside the joint gap has densified to the extent that the horizontal stresses acting on the lining wall increase to the point that the resulting friction resistance requires immense force to overcome. On the other hand, pushing back a much smaller area might result in the remaining area of the gasket simply giving way to the side. Hence the sand inside the joint gap remains unaffected by the pushing-back action.

However, it can be observed that the difference in resulting forces between full contraction and full expansion of the joint are quite large, in the order of 30 times. This is due to the relatively low density of the sand inside the joint gap during unloading.

To reduce the required pushing-back force, some suggestions are made:

- Consider performing joint reparations during the colder seasons, as the joint gap would be at maximum expansion, thus decreasing the soil density.
- Consider taking out some of the sand inside the joint gap before applying the pushing-back force on the steel strip. This would reduce the density of the sand and further alleviate the required pushing-back force.

Chapter 7 Conclusions and Further Research

7.1. Conclusions

Q1 : Do the multiple cycles of loading and unloading, due to the annual expansion and contraction of the immersion joint, generate increased stresses in the soil inside the joint?

1. Results of multiple laboratory experiments show that the cyclic movement of the lining wall significantly increases the soil stresses.
 - At 0.5 mm stroke length, recorded soil stresses increased from near zero prior to loading, and reaching up to 280 kPa after 75 loading and unloading cycles.
 - At 1.0 mm stroke length, recorded soil stresses increased from near zero prior to loading, and reaching up to 1300 kPa after 50 loading and unloading cycles.
 - At 1.5 mm stroke length, recorded soil stresses increased from near zero prior to loading, and reaching up to 3200 kPa after 25 loading and unloading cycle.
 - At 2.5 mm stroke length, recorded soil stresses increased from near zero prior to loading, and reaching up to 2700 kPa after 7 loading and unloading cycle.
2. The “walking effect” of the Gina gasket displayed by the LVDT reading, where the gasket continuously move inward, show that an increasing amount of soil stresses is exerted onto the Gina gasket
 - Results of the control tests, which applies the same configuration of the cyclic movement while excluding the presence of sand, show that the Gina gasket does not move when subjected to constant stroke length.
 - Comparing results of the control test with the main experiment concludes that the “walking effect” of the Gina gasket indeed occurs due to the contraction and expansion of the joint gap, and not due to any other factors.

Q2 : Does the soil experience densification due to the cyclic loading-unloading process?

1. Penetrometer test results show that the joint gap sand increases in cone resistance after subsequent loading and unloading cycles.
 - Prior to loading, the penetrometer test results show zero resistance from the joint gap sand.
 - Following the experiments, penetrometer tests show an average cone resistance value between 0.15 to 0.3 MPa
2. Using the Schmertmann (1976) correlation, the resulting penetrometer cone resistances can be correlated with their respective relative densities.
 - Results show an increase of relative density from 0% prior to loading to around 15-30% after the final loading cycle.
3. The penetrometer tests discussed in point 1 and 2 are conducted on a relaxed state of the joint gap due to the limitations of the penetrometer. At the worst case scenario, where the joint gap is fully contracted, the cone resistance measurements and the subsequently calculated sand densities are expected to be much higher than currently obtained.
4. Increase in soil stresses after subsequent loading and unloading cycles signify that the joint gap sand increases in stiffness, which in turn indicates an increase in density.
 - The increase in soil stresses occurs due to overlying sand entering the joint gap, thus densifying the sand inside the joint gap.
5. The soil top deformation output obtained from the finite element analysis show that following a single cycle of loading and unloading, the top of the sand fails to rebound to its original height, therefore creating a void in the system. In reality, this void would be filled with the backfill sand outside of the system, thus densifying the joint gap sand.

6. Multiple phenomena, namely the failure of the natural ground arch forming above the joint gap, the rotation of principal axes, and the inability of the Gina gasket to rebound (walking effect) promote internal soil failure, hence facilitating the overlying sand to enter the joint gap
7. The “walking effect” show that the Gina gasket is unable to rebound to its original position after every succeeding cycle. Therefore after every unloading part of each cycle, the inward movement of the Gina gasket generates extra void space in the system for the backfilled sand to enter the joint gap, hence densifying the soil.
8. The rotation of the principal axes during the unloading part of every cycle develops slip surface lines inside the joint gap, which allows the sand to move more freely inside the joint gap. This phenomenon promotes densification of the joint gap sand.
 - The high soil vertical stresses due to friction imply that the rotation of the principal axes occurs earlier than expected, further promoting internal failure of sand.
9. The natural ground arch above the joint gap either failed to form prior to joint gap movement or structurally failed due to the joint gap movement. This phenomenon promotes the densification of sand inside the joint gap.
 - Test results show a clear densification of joint gap sand for every experiment. This condition would be impossible under normal circumstances due to the resistance of the natural ground arch outside of the joint gap. Hence, the ground arch must either failed to form, or circumstances of the experiment altered the existing ground arch and hinder its ability to carry weight.

Q3 : To what extent does the mechanics of loading and unloading cycles affect the soil stresses?

1. An increase in stroke length of the tunnel lining translates to a higher rate of joint gap sand densification.
 - The initial 5 loading cycles at every stroke length show similar values of normalized deflection values. However, at higher cycles, the experiments with higher stroke lengths have generally higher normalized deflection values than the experiments with lower stroke lengths. Hence, it can be concluded that the increase of sand densification rate is due to the higher stroke length.
2. At a number of cycles beyond 50, the sand continues to densify, and the Gina gasket continues to move inward. Hence, the Gina gaskets might be vulnerable to further damage if left in the current state of disrepair beyond the 50 years of service life.
3. The inability to rebound during unloading, combined together with higher Gina deflection, further facilitates the “walking effect” shown by the Gina gasket at higher stroke lengths. Hence, at higher stroke lengths, the gasket is more prone to failure.
 - The inability to rebound is also shown to a certain extent by the results of the finite element analysis.
4. The loading curve behaves in a gradual manner compared to the rapid change during unloading. This phenomenon implies hysteretic behavior occurs during each loading cycle.
5. The presence of hysteretic behavior indicates the soil underwent plastic deformation, further validating the hypothesis that the soil undergoes a change in volume and increasing in density.
6. Friction between the joint gap sand and the lining wall has a major effect on the increase of vertical stresses.
 - The initial assumption states that the vertical stresses stay constant at 68 kPa. Results of the finite element analysis show that the vertical stresses increase up to 760 kPa during loading. This occurs, in part, due to the high friction between the sand and the lining wall.
7. The stress path analysis had increased in accuracy due to new assumptions obtained from the finite element analysis. However, the improvements are still not enough to accurately determine the stress path in real life.
 - The initial stress path analysis assumes a constant value of vertical pressure at 68 kPa. Following the finite element analysis, the assumptions are adjusted to accommodate the new values of vertical stress.

Conclusions on Force Analysis

Further conclusions can also be drawn for the additional force analysis discussed in part 6.3:

1. Due to the good agreement between results of the experiment and the finite element analysis, a modified version of the original finite element model is sufficient to predict the behavior of the sand during the rehabilitation process of the joint gap.
2. Pushing back the entire bottom area of the Gina gasket to its original position requires forces up to 297000 kN/m.
3. Pushing back approximately 1/3 the area of the Gina gasket results in the unaffected gasket area being pushed to the side. Hence, the impact to the sand inside the immersion joint remains minimum.
4. In the condition that joint gap is at full expansion, the required force decreases by a factor of 16.
5. To reduce the required pushing-back force during joint rehabilitation, consider conducting reparations during the colder seasons, where the joint gap is at maximum width. Furthermore, taking out some of the sand inside the gap prior to installing the support strip would also significantly reduce the required force.

7.2.Limitations and Further Research

7.2.1.Possible Further Research Topics

The scale of the model and the materials used to replicate the joints impose a clear restriction in this research. Certain aspects, such as the magnitude of forces and actual failures of the gaskets are unable to be measured or observed. However, this pilot research may open up possibilities for further studies related to this topic. Possible further research topics include:

- Does the soil behave the same way in a full-scale model of the immersion joint?
- What is the magnitude of the force exerted by the soil inside the immersion joint gap onto the Gina profile?

Due to time constraints, the immersion joint gap model was not designed to be watertight. Hence, the experiments were conducted on dry sand, contrary to the saturated conditions of the prototype. Therefore, further research regarding these restrictions include:

- What is the behavior of saturated sand when introduced to similar conditions?
- What are the effects of pore water pressure on the behavior of the sand inside the joint gap?

The original solution to the project involves installing supporting steel strips in order to push the gasket back into position. Therefore, in a full-scale model, one might also figure out:

- What is the magnitude of the force required to push back the Gina gasket into its initial position?
- What is the magnitude of the force required to retain the Gina gasket for future tunnel designs?

Densification of the sand inside the joint gap is made possible due to the high friction between the sand and the tunnel lining, which prevents the joint gap sand to be pushed out of the system when the gap contracts. In theory, the friction resistance could be lowered by reducing the height of sand column inside the joint gap. This condition can be achieved by installing the Gina gasket at a higher position for future immersed tunnel design. Hence, some possible research questions regarding this topic include:

- Does lowering the sand column inside the joint gap have a significant effect on reducing the forces exerted by the densified sand on the Gina gasket?
- What is the critical height of the sand column?

7.2.2.Solutions

Regarding multiple possible research topics discussed in the preceding part, two options are available for the solution; manufacture a new device at true scale, or upgrade the current device to enable more detailed measurements. The new design should include the following improvements:

1. Extra LVDT sensors on the actuated lining to accurately determine the horizontal strain.
2. An overhauled design of the Gina gasket clamp system.
 - The underside of the gasket should be fixed and equipped with a load cell if one decides to measure the gasket force.

- The position of the gasket should be moveable if one decides to determine the critical height of the sand column
3. The model joint gap should be watertight. This involves custom seals in the gap between the actuated lining and the side wall, as well as utilizing a better, more watertight Gina seal.
 4. The actuator capacity should be increased. The actuator itself should also be automated to allow for more tests throughout the day.

Solution 1: Manufacture a 1:1 Scale Physical Model

The first solution involves designing and constructing a new physical model at true scale.

Pros

- Much more accurate and precise measurements by taking out the scaling factor
- Result of experiments can be more accurately extrapolated for other tunnels

Cons

- Device design, production, and manufacture takes upwards of 15 weeks excluding the experiment time
- More man-hour requirements, which translates to higher costs

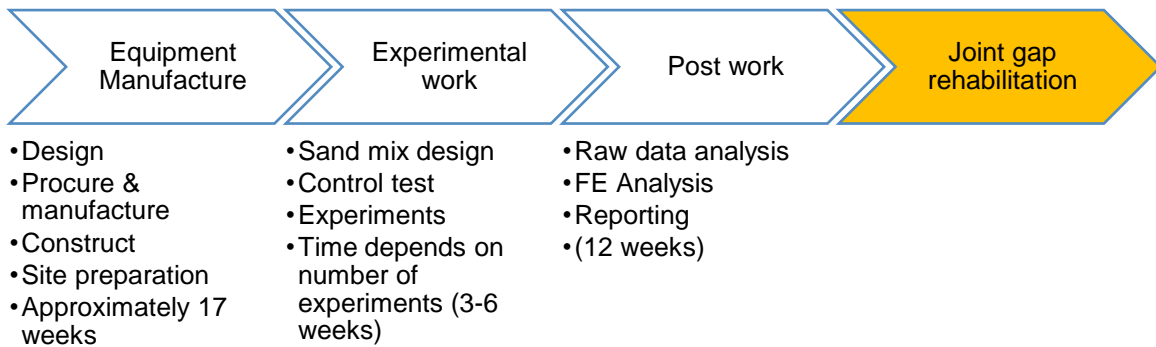


Figure 7-1 Work Flow for Solution 1

Solution 2: Modify the Current Physical Model

Pros

- Moderately accurate measurements
- Modifications take a short time to finish
- Fewer man-hour requirements, which translates to lower costs

Cons

- 1:3 scale is fixed and unchangeable
- Generally less accurate than a true scale model

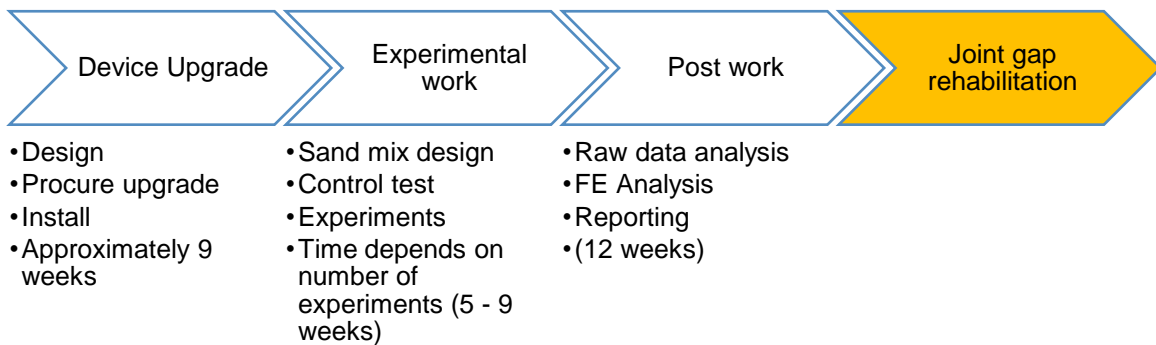


Figure 7-2 Work Flow for Solution 2

Estimations on the conceptual project plan are stated in Appendix I.

Bibliography

- Ameratunga, J., Sivakugan, N. and Das, B.M., 2016. Cone Penetrometer Test. In *Correlations of Soil and Rock Properties in Geotechnical Engineering* (pp. 115-157). Springer India.
- Anaraki, K.E. 2008. *Hypoplasticity Investigated: Parameter Determination and Numerical Simulation*, Master of Science, Delft University of Technology, The Netherlands.
- Arshad, M. and O'KELLY, B.C., 2014, July. Use of Miniature Soil Stress Measuring Cells under Repeating Loads. In *Information Technology in Geo-Engineering: Proceedings of the 2nd International Conference (ICITG) Durham, UK* (Vol. 3, p. 177). IOS Press.
- Askegaard, V., 1963. *Measurement of pressure in solids by means of pressure cells*. Danish Acad. of Technical Sciences.
- Askegaard, V., 1988. Problems in connection with design, calibration and use of pressure cells. *Journal of Theoretical and Applied Mechanics*, 26(2), pp.219-229.
- Beaty, M. and Byrne, P.M., 1998, August. An Effective Stress Model for Predicting Liquefaction Behaviour of Sand. In *Geotechnical Earthquake Engineering and Soil Dynamics III: (pp. 766-777)*. ASCE.
- Bo, M.W., Na, Y.M., Arulrajah, A. and Chang, M.F., 2009. Densification of granular soil by dynamic compaction. *Proceedings of the ICE-Ground Improvement*, 162(3), pp.121-132.
- Broere, W. and van Tol, A.F., 1998. Horizontal cone penetration testing. *Geotechnical Site Characterization, Proc. ISC*, 98, pp.989-994.
- Byrne, P.M., Park, S.S., Beaty, M., Sharp, M., Gonzalez, L. and Abdoun, T., 2004. Numerical modeling of liquefaction and comparison with centrifuge tests. *Canadian Geotechnical Journal*, 41(2), pp.193-211.
- Clayton, C.R.I. and Bica, A.V.D., 1993. The design of diaphragm-type boundary total stress cells. *Geotechnique*, 43(4), pp.523-535.
- Dave, T.N. and Dasaka, S.M., 2011. A review on pressure measurement using earth pressure cell. *Int. J. Earth Sci. Eng*, 4(6), pp.1031-1034.
- Dave, T.N. and Dasaka, S.M., 2013. In-house calibration of pressure transducers and effect of material thickness. *Geomech. Engrg-An Intl. J*, pp.1-15.
- Desrues, J., Lanier, J. and Stutz, P., 1985. Localization of the deformation in tests on sand sample. *Engineering fracture mechanics*, 21(4), pp.909-921.
- Evans, C.H., 1983. *An examination of arching in granular soils* (Doctoral dissertation, Massachusetts Institute of Technology).
- Han, C. and Drescher, A., 1993. Shear bands in biaxial tests on dry coarse sand. *Soils and Foundations*, 33(1), pp.118-132.
- Handy, R.L., 1985. The arch in soil arching. *Journal of Geotechnical Engineering*, 111(3), pp.302-318.
- Iglesia, G.R., Einstein, H.H. and Whitman, R.V., 2013. Investigation of soil arching with centrifuge tests. *Journal of Geotechnical and Geoenvironmental engineering*, 140(2), p.04013005.
- Jamiolkowski, M., 2001, October. Lo Presti, DCF, Manassero, M. 2001. In *Evaluation of relative density and shear strength of sand from CPT and DMT. LADD Symposium*.
- Janbu, N., 1963, October. Soil compressibility as determined by oedometer and triaxial tests. In *Proceedings of the European conference on soil mechanics and foundation engineering* (Vol. 1, pp. 19-25).
- Jardine, R.J. and Standing, J.R., 2012. Field axial cyclic loading experiments on piles driven in sand. *Soils and foundations*, 52(4), pp.723-736.
- Kallstenius, T. and Bergau, W., 1956. *Investigations of soil pressure measuring by means of cells*.
- Kishida, H., and M. Uesugi. "Tests of the interface between sand and steel in the simple shear apparatus." *Geotechnique* 37.1 (1987): 45-52.

- Kulhawy, F.H. and Mayne, P.W., 1990. *Manual on estimating soil properties for foundation design* (No. EPRI-EL-6800). Electric Power Research Inst., Palo Alto, CA (USA); Cornell Univ., Ithaca, NY (USA). Geotechnical Engineering Group.
- Labuz, J.F. and Theroux, B., 2005. Laboratory calibration of earth pressure cells.
- Lunniss, R. and Baber, J., 2013. *Immersed tunnels*. CRC Press.
- McKelvey, J.A., 1994. The anatomy of soil arching. *Geotextiles and Geomembranes*, 13(5), pp.317-329.
- Nielson, F.D., 1966. Soil-structure-arching Analysis of Buried Flexible Structures. Ph.D. Thesis in Civil Engineering. University of Arizona.
- O'Reilly, M.P. and Brown, S.F. eds., 1991. *Cyclic loading of soils: from theory to design* (pp. 1-18). Glasgow, UK: Blackie.
- Robertson, P.K. and Campanella, R.G., 1986. *Guidelines for Use, Interpretation and Application of the CPT and CPTU*. Hogentogler & Company.
- Sadrekarami, A., 2016. Estimating relative density of sand with cone penetration test. *Proceedings of the Institution of Civil Engineers-Ground Improvement*, 169(4), pp.253-263.
- Salgado, R., Mitchell, J.K. and Jamiolkowski, M., 1997. Cavity expansion and penetration resistance in sand. *Journal of Geotechnical and Geoenvironmental Engineering*, 123(4), pp.344-354.
- Schmertmann, J.H., 1976. An updated correlation between relative density, D_r , and Fugro-type electric cone bearing, q_c . *Contract Report DACW*, pp.39-76.
- Talesnick, M., 2005. Measuring soil contact pressure on a solid boundary and quantifying soil arching
- Talesnick, M.L., Ringel, M. and Avraham, R., 2014. Measurement of contact soil pressure in physical modelling of soil-structure interaction. *International Journal of Physical Modelling in Geotechnics*, 14(1), pp.3-12.
- Terzaghi, K., 1943. *Theoretical Soil Mechanics*. John Wiley & Sons, Inc..
- Tsuha, C.D.H.C., Foray, P.Y., Jardine, R.J., Yang, Z.X., Silva, M. and Rimoy, S., 2012. Behaviour of displacement piles in sand under cyclic axial loading. *Soils and foundations*, 52(3), pp.393-410.
- Venkatarama-Reddy, B.V. and Jagadish, K.S., 1993. The static compaction of soils. *Geotechnique*, 43(2).
- Von Soos, P., 1990. Properties of soil and rock. *Grundbautaschenbuch Part, 4*.
- Walters, J.K., 1973. A theoretical analysis of stresses in silos with vertical walls. *Chemical Engineering Science*, 28(1), pp.13-21.
- Weiler, W.A. and Kulhawy, F.H., 1982. Factors affecting stress cell measurements in soil. *Journal of the Geotechnical Engineering Division*, 108(12), pp.1529-1548.
- Whitman, R.V., Getzler, Z. and Hoeg, K., 1962. *Static tests upon thin domes buried in sand*. MASSACHUSETTS INST OF TECH CAMBRIDGE.
- Wijewickreme, D., Sriskandakumar, S. and Byrne, P., 2005. Cyclic loading response of loose air-pluviated Fraser River sand for validation of numerical models simulating centrifuge tests. *Canadian Geotechnical Journal*, 42(2), pp.550-561.
- WILLIAMS, F.H.P., 1949. COMPACTION OF SOILS. *Journal of the Institution of Civil Engineers*, 33(2), pp.73-99.
- Wrześniński, G. and Lechowicz, Z., 2013. Influence of the rotation of principal stress directions on undrained shear strength. *Annals of Warsaw University of Life Sciences-SGGW. Land Reclamation*, 45(2), pp.183-192.